Dissertation
submitted to the
Combined Faculties for the Natural Sciences and for Mathematics
of the Ruperto-Carola University of Heidelberg, Germany
for the degree of
Doctor of Natural Sciences

Put forward by
M. Sc. Julia-Maria Osinga-Blättermann
Born in: Varel, Germany

Oral examination: December 20th, 2016

Determination of absorbed dose to water in a clinical carbon ion beam by means of fluorescent nuclear track detectors, ionization chambers, and water calorimetry

Referees: **Prof. Dr. Wolfgang Schlegel**
Prof. Dr. Oliver Jäkel

Erklärung

Ich erkläre hiermit, dass ich die vorgelegte Dissertation selbst verfasst und mich dabei keiner anderen, als der von mir ausdrücklich bezeichneten Quellen und Hilfen bedient habe.

Heidelberg, d. 02.11.2016

Julia-Maria Osinga-Blättermann

Bestimmung der Wasser-Energiedosis im klinischen Kohlenstoffstrahl mit Hilfe fluoreszierender Kernspurdetektoren, Ionisationskammern und Wasserkalorimetrie

Bis heute hat die Dosimetrie von Kohlenstoffionen mittels Ionisationskammern nicht die gleiche Präzision erreicht wie von hoch-energetischen Photonen. Dies beruht maßgeblich auf der dreifach größeren Messunsicherheit des k_{Q,Q_0}-Faktors der Ionisationskammern, welcher aufrund fehlender experimenteller Daten auf Berechnungen basiert.
Die vorliegende Arbeit umfasst zwei Hauptziele hinsichtlich der Dosimetrie von Kohlenstoffstrahlung: Erstens, die Untersuchung des Potentials fluoreszierender Kernspurdetektoren für fluenz-basierte Dosimetrie und zweitens, die experimentelle Bestimmung des k_{Q,Q_0}-Faktors.
Der direkte Vergleich von fluenz- und ionisations-basierter Dosimetrie hat einen signifikanten Unterschied von 4.5 % gezeigt, welcher erneut die Frage nach der Genaugkeit berechneter k_{Q,Q_0}-Faktoren aufgeworfen hat.
Daher wurden Messungen der Wasser-Energiedosis mit Hilfe der Wasserkalorimetrie durchgeführt, welche die direkte Kalibrierung von Ionisationskammern und damit die experimentelle Bestimmung von k_{Q,Q_0} ermöglichen. Zum ersten Mal konnte gezeigt werden, dass die experimentelle Bestimmung des k_{Q,Q_0}-Faktors für Kohlenstoffstrahlung mit einer Standardmessunsicherheit von 0,8 % erreichbar ist. Dies bedeutet eine Verringerung der Unsicherheit im Vergleich zu berechneten Werten um den Faktor drei und ermöglicht daher eine signifikante Reduktion der Gesamtunsicherheit bei der ionisations-basierten Dosimetrie klinischer Kohlenstoffstrahlung.

Determination of absorbed dose to water in a clinical carbon ion beam by means of fluorescent nuclear track detectors, ionization chambers, and water calorimetry

Until now, dosimetry of carbon ions with ionization chambers has not reached the same level of accuracy as of high-energy photons. This is mainly caused by the threefold higher uncertainty of the k_{Q,Q_0}-factor of ionization chambers, which is derived by calculations due to a lack of experimental data.
The current thesis comprises two major aims with respect to the dosimetry of carbon ion beams: first, the investigation of the potential of fluorescent nuclear track detectors for fluence-based dosimetry and second, the experimental determination of the k_{Q,Q_0}-factor.
The direct comparison of fluence- and ionization-based measurements has shown a significant discrepancy of 4.5 %, which re-opened the discussion on the accuracy of calculated k_{Q,Q_0}-factors.
Therefore, absorbed dose to water measurements by means of water calorimetry have been performed allowing for the direct calibration of ionization chambers and thus for the experimental determination of k_{Q,Q_0}. For the first time it could be shown that the experimental determination of k_{Q,Q_0} for carbon ion beams is achievable with a standard measurement uncertainty of 0.8 %. This corresponds to a threefold reduction of the uncertainty compared to calculated values and therefore enables to significantly decrease the overall uncertainty related to ionization-based dosimetry of clinical carbon ion beams.

List of Publications

Parts of this work have been published in the following reference:

J.-M. Osinga, S. Brons, J.A. Bartz, M.S. Akselrod, O. Jäkel, S. Greilich.
Absorbed dose in ion beams: Comparison of ionization- and fluence-based measurements.
Radiation Protection Dosimetry **161**, pp. 387-392 (2014).

Further publications with own contributions:

J.-M. Osinga-Blättermann, S. Greilich. *Strahlenphysik*. In: Medizinische Physik (Springer), Editors: Prof. Schlegel, Prof. Karger, Prof. Jäkel, (submitted).

J.-M. Osinga, I. Ambrožová, K. Pachnerová Brabcová, M.S. Akselrod, O. Jäkel, M. Davídková, S. Greilich. *Single track coincidence measurements of fluorescent and plastic nuclear track detectors in therapeutic carbon beams*. Journal of Instrumentation **9**, PO4013 (2014).

J.-M. Osinga, M.S. Akselrod, R. Herrmann, V. Hable, G. Dollinger, O. Jäkel, S. Greilich. *High-accuracy fluence determination in ion beams using fluorescent nuclear track detectors*. Radiation Measurements **56**, pp. 294-298 (2013).

S. Greilich, J.-M. Osinga, M. Niklas, F.M. Lauer, G. Klimpki, F. Bestvater, J.A. Bartz, M.S. Akselrod, O. Jäkel. *Fluorescent nuclear track detectors as a tool for ion-beam therapy research*. Radiation Measurements **56**, pp. 267-272 (2013).

G. Klimpki, J.-M. Osinga, R. Herrmann, M.S. Akselrod, O. Jäkel, S. Greilich. *Ion range measurements using fluorescent nuclear track detectors*. Radiation Measurements **56**, pp. 342-346 (2013).

J.-M. Osinga, M. Niklas, G. Klimpki, M.S. Akselrod, O. Jäkel, S. Greilich. *Proton and ion beam radiation therapy: A microscopic dosimetry system for radiobiology and treatment*. International Journal of Radiation Oncology∗Biology∗Physics **84**(3), S54 (2012).

Contents

List of Abbreviations

BAMS	Beam application monitoring system
ddd	Depth dose distribution
CSDA	Continuous slowing down approximation
DKFZ	German Cancer Research Center
FNTD	Fluorescent nuclear track detector
FWHM	Full width at half maximum
GSI	Gesellschaft für Schwerionenforschung
HIMAC	Heavy Ion Medical Accelerator
HIT	Heidelberg Ion-Beam Therapy Center
ICRU	International Commission on Radiation Units and Measurements
LET	Linear energy transfer
MBR	Machine beam record
MC	Monte Carlo
MWPC	Multi-wire proportional chamber
PMMA	Poly(methyl methacrylate), also known as acrylic glass
PTB	Physikalisch-Technische Bundesanstalt
RBE	Relative biological effectiveness
SOBP	Spread-out Bragg peak
WEPL	Water-equivalent path length
WET	Water-equivalent thickness

Chapter 1

Introduction

Although radiation therapy with carbon ions already started more than 20 years ago in 1994 at the Heavy Ion Medical Accelerator (HIMAC) in Chiba, Japan with,today, more than 15000 patients treated in one of the 10 facilities being in clinical operation ([PTCOG, 2016], [Jermann, 2015]), the dosimetry of carbon ion beams has - up to now - by far not reached the same level of accuracy as of conventional high-energy photon beams. This conflicts with the main benefits of carbon ion radiotherapy being (I) the possibility of a high local dose deposition in a well-defined depth (Bragg peak) as well as (II) the strong increase of the ion's linear energy transfer (LET) and thus of the ionization density yielding a better response per deposited physical dose as expressed by the relative biological effectiveness (RBE) [Debus, 2009]. Consequently, radiation therapy with carbon ions can show substantial biological and physical advantages over conventional radiation therapy with photons or electrons [Durante and Loeffler, 2010]. In turn, this simultaneously asks for a very accurate dosimetry in order to verify and assure the quality of the irradiation. While the standard measurement uncertainty assigned to the dosimetry of high-energy photons by means of calibrated ionization chambers is stated with 1 % in the International Code of Practice for the Dosimetry of External Radiotherapy Beams TRS-398, the corresponding uncertainty related to the dosimetry of carbon ions is about a factor of three higher [IAEA, 2000]. Although no precise recommendations are given, an appropriate limit for the combined standard uncertainty of the dose delivered to the patient is assumed to be around 5 % in TRS-398, which, besides uncertainties from the dose measurement itself, also includes uncertainty contributions from dose calculation as well as dose delivery. Out of this, Karger et al. [2010] conclude that absorbed dose measurements in clinical applications should be performed with an uncertainty well below this overall requirement, *i.e.* in the order of 1 %, which - up to now - does not hold true for the dosimetry of clinical carbon ion beams.

The large uncertainty associated to the reference dosimetry of carbon ion beams by means of ionization chambers is mainly caused by the weak knowledge of the so-called k_{Q,Q_0}-factor. This factor corrects for the different response of the ionization chamber between the actual user beam quality Q (here: ^{12}C) and the reference beam quality Q_0 (here: ^{60}Co) used for the calibration of the chamber in terms of absorbed dose to water. Due to the lack of experimental data for the k_{Q,Q_0}-factor, this factor is up to now determined by calculations based on cavity theory or Monte-Carlo transport simulations. Hence, although methods for ion beam dosimetry have been established with calibrated ionization chambers being the gold standard, there is still a need for improvement of the dosimetric accuracy and for the devel-

opment of more efficient measurement techniques [Karger et al., 2010].

At this point one might argue that reducing the uncertainty of the physical quantity absorbed dose with respect to carbon ion beams is a 'drop in the bucket' considering the substantial uncertainties of up to 20 % associated with the clinically relevant iso-effective dose[1] [Karger and Jäkel, 2007]. In spite of the importance of the iso-effective dose and the involved uncertainty, accurate knowledge of the quantity absorbed dose is still required for several reasons as discussed by Karger et al. [2010]: First of all, beam delivery in ion beam therapy is controlled in terms of absorbed dose (or particle numbers) and thus relies on accurate dosimetry. Second, quality assurance measurements such as the verification of dose delivery is performed in terms of absorbed rather than iso-effective dose. Concluding Karger et al. [2010] point out that beam characteristics are described by physical quantities under the general assumption that a reproduction of the physical parameters of the irradiation will also reproduce the response of biological systems. As a consequence, absorbed dose is indispensable as an operative quantity in ion beam radiotherapy and its precise knowledge essential for safe application as well as for reproducible clinical results.

The current thesis therefore comprises two major aims: first, the investigation of the potential of Al_2O_3:C,Mg-based fluorescent nuclear track detectors (FNTDs) for fluence-based dosimetry in carbon ion beams by a direct comparison of this relatively new technique with ionization-based measurements of absorbed dose to water. And second, the experimental determination of the k_{Q,Q_0}-factor for carbon ion beams with a standard measurement uncertainty below 1 % by means of water calorimetry in order to verify ionization chamber dosimetry and significantly decrease its uncertainty.

The motivation for the first aim results from previous studies showing that FNTDs [Akselrod and Sykora, 2011] are promising candidates to extend fluence-based dosimetry and ion beam characterization to clinical doses and therapeutic depth, since those detectors have shown to cover the entire range of ion types and energies found in therapeutic ion beams [Osinga et al., 2013]. Furthermore, recent developments indicate that knowledge of the primary particle fluence plus limited information on those of the most important fragment(s) can be sufficient to characterize an ion beam [Lühr et al., 2012]. This confirms the promising approach of fluence-based dosimetry with energy discriminating detectors like FNTDs. Potential applications of the FNTD technique are especially seen where employment of ionization chambers is challenging, such as in laser-accelerated particles, dosimetry in magnetic fields, or in-vivo dosimetry. The experimental set-up used for the direct comparison study of fluence- and ionization-based dosimetry as well as the measurements performed in the clinical carbon ion beam at the Heidelberg Ion-Beam Therapy Center (HIT) and corresponding results are presented and discussed in chapter 5.

Without anticipating too much of the work presented in chapter 5, the results re-opened the discussion on the accuracy of the clinically-used calculated k_{Q,Q_0}-factor for carbon ion beams [Hartmann et al. [1997] and references therein] leading over to the second objective of this study. In order to investigate the contested accuracy of k_{Q,Q_0} in more detail, the fo-

[1] The iso-effective dose is defined as the dose of a photon treatment resulting in the same biological effect using the same fractionation schedule and is given by the product of the (physical) absorbed dose and the RBE [Karger et al., 2010].

cus of the second and main part of this thesis is on absolute dose to water measurements in the scanned carbon ion beam at HIT using the transportable PTB (Physikalisch-Technische Bundesanstalt) water calorimeter [Krauss, 2006b]. The goal of these measurements is to directly calibrate ionization chambers in units of absorbed dose to water and thus the experimental verification of the currently used k_{Q,Q_0}-factor for ionization chambers for the first time. Major challenges of this study are the determination of optimized irradiation conditions for the application of the water calorimeter at HIT as the measurements are performed under special irradiation conditions, namely (I) the active beam delivery technique using intensity-controlled raster scanning and (II) the irradiation with a pulsed beam as discussed in Sec. 6.2. Further, besides precise calorimetric and ionometric measurements presented in Sec. 6.4 and Sec. 6.5, detailed investigations and monitoring of the irradiation field used for the determination of k_{Q,Q_0} (Sec. 6.3) are of major importance in order to allow for an accurate determination of subsequent calorimetric and ionometric correction factors with low standard measurement uncertainty. Finally, the experimentally determined k_{Q,Q_0}-factor for carbon ion beams including a detailed investigation of uncertainties will be given in Sec. 6.6 and discussed in Sec. 6.7.

To finish, chapter 7 summarizes the results of both parts of this thesis, draws final conclusions, and presents an outlook on possible future projects. In addition, the impact of the experimentally determined k_{Q,Q_0}-factor by means of water calorimetry as well as the knowledge gained from the corresponding detailed irradiation field characterization measurements on the results obtained by the direct comparison of fluence- and ionization-based dosimetry will be discussed.

The physical background and the definition of fundamental quantities with relevance to the measurements conducted are briefly introduced in chapter 2. Chapter 3 summarizes the current status of reference dosimetry with ionization chambers for ion beams according to the International Code of Practice TRS-398 [IAEA, 2000] and the soon to be published German dosimetry protocol DIN 6801-1 [DIN, 2016] with the main focus on the k_{Q,Q_0}-factor. Similarities and differences of both protocols are highlighted and the individual components of the calculated k_{Q,Q_0}-factor analyzed in detail including corresponding uncertainties. The materials and methods applied within this study are introduced in chapter 4 with emphasize on the main detectors used being the water calorimeter, the ionization chamber, and the FNTD.

Chapter 2

Background

This chapter briefly describes the interaction processes of clinical carbon ions when traversing through matter focusing on those being of relevance for the understanding of the measurements performed within this thesis. Further, frequently used terms are defined and corresponding equations given.

2.1 Stopping-power

The slowing-down process of carbon ions with clinically relevant energies (about 90 MeV/u up to 430 MeV/u) is overwhelmingly dominated by inelastic collisions with the target electrons [Schardt et al., 2010]. The mean energy-loss of charged particles per unit path length, dE/dx, due to electronic interactions is referred to as electronic (or collision) stopping-power, S_{el}, and can be well described by the Bethe-Bloch formula ([Bethe, 1930], [Bloch, 1933]). The relativistic version of the original Bethe-Bloch equation has been further modified by Fano [1963] including the shell correction term C/Z and the density effect correction term $\delta/2$, while higher order corrections are neglected in the following commonly-used equation:

$$S = -\frac{dE}{dx} \approx S_{el}(E) = \frac{e^4}{4\pi m_e c^2 \varepsilon_0^2} \cdot \frac{z^2}{\beta^2} \cdot \rho_e \left[ln\left(\frac{2m_e c^2 \beta^2}{I(1-\beta^2)}\right) - \beta^2 - \frac{\delta}{2} - \frac{C}{Z}\right] . \qquad (2.1)$$

Here, E is the kinetic energy of the projectile, e and m_e the charge and mass of an electron, c the speed of light, ε_0 the vacuum permittivity, z and Z the charge of the projectile and target medium respectively, β the velocity of the projectile divided by c, ρ_e the electron density per volume of the target medium, and I the mean excitation energy of the target medium. The shell correction term corrects the assumption that the ion velocity is much larger than the target electron velocity and thus becomes important at projectile velocities comparable or smaller than the orbital electron velocities [Ziegler, 1999]. Further, at low velocities (< 10 MeV/u), the mean charge state of the projectile decreases, which needs to be considered by replacing the atomic charge number z in Eq. 2.1 by the empirically derived effective charge z_{eff} [Barkas and Evans, 1963]. Contrary, the density effect term gains importance at large projectile energies correcting for polarization effects in the target which reduce the stopping-power. However, this effect is of minor importance for clinically used energies [Ziegler, 1999].

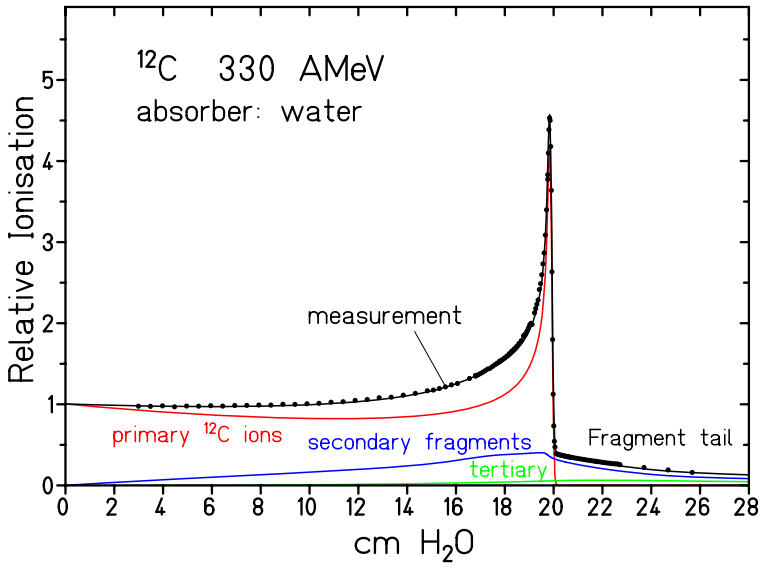

Fig. 2.1: *Depth dose distribution of 330 MeV/u carbon ions in water comparing measured data (black dots) to a model calculation (solid curves). The figure emphasizes the buildup of fragments due to nuclear fragmentation (cf Sec. 2.7) and their increasing dose contribution to the total deposited dose with depth. While the total deposited dose (black curve and dots) in the Bragg peak region is still dominated by the dose deposited by primary carbon ions (red curve), secondary (blue curve) and tertiary (green curve) fragments exhibit a longer range and thus cause the characteristic dose tail behind the Bragg peak. Reprinted from Schardt [2007].*

With respect to the projectile, S_{el} depends on the particle's velocity and charge. Due to the $\frac{1}{\beta^2}$ term, the energy-loss increases with decreasing velocity and thus energy resulting in the characteristic depth dose distribution of carbon ion beams. As exemplary shown in Fig. 2.1, the curve is defined by a flat plateau (entrance) region and a distinct dose peak (Bragg peak) near the end of the particle's trajectory. On the target side, the electronic energy-loss depends on the electron density and the logarithm of the I-value. Within this thesis, Bragg's additivity rule

$$ln(I) = \frac{\sum_j w_j \cdot \frac{Z_j}{A_j} \cdot ln(I_j)}{\sum_j w_j \cdot \frac{Z_j}{A_j}} \tag{2.2}$$

has been used to calculate the I-value for unlisted compounds by multiplying the individual ratio of atomic number Z_j and mass number A_j of each element j with the mass weight fraction w_j [Bragg and Kleeman, 1905]. The I-values for the individual constituents were thereby taken from ICRU [1993], Tab. 2.11.

The electronic stopping-power is equal to the unrestricted **linear energy transfer (LET)**, which is a surrogate for the ionization density of charged particles when traversing matter. The restricted LET L_Δ, on the other hand, only considers released electrons with an kinetic energy below a certain threshold value Δ.

2.2 Particle range

By means of the stopping-power S, the total path length, R_{CSDA}, of a particle traversing a medium can be calculated using the continuous slowing down approximation (CSDA) by integrating over the initial particle energy, $E_{initial}$, to zero:

$$R_{CSDA} = -\int_{E_{initial}}^{0} \frac{1}{S(E)} dE = -\int_{E_{initial}}^{0} \left(\frac{dE}{dx}\right)^{-1} dE \ . \tag{2.3}$$

If straggling effects can be assumed to be small as it is the case for clinical carbon ion beams, R_{CSDA} is a good approximation of the mean particle range R [Sigmund, 2004].
In clinical dosimetry, the practical range, R_p, as well as the residual range, R_{res}, are commonly used to define the particle range being directly derived from the measured depth dose distribution. In the case of carbon ion beams, R_p is defined as the depth where the relative dose deposition behind the Bragg peak (100 %) amounts to 50 %. The residual range is then given by the difference of R_p and the measurement depth z according to $R_{res} = R_p - z$ for $z < R_p$ [DIN, 2016], which is for example needed in order to determine the radiation quality, Q, of ion beams (*cf* Sec. 3.1).

2.3 Energy-loss and range straggling

While the energy-loss of a single charged particle traversing through matter results in a very sharp Bragg peak, statistical fluctuations in the number of collisions and the energy transferred in each collision cause a broadening of the Bragg peak for an ion beam consisting of many particles. This effect is referred to as energy-loss straggling with the probability distribution for the energy-loss depending on the number of interactions and with that on the absorber thickness [Leo, 1994]. These fluctuations can be described by means of the Vavilov theory [Vavilov, 1957], which combines the different theories on the theoretical calculation of the energy-loss probability distribution dedicated to different regions of applicability. A detailed description of the underlying theories can be found in the stated references, while only a brief overview will be given here. In the limit of many collisions, N, and thus thick absorbers, the Vavilov distribution becomes Gaussian with the corresponding probability distribution for the energy-loss given by

$$f(\Delta E) = \frac{1}{\sqrt{2\pi\sigma_E}} exp \frac{(\Delta E - \overline{\Delta E})^2}{2\sigma_E^2} \tag{2.4}$$

with

$$\sigma_E = 4\pi z_{eff} Z e^4 N \Delta x \left[\frac{1 - \frac{\beta^2}{2}}{1 - \beta^2}\right] \ . \tag{2.5}$$

In contrast to thick absorbers, the possibility of a large energy transfer in a single collision can no longer be neglected with respect to thin absorbers, where only a small number of collisions take place. Although these events are still rare, they lead to an asymmetric energy-loss probability distribution - known as Landau distribution [Landau, 1944] - exhibiting a long tail towards high energies. As a result, the most probable energy-loss resulting from this distribution is smaller than the mean energy-loss [Leo, 1994].

A direct consequence of energy-loss straggling is range straggling with the variance of range straggling, σ_R, being directly related to the variance of energy-loss straggling, σ_E:

$$\sigma_R^2 = \int_0^{E_i} \left(\frac{d\sigma_E}{dx}\right) \left(\frac{dE}{dx}\right)^{-3} dE \; . \tag{2.6}$$

The ratio of σ_R and the mean particle range, R, can be described by

$$\frac{\sigma_R}{R} = \frac{1}{\sqrt{m}} f\left(\frac{E}{mc^2}\right) \; , \tag{2.7}$$

with f being an absorber-dependent function and m the mass of the particle. Due to the strong dependence on $1/\sqrt{m}$, relative range straggling is for example decreased by a factor of 3.5 for carbon ions in comparison to protons. Besides energy-loss straggling and multiple Coulomb scattering, inhomogeneities in the density of the traversed media also contribute to range straggling [Schardt et al., 2010]. This effect is for example clearly shown in the calorimetric measurements performed within this thesis, where highly-inhomogeneous styrofoam used for thermal isolation leads to an additional broadening of the resulting carbon ion Bragg peak as shown in Fig. 6.14.

2.4 Water equivalent path length

The water equivalent path length (WEPL) is an important quantity in proton and ion beam radiotherapy as it allows to convert particle ranges in human tissue to corresponding ranges in water needed for analytical dose planning algorithms [Krämer et al., 2000]. WEPL is thereby defined as the ratio of the mean particle range in a medium m relative to the range in water w and can thus be approximated by means of the corresponding stopping-power ratio neglecting shell and density corrections [Hünemohr, 2014]:

$$WEPL \approx \frac{\rho_{e,m}}{\rho_{e,w}} \cdot \frac{ln(2m_e c^2\beta^2) - ln(1-\beta^2) - \beta^2 - ln(I_m)}{ln(2m_e c^2\beta^2) - ln(1-\beta^2) - \beta^2 - ln(I_w)} \; . \tag{2.8}$$

Experimentally, the WEPL-value of a material can be determined by means of a water range telescope (*cf* PEAKFINDER, Sec. 4.4.3) as described in Jäkel et al. [2001]. First, the relative depth dose distribution in water is measured without any absorber yielding a reference for the relative position of the Bragg peak, r_w. In a second step, a slap of the material to be investigated of thickness d_m is placed upstream of the water absorber and the Bragg curve is measured again using the very same particle type and energy. By determining the corresponding position r_m of the shifted Bragg peak, the WEPL-value of the added material can be determined with an accuracy of 1 % [Jäkel et al., 2001] according to the following equation:

$$WEPL_m = \frac{r_w - r_m}{d_m} \; . \tag{2.9}$$

Another term often used in this context is the **water equivalent thickness (WET)** of a material, which is defined as $WET_m = WEPL_m \cdot d_m$.

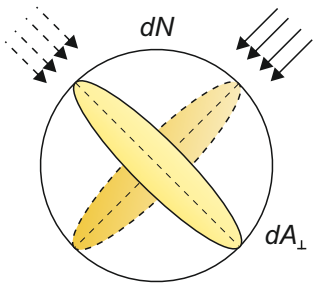

Fig. 2.2: *Illustration of the spatial differential quantity* Φ*. According to its definition given in Eq. 2.11, the considered area* $dA_\perp$ *is perpendicular to the direction of each incident particle* N*. Image reprinted from Osinga [2012].*

2.5 Absorbed dose and fluence-based dose determination

A quantity of major importance in radiation therapy is absorbed dose, D, which is defined as

$$D = \frac{d\bar{\varepsilon}}{dm} , \tag{2.10}$$

where $d\bar{\varepsilon}$ is the mean energy imparted by ionizing radiation to matter of mass dm [ICRU, 1998]. The corresponding unit is J per kg, which is often referred to as Gray (Gy). Many different methods for the determination of absorbed dose to water, D_w, exist, with three of them primarily used within this thesis: (I) Absolute dosimetry by means of water calorimetry (*cf* Sec. 4.1), (II) reference dosimetry with calibrated ionization chambers (*cf* Sec. 3 and Sec. 4.2) as well as (III) fluence-based dosimetry, with the main concept briefly described in the following section.

Fluence-based dose determination

By means of the particle fluence, Φ, which is defined as

$$\Phi = \frac{dN}{dA_\perp} , \tag{2.11}$$

with dN being the number of particles incident on a sphere of cross-sectional area $dA_\perp$ as illustrated in Fig. 2.2 [ICRU, 1998], the absorbed dose to a medium m, $D_{m,Q}$, deposited by a beam of quality Q can be derived under the assumption of secondary electron equilibrium from

$$D_{m,Q} = \phi \cdot \frac{S_{m,Q}}{\rho_m} . \tag{2.12}$$

Here, $S_{m,Q}/\rho_m$ is the mass stopping-power of the medium and ρ_m its density. With respect to mixed particle fields (*e.g.* clinical carbon ion beams), dose contributions from the complete energy spectrum of primary and secondary particles (*cf* Sec. 2.7) need to be considered according to

$$D_{m,Q} = \frac{1}{\rho_m} \cdot \sum_T \int_E \Phi_{E,T}(E) \cdot S_{m,Q}(E,T) dE , \tag{2.13}$$

with T indicating different particle species and E being the kinetic energy.

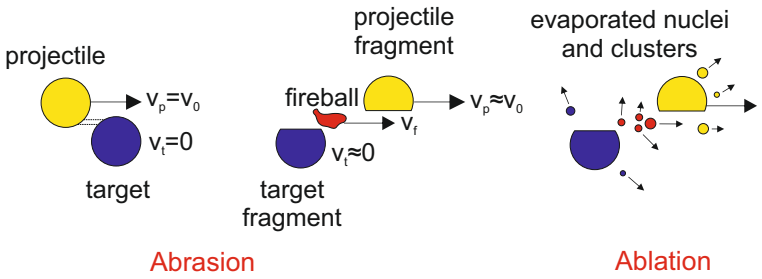

Fig. 2.3: *Illustration of the abrasion-ablation model of peripheral collisions at high energies assuming a projectile velocity v_p and a stationary target nucleus. Reproduction according to Gunzert-Marx et al. [2008].*

2.6 Lateral beam spread

In general, clinical carbon ion beams experience only a small lateral deflection when traversing through matter, which is mainly caused by elastic Coulomb interactions with the target nucleus while scattering due to electronic interactions can be neglected [Schardt et al., 2010]. For small scattering angles θ, the resulting angular distribution can be approximated by a Gaussian function with the corresponding standard deviation, σ_θ, in units of rad given by

$$\sigma_\theta = \frac{14.1\,MeV}{\beta pc} z \sqrt{\frac{d}{L_{rad}}} \left[1 + \frac{1}{9} log_{10} \left(\frac{d}{L_{rad}} \right) \right] , \tag{2.14}$$

with d being the penetration depth, p the momentum of the projectile, and L_{rad} a tabulated material-specific radiation length [Highland, 1975]. Without going into detail, two important consequences result from this formula [Schardt et al., 2010]: (I) High-Z targets cause a larger angular spread than low-Z targets of the same thickness and (II) the angular spread for heavy charged particles is small (about 1 mrad for a thin target) but increases significantly towards low energies. However, it is important to keep in mind that even small lateral beam spreads can result in non-negligible range straggling in the case of inhomogeneous materials.

2.7 Fragmentation

Especially at large penetration depth, nuclear fragmentation processes have a significant impact on radiotherapy with high energy carbon ion beams as they directly influence the particle spectrum and with that the dose deposition. The fragmentation process can be described as a two-step process by means of the abration-ablation model [Serber, 1947]. This is schematically shown in Fig. 2.3 using the example of a peripheral collision being the most frequent nuclear reactions due to geometrical reasons. In the first step, the so-called 'abrasion', nucleons in the overlapping zone of the interacting projectile and target nucleus are abraded forming the hot reaction zone referred to as 'fireball'. Meanwhile, the outer nucleons are only slightly affected by the collision. Afterwards, the remaining target and projectile fragments as well as the fireball de-excite in the second step ('ablation') by evaporation of nucleons and light clusters [Schardt et al., 2010]. As a consequence, nuclear fragmentation causes a loss of primary particles (*e.g.* only 52 % of the primary carbon ions with a range of 16 cm in water reach the Bragg peak [Schardt et al., 2010]) and a buildup of lower-Z fragments, which increases with depth. As the projectile fragments continue their traversal through matter with almost the same velocity and direction as the projectile nucleus, they exhibit longer ranges than the primary ions as the particle range scales with $1/Z^2$. Thus, projectile fragments with lower Z than the primary particle deposit their dose behind the Bragg peak producing the

characteristic dose tail as exemplary shown in Fig. 2.1. Target fragments, on the other hand, are emitted isotropically with much lower velocity, while particles ablated from the fireball cover the range between projectile and target emission [Gunzert-Marx et al., 2008].

Chapter 3

Current Status of Reference Dosimetry with Ionization Chambers for Ion Beams

Following the formalism for the dosimetry of high energy photon and electron beams, the International Code of Practice TRS-398 [IAEA, 2000] as well as the German dosimetry protocol DIN 6801-1 [DIN, 2016], which is supposed to be published in 2016, recommend the determination of absorbed dose to water in ion beams using an air-filled ionization chamber calibrated in terms of absorbed dose to water in a ^{60}Co gamma ray reference beam. In this context, the term ion beam refers to all ions with atomic numbers between two being helium and 18 being argon having ranges of $2-30\,$cm in water with respect to TRS-398 and to all ions with atomic numbers between two being helium and 10 being neon having practical ranges of $1-30\,$cm in water according to DIN-6801-1. In Germany, the primary standard for absorbed dose to water with respect to ^{60}Co radiation is the water calorimeter (*cf* Sec. 4.1), which is operated by PTB in Braunschweig being the German Primary Standard Dosimetry Laboratory. Briefly, the calibration procedure in the reference beam quality Q_0 consists of two steps: First, absorbed dose to water, D_{w,Q_0}, is measured in absolute terms by means of water calorimetry at a reference depth, z_{ref}, in water under reference conditions. In a second step, the very same irradiation is repeated with the calorimetric detector replaced by the ionization chamber to be calibrated, which is positioned with its reference point, P_{ref}, at the same measurement depth z_{ref} as schematically shown in Fig. 3.1 a using the example of a cylindrical ionization chamber. Thus, the calibration factor, N_{D,w,Q_0}, can be directly determined by dividing D_{w,Q_0} by the corresponding ionization chamber reading, M_{Q_0}, corrected for influence quantities:

$$N_{D,w,Q_0} = \frac{D_{w,Q_0}(z_{ref})}{M_{Q_0}(z_{ref})}\,. \tag{3.1}$$

The reference conditions for calibration are described by a set of values of influence quantities affecting the response of the dosimeter. Since many influence quantities, such as temperature and air pressure for example, usually differ in clinical dosimetry from the reference conditions used in the standards laboratory for calibration, a product of appropriate correction factors k_i needs to be applied, which will be discussed in more detail in Sec. 4.2.2. Further, the departure from the reference beam quality, Q_0, to other beam qualities, Q, is accounted for by an additional correction factor, the so called beam quality correction factor k_{Q,Q_0}. Hence, absorbed dose to water measured in a beam of quality Q is given by

$$D_{w,Q} = M_Q \cdot N_{D,w,Q_0} \cdot k_{Q,Q_0}\,, \tag{3.2}$$

assuming that the dosimeter reading, M_Q, has been corrected to the reference values of influence quantities other than beam quality. In the following, the subscript Q_0 will be omitted when the reference beam quality is ^{60}Co. In general, the beam quality correction factor, k_{Q,Q_0}, is defined as the ratio of calibration factors in terms of absorbed dose to water determined at the beam qualities Q and Q_0. In the case of ion beams with Q_0 being ^{60}Co radiation, the k_Q-factor is defined as follows:

$$k_Q = \frac{N_{D,w,Q}}{N_{D,w}} = \frac{\frac{D_{w,Q}}{M_Q}}{\frac{D_w}{M}} . \tag{3.3}$$

Ideally, the beam quality correction factor should be measured directly for each ionization chamber in the user beam quality as recommended by both dosimetry protocols. However, owing to the lack of a primary standard for absorbed dose to water for ion beams, all values for k_Q given in TRS-398 and DIN 6801-1 for ion beams are derived by calculations on the basis of Bragg-Gray cavity theory or Monte Carlo particle transport simulations. Up to now, the k_Q-factor is the main source of uncertainties in the dosimetry of ion beams with ionization chambers calibrated in ^{60}Co radiation.

3.1 Application of calculated k_Q-values according to TRS-398 and DIN 6801-1

Under conditions where the Bragg-Gray cavity theory is valid, the k_Q-factor for ion beams may be calculated as follows:

$$k_Q = \frac{(s_{w,air})_Q}{(s_{w,air})_{Co}} \cdot \frac{(W_{air})_Q}{(W_{air})_{Co}} \cdot \frac{p_Q}{p_{Co}} . \tag{3.4}$$

Here, $s_{w,air}$ is the water-to-air stopping-power ratio (*cf* Sec. 2.1), W_{air} the mean energy expended in air per ion pair formed, and p the pertubation factors at the beam qualities Q and ^{60}Co, which correct all departures from the ideal Bragg-Gray detector conditions.
For an accurate theoretical determination of the k_Q-factor for ion beams, it is desirable to know the energy spectra of the incident ion beam, of the projectile fragments and also of the target fragmented nuclei. However, in the year 2000 when TRS-398 was published, only very few experimental and theoretical data on the spectral distribution of ion beams were available resulting in the simplified characterization of ion beams by means of the atomic number, mass number, energy, width of the spread-out Bragg peak (SOBP) and the range of the incident ion beams disregarding projectile and target fragments. Consequently, simplified values for the physical parameters required for ion dosimetry with ionization chambers are given in TRS-398. In order to ensure international consistency, the German dosimetry protocol DIN-6801-1 is based on TRS-398 comprising three main revisions: (I) The introduction of reference conditions for the dosimetry of monoenergetic ion beams, (II) a more sophisticated method for the determination of the saturation effect (*cf* Sec. 4.2.2.3) and (III) the use of more recent data concerning the water-to-air stopping-power ratios. In order to highlight the main sources of uncertainties contributing to the total uncertainty of the resulting k_Q-factors currently used in clinical dosimetry, each component of k_Q will be discussed separately in what follows emphasizing similarities/differences of the two dosimetry protocols.

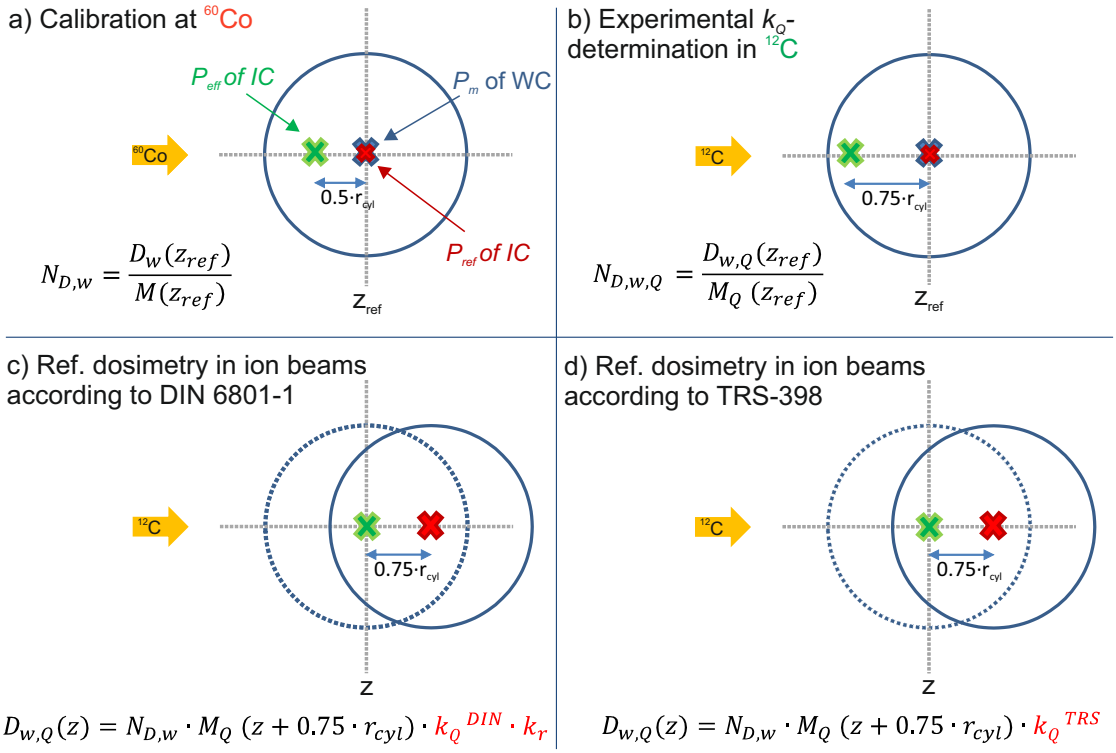

Fig. 3.1: *Positioning of a thimble ionization chamber (top view) during calibration in (a) ^{60}Co radiation and during the experimental k_Q-determination in (b) ^{12}C radiation, as well as for reference dosimetry in ion beams according to DIN 6801-1 (c) and TRS-398 (d). Here, the difference of both protocols concerning the determination of $D_{w,Q}$ is emphasized. IC = ionization chamber, WC = water calorimeter, P_{eff} = effective measurement position of IC, P_{ref} = reference point of IC, P_m = measurement position of WC, z_{ref} = reference depth.*

Water-to-air stopping-power ratio

^{60}Co In TRS-398, $(s_{w,air})_{Co} = 1.133$ is used, which was calculated by Andreo et al. [1986] using the monoenergetic electron stopping-power data tabulated in ICRU [1984] with the density effect correction due to Sternheimer et al. [1984]. The total uncertainty of 0.5 % is separated into a contribution of 0.5 % associated with the uncertainties of the mean excitation energies (I-values) and density effect corrections and a contribution of 0.1 % due to spectral differences between ^{60}Co-beams, which is neglected when assigning a stopping-power ratio to a particular ^{60}Co beam. DIN 6801-1, on the other hand, uses the restricted stopping-power $(s^{\Delta}_{w,air})_{Co}$ according to Spencer and Attix for both water and air taking into account the spectral electron fluence at the measurement depth. This results in $(s^{\Delta}_{w,air})_{Co} = 1.133$ with a reduced uncertainty of 0.1 %.

Ion beams For an accurate theoretical determination of the water-to-air stopping-power ratio for ion beams, $(s_{w,air})_Q$ should be obtained by averaging over the complete spectrum of primary particles and fragments at the reference depth according to the following formula:

$$(s_{w,air})_Q = \frac{\sum_i \int_0^\infty \Phi_{E,i} \cdot (S_i(E)/\rho)_w \, dE}{\sum_i \int_0^\infty \Phi_{E,i} \cdot (S_i(E)/\rho)_{air} \, dE} \,. \tag{3.5}$$

Here, $(S_i(E)/\rho)_m$ is the mass stopping-power at energy E for particle i in medium m and Φ_E the particle fluence differential in energy.
Owing to the lack of spectral data at the time when TRS-398 was published, the stopping-power ratios for ion beams are taken to be independent of the beam quality neglecting the contribution of fragments. Thus, for all ion beams covered by TRS-398, a constant value of $(s_{w,air})_Q = 1.130$ is assumed with an estimated combined standard uncertainty of 2.0 % adopted from Hartmann et al. [1999]. At that time, this value has shown to be the best compromise of $(s_{w,air})_Q$-values calculated using the computer codes developed by Salamon [1980] for helium, carbon, neon and argon ions, by Hiraoka and Bichsel [1995] for carbon ions, and by the ICRU report 49 [ICRU, 1993] for protons and helium, with all values lying in the range from 1.12 to 1.14. In comparison, the determination of $(s_{w,air})_Q$ in DIN 6801-1 is based on the recent work of Lühr et al. [2011] who showed that the stopping-power ratio for ion beams as a function of residual range (*cf* Sec. 2.2), R_{res}, can be assumed in good agreement to be independent of the initial energy and atomic number of the primary ion using the I-values stated in the ICRU report 73 [ICRU, 2005] and corresponding addendum. The following equation approximates the results of Lühr et al. [2011] very well and is thus used in DIN 6801-1 for the residual range-dependent determination of $(s_{w,air})_Q$:

$$(s_{w,air})_Q = 1.1203 - 3.998 \cdot 10^{-5}\, cm^{-1} \cdot R_{res} + \frac{3.942 \cdot 10^{-4}\, cm}{R_{res}} \text{ for } R_{res} \geq 0.03\, cm\,. \quad (3.6)$$

Exemplary, carbon ions with a residual range of 24.1 cm as used for the water calorimetric measurements performed within this thesis (*cf* Ch. 6) amount to $(s_{w,air})_Q = 1.119$. Compared to the beam quality-independent $(s_{w,air})_Q$-value of 1.130 used in TRS-398, the water-to-air stopping-power ratio for carbon ions according to DIN 6801-1 is about 1 % lower. The overall uncertainty of $(s_{w,air})_Q$ is thereby mainly influenced by the inconsistency of I-values (*cf* [ICRU, 2005]) and estimated with 1.5 %.

W-factor

^{60}Co In TRS-398, a value of $W_{air}/e = 33.97\,J/C$ is assumed for dry air ([Niatel et al., 1985], [BIPM, 1985], and [Boutillon and Perroche-Roux, 1987]) with e being the elementary charge. The uncertainty is estimated with 0.2 % according to Niatel et al. [1985]. The same value of W_{air}/e including the given uncertainty is adopted in DIN 6801-1.

Ion beams As discussed for the water-to-air stopping-power ratio for ion beams, also the value for $(W_{air})_Q$ should ideally be obtained by averaging over the complete particle spectrum with $w_i(E)$ being the differential value of W at energy E for particle i:

$$\left(\frac{\overline{w}}{e}\right)_Q = \frac{\sum_i \int_0^\infty \Phi_{E,i} \cdot (S_i(E)/\rho)_{air}\, dE}{\sum_i \int_0^\infty \frac{\Phi_{E,i} \cdot (S_i(E)/\rho)_{air}}{(w_i(E)/e)_{air}}\, dE}\,. \quad (3.7)$$

However, at the time of TRS-398, only a few experimental investigations of $(W_{air})_Q$ for high-energy ion beams existed. Thus, a beam-quality dependent determination of $\left(\frac{\overline{w}}{e}\right)_Q$ under consideration of the complete particle spectrum was not possible. Therefore, a constant value of $(W_{air}/e)_Q = 34.50\,J/C \pm 1.5\,\%$, which is the uncertainty-weighted median of $(W_{air}/e)_Q$-values for different ions existing at that time (*cf* Tab. 43 in [IAEA, 2000]), is adopted in TRS-398 for all ion beams. As experimental data for $(W_{air})_Q$ is still limited and only exists

for a few ion types (*e.g.* [Rossomme et al., 2014], [Giesen and Beck, 2014], [Sakama et al., 2009] and references therein), a beam-quality dependent determination of $\left(\frac{\bar{w}}{e}\right)_Q$ according to the above formula is also not possible in the year 2016. Thus, in accordance to TRS-398, a value of $(W_{air}/e)_Q = 34.50 J/C \pm 1.5\,\%$ is assumed for dry air in DIN 6801-1 for all ions and energies covered.

Pertubation factor

The chamber-specific pertubation factor consists of a product of four independent components p_i, which take the individual departures from the ideal Bragg-Gray detector conditions into account:

$$p = p_{cav} \cdot p_{dis} \cdot p_{wall} \cdot p_{cel} \,. \tag{3.8}$$

The meaning of the components is described in detail in Sec. 1.6 of IAEA [2000], while only the displacement correction factor, p_{dis}, will be discussed here as it plays an important role in understanding the difference between TRS-398 and DIN 6801-1. Briefly, p_{dis} accounts for the fact that a cylindrical chamber cavity with its center (reference point, P_{ref}) positioned at the reference depth, z_{ref}, actually samples the electron fluence at a point which is closer to the radiation source than z_{ref}. This effect can either be accounted for by applying the corresponding correction or by displacing the chamber by an amount Δz, which compensates for this effect. The later case is often referred to as the use of the effective point of measurement, P_{eff}. Depending on the beam quality, different regulations for the positioning of the ionization chamber exist leading to a different handling of the displacement effect in order to allow for an accurate determination of D_w.

^{60}Co As explained in the beginning of this chapter, the reference point P_{ref} of an ionization chamber is positioned at z_{ref} during calibration in ^{60}Co radiation. With respect to this radiation quality, P_{eff} is located $\Delta z_{Co} = 0.5 \cdot r_{cyl}$ closer to the impinging beam, with r_{cyl} being the inner radius of the chamber (Fig. 3.1 a). Hence, the value for $N_{D,w}$ determined under calibration conditions needs to be corrected for the displacement effect in order to be applicable to measurements where P_{eff} is located at z_{ref}. While in TRS-398 the displacement correction for ^{60}Co is considered in p_{Co} according to Eq. 3.8, DIN 6801-1 separately addresses this effect by introducing a further correction factor k_r, which can be derived from the requirement that the dose determined at z_{ref} needs to be independent of the displacement correction method chosen:

$$\begin{aligned} M(z_{ref}) \cdot N_{D,w} &\stackrel{!}{=} M(z_{ref} + \Delta z_{Co}) \cdot N_{D,w} \cdot k_r \\ \text{with } M(z_{ref} + \Delta z_{Co}) \approx M(z_{ref}) \cdot (1 + \delta_{Co} \cdot \Delta z_{Co}) &= M(z_{ref}) \cdot (1 + \delta_{Co} \cdot 0.5 \cdot r_{cyl}) \\ \Rightarrow k_r &= \frac{1}{(1 + \delta_{Co} \cdot 0.5 \cdot r_{cyl})} \,. \end{aligned} \tag{3.9}$$

Here, δ_{Co} is the relative depth dose gradient of ^{60}Co radiation at z_{ref} given by $-0.006\,mm^{-1}$ and $M(z_{ref} + \Delta z_{Co})$ is approximated by the first two terms of a Taylor expansion. Thus, care has to be taken when comparing the pertubation factors given in TRS-398 and DIN 6801-1 and with that the corresponding k_Q-factors. In order to convert the values for p_{Co}^{TRS} into p_{Co}^{DIN}, the following relation needs to be used:

$$p_{Co}^{DIN} = p_{Co}^{TRS} \cdot k_r \,. \tag{3.10}$$

	DIN 6801-1 draft	**TRS-398**
$D_w(z)$	$N_{D,w} \cdot M(z+0.75r_{cyl}) \cdot k_r \cdot k_Q^{DIN}$	$N_{D,w} \cdot M(z+0.75r_{cyl}) \cdot k_Q^{TRS}$
k_Q	$\frac{(s_{w,air})_Q}{(s^{\Delta}_{w,air})_{Co}} \cdot \frac{(W_{air})_Q}{(W_{air})_{Co}} \cdot \frac{p_Q}{p_{Co}}$	$\frac{(s_{w,air})_Q}{(s_{w,air})_{Co}} \cdot \frac{(W_{air})_Q}{(W_{air})_{Co}} \cdot \frac{p_Q}{p_{Co}}$
$(s_{w,air})_Q$	Eq. 3.6 ($\pm 1.5\,\%$)	1.130 ($\pm 2.0\,\%$)
$(s_{w,air})_{Co}$	1.133 ($\pm 0.1\,\%$)	1.133 ($\pm 0.5\,\%$)
$\left(\frac{W_{air}}{e}\right)_Q$	34.50 $\frac{J}{C}$ ($\pm 1.5\,\%$)	34.50 $\frac{J}{C}$ ($\pm 1.5\,\%$)
$\left(\frac{W_{air}}{e}\right)_{Co}$	33.97 $\frac{J}{C}$ ($\pm 0.2\,\%$)	33.97 $\frac{J}{C}$ ($\pm 0.2\,\%$)
p_Q	1.0 ($\pm 0.1\,\%$)	1.0 ($\pm 1.0\,\%$)
p_{Co}	$p_{Co}^{DIN} = p_{Co}^{TRS} \cdot k_r$ ($\pm 0.6\,\%$)	Tab. 37 in TRS-398 ($\pm 0.6\,\%$)
$\frac{\Delta k_Q}{k_Q}$	2.2 %	2.8 %

Table 3.1: *Comparison of TRS-398 and DIN 6801-1 (draft) concerning the procedure of reference dosimetry for ion beams ($2 \geq Z \leq 18$ for TRS-398 and $2 \geq Z \leq 10$ for DIN 6801-1) with calibrated air-filled thimble ionization chambers. The values and relative measurement uncertainties given are taken from IAEA [2000] and DIN [2016].*

The chamber-specific p_{Co}-values given in Tab. 37 of TRS-398 have an overall standard measurement uncertainty of 0.6 %, which is dominated by the uncertainties of p_{wall} (0.5 %) and p_{dis} (0.3 %). These values are adopted in DIN 6801-1 according to Eq. 3.10 supplemented with values for additional chambers taken from Muir and Rogers [2010] assuming an overall standard measurement uncertainty of 0.6 %.

Ion beams With respect to ion beams, both dosimetry protocols recommend the use of P_{eff} in order to account for the displacement effect. Therefore, P_{ref} has to be positioned $0.75 \cdot r_{cyl}$ deeper than z_{ref}. By doing so, P_{eff} of the chamber is positioned at z_{ref} and thus the measured value directly refers to the reference depth without the need for an additional correction (Fig. 3.1 c, d). Due to the non-availability of information concerning the other components of the overall pertubation correction factor, p_Q is assumed to be identical to unity in TRS-398 with an estimated uncertainty of 1.0 % according to the work of Hartmann et al. [1999]. As experimental data on pertubation factors is still very limited at the time of DIN 6801-1, the German dosimetry protocol also recommends $p_Q = 1.0$ with a reduced standard measurement uncertainty of 0.1 % assuming a negligible departure from the ideal Bragg-Gray detector conditions due to the comparably low energies of secondary electrons occurring in ion beam radiation.

Conclusion

As summarized in Tab. 3.1, the overall uncertainty associated with the calculated k_Q-factor of ion beams accounts to 2.8 % in the case of TRS-398 and 2.2 % in the case of DIN 6801-1, respectively. The lower uncertainty of the k_Q-factor stated in DIN 6801-1 is mainly caused by the availability of more accurate water-to-air stopping-power ratios for ion beams as well

as the reduced uncertainty in the determination of $s_{w,air}$ with respect to ^{60}Co radiation by using the restricted stopping-power values according to Spencer and Attix, although this new calculation does not change the value itself. Further, a significantly reduced uncertainty for p_Q is assumed in DIN 6801-1. In both protocols, the uncertainty of the k_Q-factor for ion beams is dominated by those of the stopping-power ratio and W-value for the user beam quality Q. As emphasized in Tab. 3.1, it is important to note that k_Q^{DIN} and k_Q^{TRS} are only valid in combination with the corresponding equation for the determination of $D_{w,Q}$ given in DIN 6801-1 and TRS-398, respectively, as $\frac{p_Q}{p_{Co}}$ is handled differently in both protocols resulting in a systematic difference of k_Q^{DIN} and k_Q^{TRS}.

3.2 Experimental k_Q-values

According to Eq. 3.3, the k_Q-factor for ion beams can be experimentally determined by a direct calibration of an ionization chamber in terms of absorbed dose to water in the user beam quality Q by means of a primary standard for the determination of $D_{w,Q}$. Both TRS-398 and DIN 6801-1 recommend the use of experimentally determined k_Q-factors instead of the calculated k_Q-factors given in the protocols, if the corresponding uncertainty is sufficiently low. However, as a primary standard for the determination of $D_{w,Q}$ does not exist yet, experimental k_Q-factors for ion beams are not available in the dosimetry protocols up to now. In terms of clinically used proton beams, recent work using water calorimetry for the experimental determination of k_Q has been for example carried out by Medin [2010] and Sarfehnia et al. [2010]. With respect to carbon ion beams, however, only a very limited number of work has been performed so far with the most recent work by Rossomme et al. [2014] and Sakama et al. [2009], which both used graphite calorimetry for the absolute determination of $D_{w,Q}$, rather concentrating on the experimental determination of the $(W_{air})_Q$-factor. Thus, one major aim of this thesis is the implementation of water calorimetry for the absolute determination of $D_{w,Q}$ in the clinical carbon ion beam at HIT in order to determine $N_{D,w,Q}$ analogue to the calibration procedure described in the beginning of this chapter for ^{60}Co radiation at PTB. Following this established procedure, $N_{D,w,Q}$ is given by

$$N_{D,w,Q} = \frac{D_{w,Q}(z_{ref})}{M_Q(z_{ref})} \,, \tag{3.11}$$

with the corresponding ionometric and calorimetric measurements performed at z_{ref} in water as schematically shown in Fig. 3.1 b. Thus, the k_Q-factor can be determined as the ratio of $N_{D,w,Q}$ and the well-known calibration factor $N_{D,w}$ in terms of ^{60}Co reference radiation.
However, it is important to note that this experimentally determined k_Q-factor, which will be referred to as k_Q^{cal} in the following, is not directly comparable with the k_Q-factors stated in TRS-398 and DIN 6801-1. As discussed before, both protocols recommend the use of P_{eff} by positioning the reference point of the chamber, P_{ref}, $0.75 \cdot r_{cyl}$ deeper than z_{ref}. Thus, in order to use k_Q^{cal} for the reference dosimetry of ion beams according to DIN 6801-1 and TRS-398, k_Q^{cal} has to be transformed into k_Q^{DIN} and k_Q^{TRS}, respectively. As discussed before for the derivation of k_r (Eq. 3.9), $D_{w,Q}$ determined at z_{ref} needs to be independent of the

protocol and with that positioning restriction used:

$$\begin{aligned} M(z_{ref}) \cdot k_Q^{cal} &\stackrel{!}{=} M(z_{ref} + \Delta z_{^{12}C}) \cdot k_Q^{DIN} \cdot k_r \\ \text{with } M(z_{ref} + \Delta z_{^{12}C}) &\approx M(z_{ref}) \cdot (1 + \delta_{^{12}C} \cdot 0.75 \cdot r_{cyl}) \\ \Rightarrow k_Q^{DIN} &= \frac{k_Q^{cal}}{k_r \cdot (1 + \delta_{^{12}C} \cdot 0.75 \cdot r_{cyl})} \, . \end{aligned} \tag{3.12}$$

Here, $\Delta z_{^{12}C}$ is the shift needed in order to account for the displacement effect in ^{12}C radiation and $\delta_{^{12}C}$ the relative depth dose gradient at z_{ref} in the carbon ion field used for calibration. Analogue, k_Q^{TRS} and k_Q^{cal} relate as follows:

$$M(z_{ref}) \cdot k_Q^{cal} \stackrel{!}{=} M(z_{ref} + \Delta z_{^{12}C}) \cdot k_Q^{TRS} \;\Rightarrow\; k_Q^{TRS} = \frac{k_Q^{cal}}{1 + \delta_{^{12}C} \cdot 0.75 \cdot r_{cyl}} \, . \tag{3.13}$$

Chapter 4

Materials and Methods

4.1 Water calorimeter

Water calorimetry is used in several standard laboratories worldwide as a primary standard for absorbed dose determination in ^{60}Co γ-radiation as well as for high-energy x-rays [Seuntjens and Duane [2009] and references therein], since it allows to measure D_w in the most fundamental way with low standard measurement uncertainty without the need for energy-dependent corrections. The water calorimetric measurement of absorbed dose to water is based on the measurement of the radiation-induced temperature rise, ΔT, which amounts only to about 0.24 mK per deposited Gray. In the following section, the detector design and principle of operation allowing to accurately measure such small temperature increases will be explained. Afterwards, in Sec. 4.1.2, the determination of absorbed dose to water from the measured radiation-induced temperature rise will be discussed in general emphasizing influence quantities and their corrections, while distinctiveness as well as challenges due to the irradiation with carbon ion beams will be discussed in detail in Chapter 6. Please note that some of the correction factors described in Sec. 4.1.2 are not necessary for the calorimetric determination of D_w, but to ensure comparable calorimetric and ionometric measurement conditions for an accurate subsequent determination of k_Q. As explained in Sec. 3.2, both calorimetric and ionometric measurements for the determination of k_Q are performed at the same reference depth z_{ref}. However, as the ionometric measurements are performed at room temperature while the calorimetric measurements take place at 4 °C, the absolute measurement depth slightly differs, which is accounted for by k_d (Sec. 4.1.2.5). Further, as will be described in the following section, the lateral position of the calorimetric measurements slightly deviates from the central axis where the ionometric measurements take place, as the thermistor probes in the calorimetric detector have a small lateral off-set due to the specific detector design used. Thus, in order to ensure comparable lateral measurement positions, this effect is corrected for by k_l (Sec. 4.1.2.4). If not otherwise stated, the following descriptions are based on [Krauss, 2006b], [Krauss, 2006a] and [Krauss et al., 2012].

4.1.1 Detector design and principle of operation

For the measurements performed within this thesis, the transportable water calorimeter developed by PTB has been used, which is shown in Fig. 4.1. As the water calorimeter is operated at a water temperature of 4 °C to control heat convection (*cf* Sec. 4.1.2.2) and the radiation-induced temperature increase to be measured is very small (0.24 mK per Gy), the

cubic water phantom of 30 cm edge length has to be thermally insulated against the room temperature. This is realized by actively cooled aluminum plates which are sandwiched between two 5 cm thick layers of styrofoam. Except for the radiation entrance window, where the thickness of the styrofoam layer shielding the water phantom from room temperature is increased to 20 cm, the whole water phantom is surrounded by this structure. All six aluminum plates contain a meander-like structure of cooling channels, which are connected to an external cooling unit capable of stabilizing the temperature of the cooling plates to better than $\pm 0.01\,^{\circ}\mathrm{C}$. In addition, the cooling liquid is by-passed to a stainless steel tube inside the water phantom to accelerate the cooling procedure from room temperature to 4 °C. Still, it takes about 7 h to cool down the permanently mixed water slightly below 4 °C and another 12 h without active cooling of the steel tube inside the water phantom to reach thermal equilibrium and to decrease the remaining temperature drifts by additionally turning off the mechanical stirrer enabling conditions suitable for calorimetric measurements.

The measurement of the radiation-induced temperature increase takes place in a thin-walled plane-parallel glass cylinder, which is fixed in a support structure of PMMA as shown in Fig. 4.2 b. The glass cylinder is mounted inside the water phantom of the calorimeter with the cylinder axis oriented parallel to the beam direction (Fig. 4.2 a). The cylinder is filled with high-purity water (total organic component less than 4 ppb) saturated with hydrogen in order to control the heat defect (*cf* Sec. 4.1.2.2), while the surrounding water in the water phantom is simple distilled water. ΔT is separately measured inside the glass cylinder by two

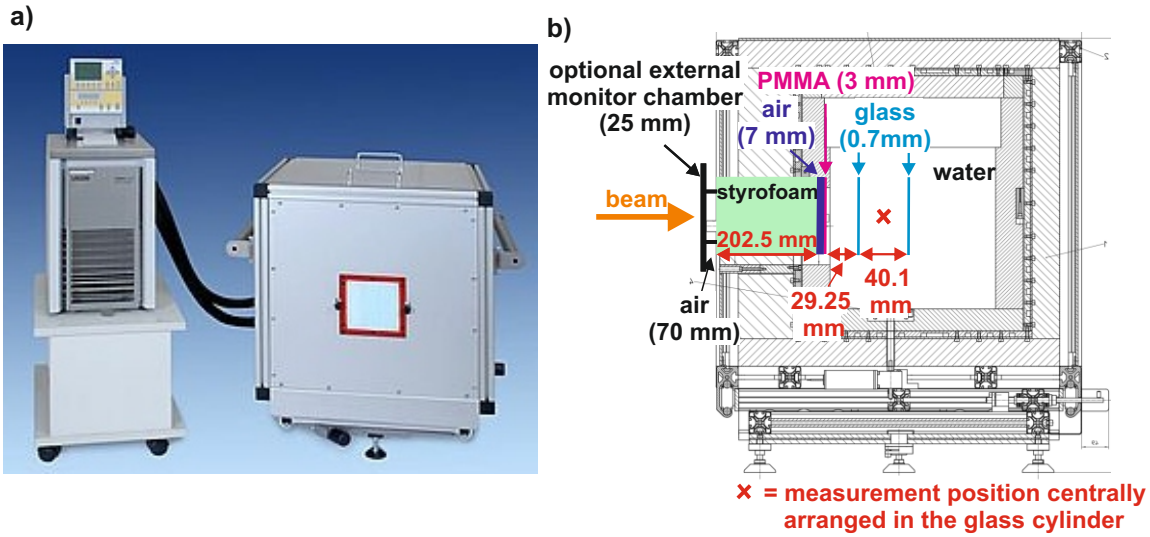

Fig. 4.1: *a) A picture of the transportable PTB water calorimeter having an almost cubic shape of 60 cm edge length is shown with the associated cooling unit on the left side. The water phantom inside the housing is made of 1 cm thick poly(methyl methacrylate) (PMMA) walls, which are reduced to 3 mm thickness at the radiation entrance window (about $12 \times 12\,\mathrm{cm}^2$ of size) shown in the middle of the calorimeter housing (reprinted from [Krauss, 2006a]). The materials of the calorimeter passed by the radiation are schematically illustrated in b). The distances given refer to a nominal measuring depth of the thermistor probes of 50 mm with respect to the inner surface of the PMMA entrance window. The external air-filled large-area ionization chamber has been mounted in front of the water calorimeter to additionally monitor the beam stability during the irradiations. Please note that the schematic drawing is not true to scale in the sake of better illustration of thin materials.*

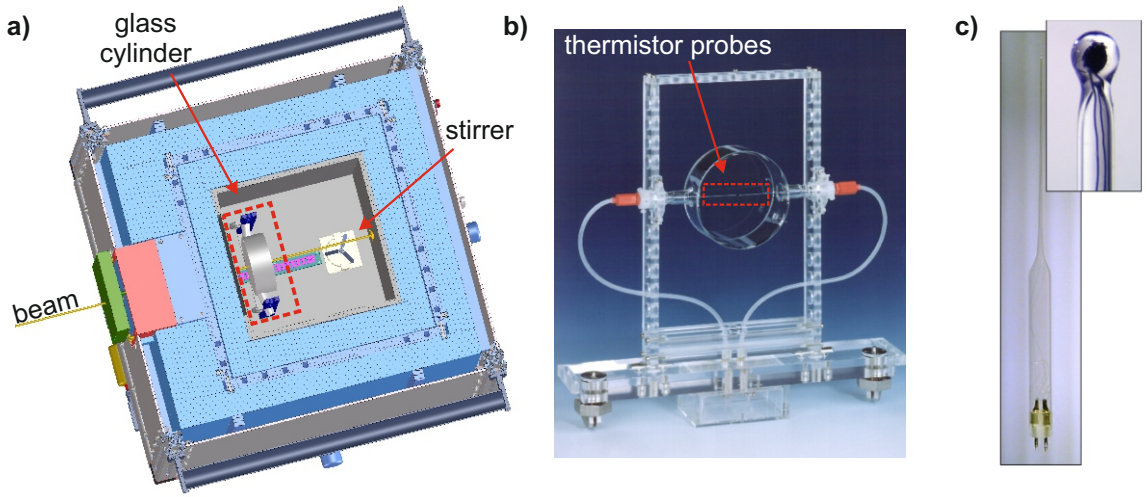

Fig. 4.2: *a) Top view inside the water calorimeter showing the position of the glass cylinder, which is placed inside the water phantom such that the radiation beam passes the cylinder parallel to its axis. Further, the magnetically coupled stirrer is depicted, which is used to accelerate the achievement of thermal equilibrium inside the water phantom. The glass cylinder (outside ∅: 95 mm, outside length: 41.5 mm, thickness of front/rear wall: 0.7 mm) in the PMMA support structure is shown upside down in b), with the two thermistor probes centrally arranged opposite of each other. One of the two thermistor probes is enlarged depicted in c) showing the thermistor (∅ 0.25 mm) fused in the tip of the glass pipette (∅ 0.5 mm) having a total length of about 110 mm. Figure b) and c) reprinted from [Krauss, 2006b].*

thermistors, which consist of semiconductor material and therefore exhibit a temperature-dependent resistance change according to the following equation:

$$R_{th} = R_{th,0} \cdot e^{B\left(\frac{1}{T}-\frac{1}{T_0}\right)} \,. \tag{4.1}$$

Here, R_{th} is the thermistor resistance as a function of temperature, T, $R_{th,0}$ the resistance at temperature T_0, and B a material parameter of the thermistor. The thermistor sensitivity, S, which is the relative resistance change with temperature, is thus given by

$$S = \frac{1}{R_{th}} \frac{\partial R_{th}}{\partial T} = -\frac{B}{T^2} \,. \tag{4.2}$$

Via a careful calibration procedure performed at PTB, the thermistor-specific sensitivity can be experimentally obtained with a relative standard uncertainty of 0.07 % [Krauss, 2006b]. This allows for an accurate determination of the radiation-induced temperature rise, ΔT, according to

$$\Delta T = \frac{1}{S} \cdot \frac{\Delta R_{th}}{R_{th}} \,. \tag{4.3}$$

by measuring $\frac{\Delta R_{th}}{R_{th}}$ during a water calorimetric measurement. It is further known from calibration that the electrical power, P, of the thermistors causes their temperature levels to be raised by a factor of about $dT/dP = 1.2\,\mathrm{mK/\mu W}$ with respect to the surrounding water temperature. As the radiation-induced decrease in the thermistor resistance causes a decrease of the thermistor´s electrical power, the temperature level of the thermistor decreases during the

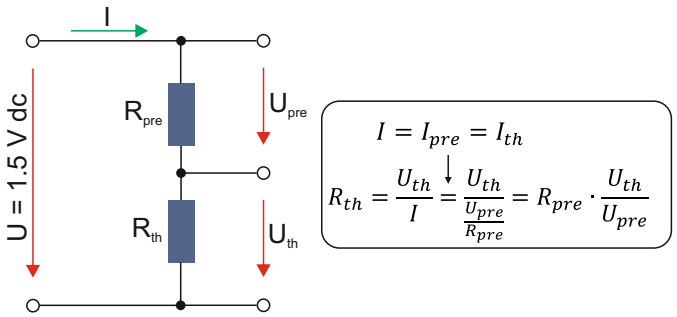

Fig. 4.3: *Voltage divider circuit for the determination of R_{th} operated with a 1.5 V battery.*

course of an calorimetric measurement which needs to be taken into account in order to accurately determine ΔT (*cf* Sec. 4.1.2.6). The thermistors are fused in the conically shaped tip of a glass pipette as shown in Fig. 4.2 c. The glass pipettes themselves are centrally arranged inside the glass cylinder perpendicular to the cylinder axis, with the two thermistors facing each other having a distance of about 7 mm (Fig. 4.2 b). The glass cylinder is positioned inside the water phantom such that the measurement depth of the thermistors with respect to the beam entrance window of the water phantom is nominally set to 50 mm as schematically shown in Fig. 4.1 b.

The resistance of each thermistor is independently measured within a separate voltage divider circuit as illustrated in Fig. 4.3. The thermistor, having a resistance of about 10 kΩ, forms one part of the voltage divider and a calibrated precision pre-resistor of about 20 kΩ the second part. By measuring the voltage drop across each part of the voltage divider with two high-stability digital multimeters (Agilent 3588A) in time intervals of 0.1 s, R_{th} can be determined according to the formula given in the figure. The time-dependent evolution of R_{th} is then recorded with 1 Hz as average over 10 sampled values each. In addition, the water temperature, T, within the calorimeter is determined with an calibrated PT-100 sensor throughout the calorimetric measurements, as T is needed for the determination of S.

The measurement procedure as well as the analysis of the recorded thermistor signals will be described in Sec. 6.4 with respect to the specific water calorimetric measurements performed within this thesis.

4.1.2 Determination of absorbed dose to water and its influence quantities

By measuring the radiation-induced temperature rise, ΔT, according to Eq. 4.3, the absorbed dose to water at the position of the measuring thermistor is given by

$$D_w = \Delta T \cdot c_p \cdot k_h \cdot k_c \cdot k_p \cdot k_l \cdot k_d \cdot k_e \, . \tag{4.4}$$

Here, c_p is the specific heat capacity of water and the k-factors denote several correction factors, which will be discussed in detail in the following. For water at 4 °C, a c_p-value of 4206.8 J kg^{-1} K^{-1} [Kohlrausch, 1996] is used with a relative standard measurement uncertainty of 0.03 % [Krauss, 2006b].

4.1.2.1 Heat defect k_h

Radiation-induced exothermic or endothermic chemical reactions can directly influence the energy balance in water and with that the measured quantity ΔT. In the case of an exothermic reaction for example, the energy appearing as heat, E_h, will be larger than the absorbed radiation energy, E_a, causing an overestimation of D_w if not corrected. This effect is called heat defect and corrected for by applying the following corresponding correction factor:

$$k_h = \frac{E_a}{E_h} \,. \tag{4.5}$$

Thus, k_h is greater 1.0 in the case of an endothermic reaction ($E_a > E_h$) and smaller 1.0 in the case of an exothermic reaction ($E_a < E_h$).
Extensive experimental and theoretical investigations have been performed in the past leading to a proper understanding of the heat defect as well as its precise prediction for different systems based on model calculations for the radiolysis (*e.g.* [Klassen and Ross, 1997], [Klassen and Ross, 2002] and references therein). In the case of hydrogen-saturated water as used within this thesis, it has been shown for ^{60}Co γ-radiation that the assumption of a zero heat defect after a small pre-irradiation dose is reasonable within a relative standard uncertainty of 0.14 % [Krauss, 2006b]. The transfer to high-LET radiation such as clinical carbon ion beams will be elaborated in Sec. 6.4.1.1.

4.1.2.2 Heat conduction effects k_c

In order to ensure a correct measurement of ΔT, heat transport taking place during and after a calorimetric measurement needs to be adequately corrected for. In principle, heat can be transported by three different mechanisms, namely convection, radiation, and conduction. Heat transport via radiation can be neglected, as water calorimetry is performed at 4 °C and typical radiation-induced temperature rises during a measurement are only in the order of a few mK (0.24 mK per Gy). Further, as water has its maximal density at 4 °C, the variation of density due to the radiation-induced temperature increase is sufficiently small avoiding convection effects. However, heat conduction effects arising during and after the irradiation of the water calorimeter cannot be neglected, although they are already reduced to a minimum by an elaborate construction of the calorimeter. These effects are due to the (I) irradiation of the non-water materials of the calorimetric detector (glass cylinder and thermistor probes) having lower specific heat capacities and mass-energy-absorption coefficients compared to water, which thus results in higher temperature increases during irradiation, as well as (II) temperature gradients in water, which are caused by the dose distribution (laterally and in depth) itself. Briefly, heat conduction corrections, k_c, are based on the results of finite-element heat conduction calculations precisely reproducing the real calorimetric measurement conditions and are defined as the ratio of a calorimetric result without and with influence of the heat conduction effects. The radiation-dependent heat generation rates necessary for the finite-element models are typically derived from measured lateral and depth dose distributions, which are then adequately fitted to generate mathematical expressions applicable within the finite-element calculation. Heat conduction effects due to the irradiation of the non-water materials of the detector have been extensively studied in [Krauss, 2002] and [Krauss and Roos, 1999], while additional heat conduction effects due to different lateral field sizes and depth dose distributions have been studied in [Krauss, 2006a]. A detailed comparison of experimental and simulated data performed by Krauss [2006b] has proven

that the heat conduction effects in the PTB water calorimeter can be adequately predicted by model calculations for time periods of more than 45 min, which is the time needed for a typical series of successive irradiations.

4.1.2.3 Radiation field pertubation correction k_p

Due to the presence of the calorimetric detector consisting of the glass cylinder and the thermistor probes (Fig. 4.2 b), the radiation field is perturbed at the measurement position. The corresponding correction factor can experimentally be determined by using a 'dummy' detector having the same dimensions as the glass cylinder of the calorimetric detector but with a small opening in the cylinder wall to place a thimble ionization chamber inside. k_p can then be determined as the ratio of the ionization chamber reading without and with the glass cylinder present. As no difference in the ionization chamber reading has been found in ^{60}Co γ-radiation when addionally using short glass pipettes placed inside the dummy detector simulating the thermistor probes [Krauss, 2006b], no glass pipettes have been used within this thesis for the determination of k_p.

4.1.2.4 Correction for lateral measurement position k_l

This factor considers the non-uniformity of the lateral dose distribution which creates a difference between the dose deposited at the central axis of the radiation field where the ionometric measurements take place and the dose at the position of the thermistor probes. In order to achieve comparable measurements conditions between the ionometric and calorimetric dose determination necessary for the subsequent determination of k_Q, the value of D_w measured off-axis with each thermistor is individually corrected to the dose deposited at the central axis. Therefore, the relative lateral dose distribution needs to be measured with high accuracy and spatial resolution.

4.1.2.5 Correction for measurement position in depth k_d

As the measurements with the water calorimeter are carried out at a water temperature of 4 °C while the ionometric measurements are performed for practical reasons at room temperature, the same geometrical depth in water of nominally 50 mm used for both calorimetric and ionometric measurements corresponds to slightly different water depth due to the temperature-dependent density of water. In order to achieve comparability with the ionometric measurements and thus allow for an accurate subsequent determination of k_Q, k_d is applied to the calorimetrically determined D_w considering the relative depth dose gradient in water at the point of measurement as well as the difference in water density.

4.1.2.6 Correction for a change in the thermistor´s electrical power k_e

As described in Sec. 4.1.1, the electrical power of the thermistors causes their temperature levels to be above the surrounding water temperature. k_e is a minor correction factor which considers the influence of the change of the thermistor's electrical power during irradiation on the determination of the radiation-induced temperature rise ΔT.

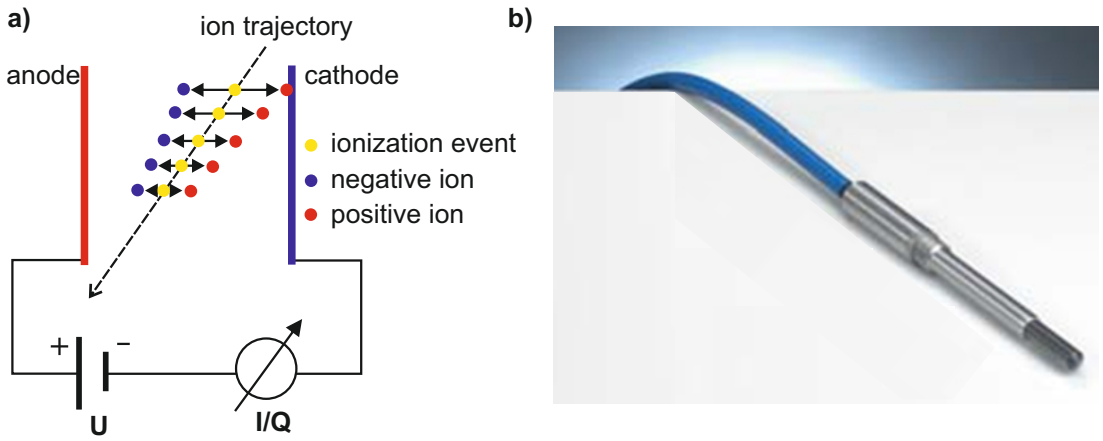

Fig. 4.4: *In a) the basic principle of an ionization chamber is illustrated, while b) shows the picture of a typical thimble ionization chamber (here: TM30013 by PTW (Freiburg, Germany), reprinted and modified from [PTW, 2013a])*

4.2 Ionization chamber

The main ionization chambers used within this thesis are the air-filled Farmer-type ionization chambers TM30013 by PTW (Freiburg, Germany) and FC65-G by IBA (Schwarzenbruck, Germany). The detector design as well as a brief description of the general detection principle of an ionization chamber will be given in Sec. 4.2.1. Afterwards, the ionometric determination of absorbed dose to water and its uncertainties will be discussed limiting the variety of correction factors to the ones used within this thesis.

4.2.1 Detector design and principle of operation

The basic principle of an ionization chamber is schematically illustrated in Fig. 4.4 a using the example of an parallel-plate ionization chamber. Similar to a parallel-plate capacitor, an electric field is applied to the detection volume of the ionization chamber. If an ion passes the volume, ionization events take place generating positive and negative charge carriers. Due to the applied electric field, the charge carriers are separated and move to the anode/cathode, respectively. Thus, ionomoetric measurements are based on the measurement of radiation-induced free charge carriers. If the W-factor for the measuring medium as well as its mass are known, absorbed dose to water can in principle be determined in absolute terms using an ionization chamber. However, in clinical practice it is more convenient to apply the $N_{D,w}$-based formalism as described in Chapter 3 by calibrating ionization chambers in terms of absorbed dose to water against a primary standard.
The TM30013 and FC65-G ionization chambers used within this thesis are air-filled thimble ionization chambers with a picture of the TM30013 exemplary shown in Fig. 4.4 b. The main components and dimensions of the chambers are summarized in Tab. 4.1 with the ^{60}Co calibration factors and corresponding corrections given in Tab. 4.2. For the read-out of the ionization chambers, two different electrometers have been used: the medical product UNIDOS by PTW (Freiburg, Germany) and a high-precision electrometer system developed by PTB.

Quantity	FC65-G, IBA	TM30013, PTW
Active medium	air	air
Active volume	0.65 cm^3 (l: 23 mm, ∅: 6.2 mm)	0.60 cm^3 (l: 23 mm, ∅: 6.1 mm)
Thickness of outer electrode	0.45 mm graphite	0.335 mm PMMA, 0.09 mm graphite
Inner electrode	∅: 1.0 mm, Al	∅: 1.1 mm, Al
Reference point as distance from chamber thimble	13 mm	13 mm

Table 4.1: *Overview of the most important characteristics of the thimble ionization chambers used within this thesis taken from the detector manuals [IBA, 2013] and [PTW, 2013a].*

4.2.2 Determination of absorbed dose to water and its influence quantities

As described in Chapter 3, the measurement conditions for the determination of absorbed dose to water in clinical dosimetry usually differ from the reference conditions used in the standards laboratory for calibration. Thus, in addition to the beam quality correction factor, k_Q, a product of appropriate correction factors k_i has to be applied to the uncorrected reading of the ionization chamber, M_Q^*, in order to account for the effect of deviating influence quantities. Thus, absorbed dose to water measured in a beam of quality Q is given by

$$D_{w,Q} = M_Q^* \cdot N_{D,w} \cdot k_Q \cdot \prod_i k_i \, . \tag{4.6}$$

In the following, the correction factors used for the ionometric measurements performed within this thesis will be described according to the recommendations given in the dosimetry protocols TRS-398 [IAEA, 2000] and DIN [2016].

4.2.2.1 Temperature and pressure correction k_ρ

Since the used ionization chambers are open to the ambient air, atmospheric variations effect the mass of air in the chamber cavity. Thus, the following correction factor, k_ρ, has to be applied in order to correct for the different air temperature T and pressure p in the cavity of the ionization chamber with respect to the reference conditions T_0 and p_0:

$$k_\rho = \frac{p_0 \cdot T}{p \cdot T_0} \, . \tag{4.7}$$

If the calibration factor of an ionization chamber refers to a relative humidity of 50 %, no further correction has to be applied for measurements performed at a relative humidity between 20 % and 80 %.

4.2.2.2 Polarization effect k_{pol}

The polarization effect describes the change in the dosimeter reading when changing the polarity of the chamber voltage. The effect can be explained by a difference in the number of charge carriers, which enter/exit (depending on the polarity) the measuring electrode from

Chamber	$N_{D,w}$	$k_{pol,Co}$	$k_{s,Co}$
FC65-G S/N 2978	4.8086e7 Gy/C $\pm$ 0.25 %	1.001	1.001
TM30013 S/N 7659	5.3773e7 Gy/C $\pm$ 0.25 %	0.999	1.001
TM30013 S/N 1714	5.383e7 Gy/C $\pm$ 0.55 %	< 0.2 %	1.000

Table 4.2: *$N_{D,w}$ calibration factors and corresponding corrections for saturation and polarity for ^{60}Co radiation. The FC65-G S/N 2978 and TM30013 S/N 7659 have been calibrated at PTB under following reference conditions: Q_0: ^{60}Co, T_0: 20 °C, p_0: 1013.25 hPa, rel. humidity: 50 %, potential of chamber thimble: 0 V for FC65-G and +250 V for TM30013, potential of central electrode: +250 V for FC65-G and 0 V for TM30013. While $k_{pol,Co}$ has been determined experimentally at PTB, $k_{s,Co}$ is taken from [Derikum, 2003]. Both correction factors have not been applied during calibration with the given standard uncertainties for the calibration factors already considering possible uncertainty contributions of the saturation and polarity effect. The TM30013 S/N 1714 has been calibrated at PTW under equal reference conditions as stated for the calibration performed at PTB, with the only exception that a potential of +400 V has been applied. Here, $N_{D,w}$ is corrected for the saturation effect but not for the polarity effect.*

the surrounding material. The true reading of the dosimeter is taken to be the mean of the absolute values measured at both polarities. Since a single polarizing potential and polarity is commonly used in clinical dosimetry, this effect is accounted for by applying the so called polarization correction factor k_{pol}. As the polarity effect depends besides the polarizing potential, polarity, and design of the ionization chamber also on the beam quality, k_{pol} has to be determined individually for each ionization chamber in the user beam quality Q and accounted for by

$$k_{pol} = \frac{|M_1| + |M_2|}{2 \cdot |M_1|} \,. \tag{4.8}$$

Here, M_1 is the dosimeter reading at the commonly used polarity and M_2 the corresponding value at opposite polarity.
If the $N_{D,w}$ calibration factor for ^{60}Co radiation is influenced by the polarity effect under reference conditions, a modified k_{pol} has to be applied:

$$k_{pol} = \frac{k_{pol,Q}}{k_{pol,Co}} \,. \tag{4.9}$$

4.2.2.3 Saturation effect k_s

The recombination of ions taking place within the cavity of an ionization chamber leads to an incomplete collection of charge during an ionometric measurement and can thus result in an incorrect determination of dose if uncorrected. In general, two types of recombination processes are differentiated: (I) general (or volume) recombination due to the recombination of ions formed by separate ionizing particle tracks and (II) initial recombination, which is caused by the recombination of ions formed by a single ionizing particle track. While initial recombination is independent of dose rate, general recombination shows a strong dependency as it relies on the density of ionizing particle tracks. Depending on the type of irradiation and the beam delivery technique (pulsed beam/pulsed-scanned beam/continuous beam), the contribution of initial and general recombination to the total recombination effect varies,

which results in different dependencies on the applied voltage and thus the requirement of different methods for the determination of k_s [IAEA, 2000]. In order to be independent of the different recombination processes taking place in synchrotron-based carbon ion radiation, the formalism described in DIN [2016] will be used within this thesis for the determination of k_s. Therefore, the voltage, U, applied to the ionization chamber has to be varied within the maximal limits as given by the manufacturer with the dosimeter reading (for the same applied dose) determined as a function of U. In order to generate a so-called Jaffé-diagram, the reciprocal mean of the values determined at positive and negative voltage are plotted with respect to $1/U$. At least four data points are necessary in order to apply the following linear-quadratic fit function and accurately determine the corresponding fit parameters a_0, a_1, and a_2:

$$Y = a_0 + a_1 \cdot \frac{1}{U} + a_2 \cdot \left(\frac{1}{U^2}\right)^2 . \tag{4.10}$$

k_s is then given as the ratio of $Y(U_G)$, with U_G being the user voltage, and Y at the position $1/U = 0$:

$$k_{s,Q} = \frac{a_0 + a_1 \cdot \frac{1}{U_G} + a_2 \cdot \left(\frac{1}{U_G^2}\right)^2}{a_0} = 1 + \frac{a_1}{a_0} \cdot \left(\frac{1}{U_G}\right) + \frac{a_2}{a_0} \cdot \left(\frac{1}{U_G}\right)^2 . \tag{4.11}$$

If the $N_{D,w}$ calibration factor for ^{60}Co radiation is influenced by the saturation effect under reference conditions, a modified k_s has to be applied:

$$k_s = \frac{k_{s,Q}}{k_{s,Co}} . \tag{4.12}$$

4.2.2.4 Volume effect k_V

As ionization chambers have a finite volume, the measured value is always an averaged value over the sensitive volume of the ionization chamber. Thus, especially in regions with high dose gradients, an exact measurement of absorbed dose to water would require an ideal, point-like detector. In conventional radiation therapy, this so-called volume effect has drawn more and more attention in the last years as modern beam delivery techniques like intensity modulated radiation therapy (IMRT) and stereotactic radiosurgery use small irradiation fields exhibiting steep dose gradients in order to achieve an optimal dose conformity to the target volume. Thus, special codes of practice for the dosimetry of such small and non-standard fields have been developed ([Alfonso et al., 2008], [DIN, 2014]) handling the finite size of 'real' detectors by introducing an additional volume effect correction factor k_V [Looe et al., 2014]. As the signal of an ionization chamber is proportional to the integral of the dose values for all points of the detection region weighted with the spatial dose response function, $K(x)$, of the individual chamber, extensive work is recently carried out to measure $K(x)$ for commonly used ionization chambers with respect to photon beams (*e.g.* [Ketelhut and Kapsch, 2015], [Butler et al., 2015] and references therein).
However, this concept has not yet been transferred from the dosimetry of photon beams to the dosimetry of ion beams, although especially irradiation fields delivered by scanned ion beams show intrinsic inhomogeneities with partly significant dose gradients. As spatial dose response functions of ionization chambers with respect to carbon ion beams do not exist yet, simplified assumptions have been made within this thesis in order to account for the volume

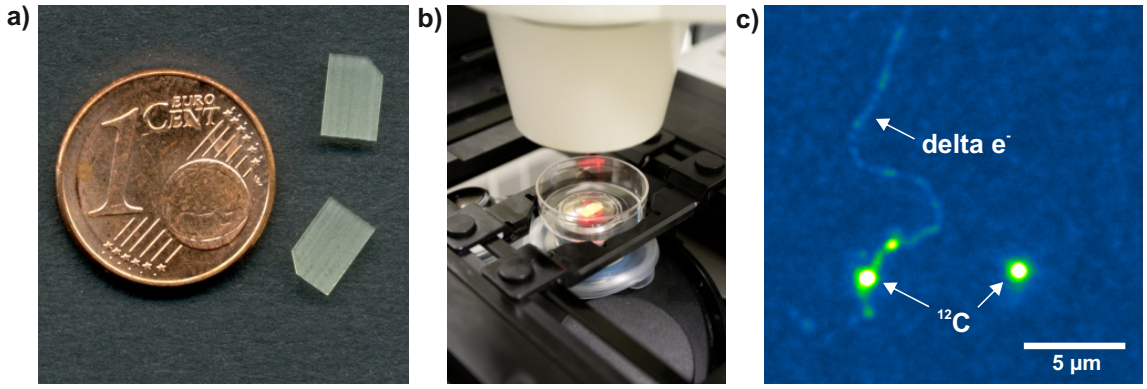

Fig. 4.5: *a) FNTDs with dimensions* $(4 \times 6 \times 0.5)\,mm^3$ *compared in size to a one cent coin. b) FNTD mounted on the microscope stage in a glass bottom microwell dish for detector readout using DKFZ´s Zeiss LSM 710 ConfoCor 3. c) Exemplary image of an FNTD irradiated perpendicular with 221 MeV/u carbon ions. Besides the tracks of two primary particles, the trajectory of a generated delta electron is clearly visible. All images are reprinted from Osinga [2012].*

effect and refer the measured integral signal of the ionization chamber to a reference point of the irradiated field, which will be explained in detail in Sec. 6.5.1.3.

4.3 Al_2O_3:C,Mg-based fluorescent nuclear track detector

4.3.1 Detector design and principle of operation

Al_2O_3:C,Mg-based fluorescent nuclear track detectors (FNTDs) (Fig. 4.5 a) developed by the Crystal Growth Division of Landauer Inc., Stillwater/OK contain aggregate F_2^{2+}(2Mg) color centers exhibiting radiochromatic transformations under ionizing radiation. These transformed F_2^{+}(2Mg) centers produce high yield intra-center fluorescence at 750 ± 50 nm when stimulated at 620 ± 50 nm with a short lifetime of 75 ± 5 ns. As the transformed color centers are optically, thermally, and temporally stable, non-destructive optical imaging of energy deposition and hence charged particle tracks is enabled [Akselrod et al., 2003]. Thus, by means of a confocal laser scanning microscope (Fig. 4.5 b), FNTDs allow the detection and visualization of individual charged particle tracks (Fig. 4.5 c) through the volume of the detector with sub-µm resolution and full three dimensional information. More detailed information on FNTD technology and its various applications can be found in Akselrod and Sykora [2011] as well as references therein.

4.3.2 Detector readout

Within this thesis, the inverted confocal laser scanning microscope LSM 710 ConfoCor 3 (Zeiss, Oberkochen) equipped with a z-piezo stage was used for detector readout, which has been provided by the light microscopy facility at DKFZ. A detailed description of the microscope and the sample handling can be found in Osinga [2012] and Greilich et al. [2013], while the individual microscope control parameters used for image acquisition with respect to single particle detection are described in Osinga et al. [2013]. Briefly, a Helium-Neon laser (633 nm, 5 mW) has been used for excitation with a main dichroic beam split-

ter 488/561/633 nm applied to separate the fluorescence signal (750 nm) from the excitation light. Additionally, a long-pass emission filter (>655 nm) was used for detection. As avalanche photodiodes (APDs) surpass photomultiplier tubes (PMTs) regarding their quantum efficiency especially in the long wavelength range around 750 nm being typical for FNTD fluorescence, an APD has been used in single photon counting mode to detect the FNTD signal. In order to gain the best resolution, a 63× magnification objective lens with a numerical aperture of 1.45 combined with low-autofluorescent Zeiss Immersion^{TM} 518F immersion medium was used allowing for a lateral (axial) resolution of about 200 nm (800 nm). In case of FNTDs irradiated perpendicular to their surface as used for fluence determination, the stochastic nature of energy deposition (*cf* Sec. 2.3) causes variations in the particle track fluorescence intensity in depth (referred to as z-direction) being most pronounced for low-LET particles. In order to reduce the impact of this 'reduced intensity effect' on the FNTD´s particle detection efficiency, a series of images from the specimen at different depth z (referred to as 'z-stack') are acquired to generate a median intensity projection. As demonstrated in Osinga et al. [2013], this procedure has found to sufficiently mitigate adverse effects of reduced particle track intensities being beneficial in terms of single particle detection.

4.3.3 Fluence assessment

In order to determine the particle fluence Φ (*cf* Sec. 2.5), the acquired FNTD images were further processed using the open source Java program ImageJ [Rasband], [Abràmoff et al., 2004]. The 'Mosaic' background subtractor [Cardinale, 2010] and particle tracker [Sbalzarini and Koumoutsakos, 2005] plug-ins have been used in order to subtract the background of the FNTD microscope images and to automatically find the particle track positions needed for fluence assessment. Further data processing was done in R (version 2.14.2) [R Development Core Team, 2015]. Detailed information on the individual settings used for image post-processing and particle tracking can be found in Osinga [2012] and Osinga et al. [2013].
With respect to a primary heavy ion beam (*e.g.* ^{12}C), the definition of Φ as spatial differential quantity, $\Phi = \frac{dN}{dA_\perp}$, reduces to

$$\Phi = \frac{N}{A_\perp} \,, \tag{4.13}$$

as scattering effects can be neglected in this specific case (*cf* Sec. 2.6). However, for ions traversing the FNTD under a polar angle $\vartheta \neq 0°$ due to e.g. non-perpendicular irradiation or misalignment of the FNTD under the microscope, the analyzed area A does not coincide with the planar area $A_\perp$. Thus, for an accurate determination of the particle fluence, this effect needs to be accounted for by multiplying A with a correction factor, k_A, according to

$$A_\perp = A \cdot k_A = cos\vartheta \cdot A \,, \tag{4.14}$$

with ϑ derived from the three dimensional information on the particle trajectory obtained within the FNTD by means of confocal laser scanning microscopy [Osinga et al., 2014b]. Since FNTDs have shown a track detection efficiency of $\geq 99.83\,\%$ [Osinga et al., 2013] and uncertainties of A have been proven to be negligible, the standard measurement uncertainty of the particle fluence is dominated by Poisson counting statistics:

$$\frac{\Delta\Phi}{\Phi} = \frac{1}{\sqrt{N}} = \frac{1}{\sqrt{\Phi \cdot A_\perp}} \,. \tag{4.15}$$

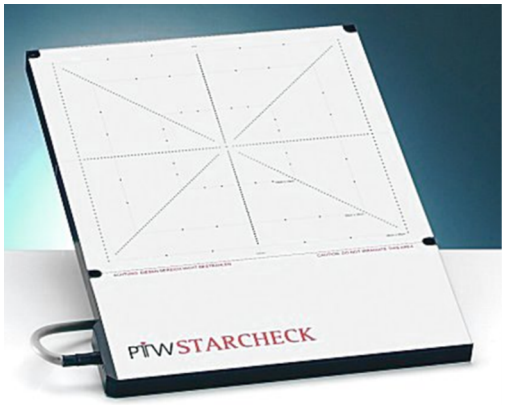

Fig. 4.6: *Two-dimensional ionization chamber array* STARCHECK *by PTW (Freiburg, Germany). Image reprinted from [PTW, 2013b].*

4.4 Detectors used for ion beam characterization

4.4.1 Ionization chamber array STARCHECK®

The two-dimensional ionization chamber array STARCHECK (T10043) with the detector interface 4000 (T16039) and corresponding BEAMADJUST software (Version 1.5.1.0) by PTW (Freiburg, Germany) was used within this thesis for the measurement of relative lateral dose profiles. STARCHECK consists of 527 air-filled ionization chambers with a sensitive volume of each 0.053 cm^3 (dimensions: 8 mm$\times$3 mm$\times$ 2.2 mm) covering an area of 27 cm$\times$ 27 cm. The ionization chambers are arranged star-shaped allowing a maximal spatial resolution of 3 mm along the principal axes and diagonals as illustrated in Fig. 4.6. The detector array is calibrated by the manufacturer in ^{60}Co radiation correcting the response of each ionization chamber relative to the response of the central chamber with an uncertainty of $\pm$1 % [PTW, 2013b]. All further data processing has been done by R (Version 2.15.2) [R Development Core Team, 2015].

4.4.2 Multi-wire proportional chamber

The type of multi-wire proportional chamber (MWPC) used within this thesis has been developed by SIEMENS AG based on the original design from the '*Gesellschaft für Schwerionenforschung*' (GSI) in Darmstadt, Germany [Haberer et al., 1993], [Kraft and Weber 2011]. The following description is based on information from the manufacturer as well as the publications by [Parodi et al., 2012] and [Ringbæk et al., 2015]. The chamber is designed as a plane-parallel transmission ionization chamber with an array of electrodes realized by tungsten wires. The signal wires (∅: 50 µm) are arranged in two levels rotated by 90 ° allowing a spatial resolution in x and y direction as schematically shown in Fig. 4.7. As in other ionization chamber designs, charge carriers, which are generated within the active volume of the MWPC by the traversing ion beam, will drift to the surrounding electrodes resulting in an electronic signal. As the density and spatial distribution of the generated charge carriers represent the profile of the beam, the integrated charge distribution measured with the read-out wires in x and y direction corresponds to an one-dimensional projection of the beam´s particle density. Typically, the signal is sampled with a frequency of a few kHz. Although adjacent wires have a distance of 1 mm, the spatial resolution of the detected signal is reduced by a factor of two, as two wires are always interconnected to one detection channel in order to increase the read-out signal. As a result, the (I) position of the beam in x and

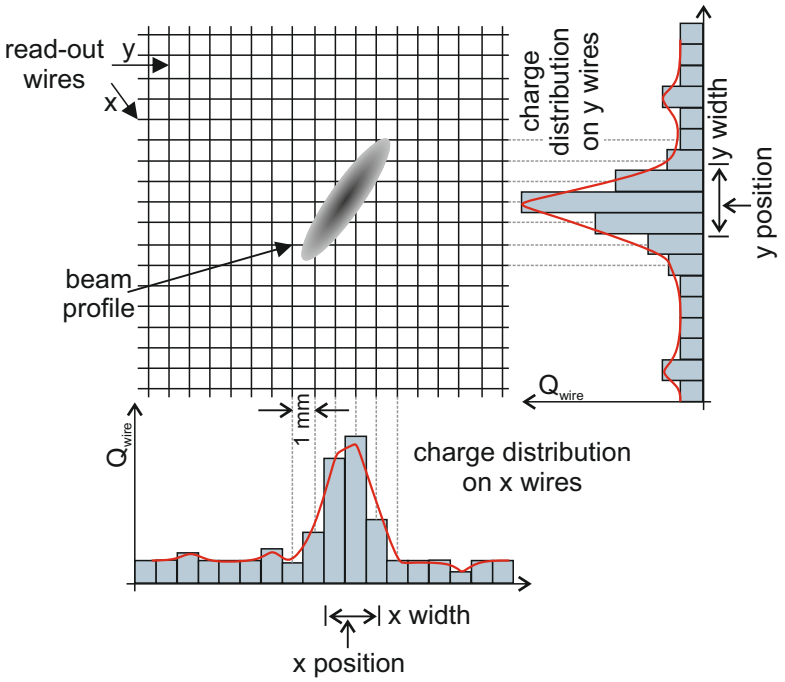

Fig. 4.7: *Simplified illustration of the multi-wire proportional chamber designed by SIEMENS AG, which covers an detection area of more than $20 \times 20\,cm^2$. The signal wires are located on an 1 mm grid with a positioning uncertainty of max. $\pm$ 0.1 mm [personal communication Dr. Stephan Brons, medical physicist at HIT]. For better illustration, the high-voltage tungsten wires (∅: 20 µm, separation of 2 mm) oriented at 45 ° with respect to the signal wires are not included in the graph. Reproduction according to the detector manual from SIEMENS AG.*

y direction is given by the charge-weighted mean of all detection channels having a signal over a certain threshold value, and the (II) full width at half maximum (FWHM) of the projected beam is calculated using the charge-weighted standard deviation of the contributing detection signals.

4.4.3 PEAKFINDER water column

The PEAKFINDER water column by PTW (Freiburg, Germany) allows to measure depth dose curves in proton and heavy ion beams with a spatial resolution of 10 µm and was used within this thesis for the experimental determination of material-specific WEPL-values according to the procedure described in Sec. 2.4. As shown in Fig. 4.8, the PEAKFINDER consists of one measuring detector and one reference detector separated by a water containing bellow alterable in length. As a measuring detector a thin-window Bragg peak chamber (type 34080, 41 mm radius of sensitive volume) is used, which is placed free in air between the bellows, while the reference chamber (type 34082, 29 mm radius of sensitive volume) is fixed at the entrance side. The measuring detector can be positioned with an absolute accuracy of 100 µm in increments as small as 10 µm synchronized with the spill structure of the synchrotron (setting Spill Start/Stop within the included PTW PeakScan software). Within this thesis, both chambers were operated at 400 V with the signals read out by a TANDEM XDR dual channel electrometer by PTW (Freiburg, Germany). The water-equivalent thicknesses (WET) of the different PEAKFINDER elements contributing to the total WET of the PEAKFINDER measurements are given in Tab. 4.3 [PTW, 2015].

4.4.4 Radiographic films

The radiographic KODAK EDR2 (Extended Dose Range) film (Carestream Health Inc., Rochester, NY, USA) has been used within this thesis to determine the focus size of single carbon ion pencil beams by analyzing the corresponding relative dose profiles. As the

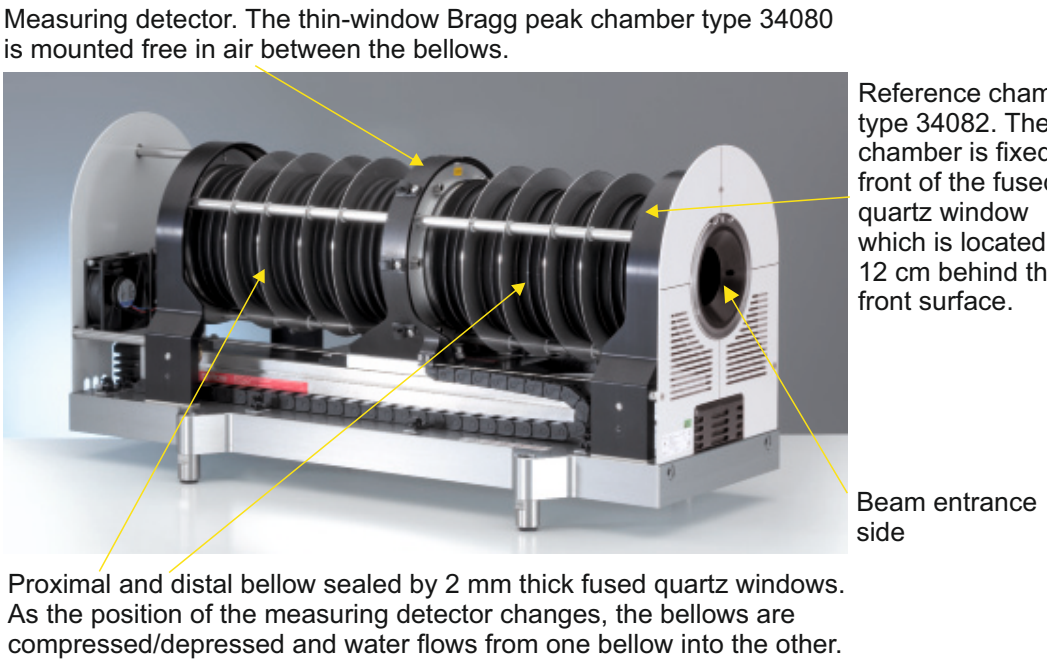

Fig. 4.8: *The picture shows the* PEAKFINDER *without cover explaining the function of the most important parts. Image reproduced according to [PTW, 2015].*

manufacturer states an applicability of the films within a dose range of 25 - 400 cGy with an approximate saturation dose of 700 cGy, EDR2 films are routinely used for this application within the quality assurance measurements performed at HIT. Following the HIT protocol, the films have been chemically processed directly after irradiation using the developing machine CURIX60 of Agfa-Gevaert Group with the corresponding developer (G 153, A) and fixer (G 354) components. Afterwards, the films were scanned using the Vidar Dosimetry Pro Advantage (Red) scanner, which is a medical film digitizer developed by Vidar Systems Corporation (Herndon, VA, USA) in cooperation with International Specialty Products for the use with EBT films. For scanning, the MEPHISTO mc^2 film scan software by PTW (Freiburg, Germany) has been used with a resolution of 71 dpi corresponding to a pixel size of about 0.32 mm and a color depth of 16 bit. The geometric accuracy of the scanner is specified as better than 1 % or 2 pixels (whichever is larger) by the manufacturer [VIDAR]. Further film processing and data analysis has been done by ImageJ ([Abràmoff et al., 2004], [Rasband]) and R (Version 2.15.2) [R Development Core Team, 2015].

4.5 Beam delivery at the Heidelberg Ion-Beam Therapy Center

The Heidelberg Ion-Beam Therapy Center (HIT) is a university-hospital-based dedicated particle-therapy center being in clinical operation since November 2009 [Combs et al., 2010]. Based on the technical developments at GSI, the HIT facility fully relies on an active beam delivery method, the so-called intensity-controlled rasterscan technique [Haberer et al., 1993]. This technique allows to precisely scan a focused particle beam by means of vertical and horizontal magnets over the radiation volume. Therefore, the volume is divided into numerous slices in depth, with each slice subdivided into a raster of voxel points. By actively adapting

Element	WET / mm
Air gap between PEAKFINDER surface and outer surface of the reference chamber	0.12 ± 0.01
Reference chamber	1.91 ± 0.02
Both quartz windows sealing the first water containing bellow	11.06 ± 0.05
Smallest possible water column between reference and measuring chamber	3.63 ± 0.02
Distance between outer surface of measuring chamber and reference point	0.70 ± 0.10
Total off-set	$\mathbf{17.42 \pm 0.12}$

Table 4.3: *Water-equivalent thicknesses (WET) of the different* PEAKFINDER *elements contributing to the total WET of the measurements performed with the 'HIT Peakfinder'. The given values are adopted from the measured WET routinely used at HIT [Dr. Peter Heeg, medical physicist at HIT, personal communication].*

the energy of the particle beam, one slice after the other is irradiated allowing an optimal target coverage. A linac-synchrotron combination enables the delivery of a combination of 255 energies corresponding to ranges in water of 2 cm to 30 cm, 6 pencil beam foci, and 15 intensity values for each of the different ion species ranging from proton to oxygen. Concerning the available foci widths, a gaussian distribution is assumed for both horizontal and vertical beam profiles with FWHM values ranging from 4 - 20 mm in air with respect to the isocenter. Intensities between 2e6 and 5e8 ions/s can be chosen for carbon ions, while the available intensities are increased *e.g.* by a factor of 40 for protons in order to account for their lower stopping-power and reduced RBE [Parodi et al., 2012]. Due to the synchrotron-based beam delivery, the irradiation has a pulsed structure with beam-on times of about 5 s and beam-off times, where new particles are accelerated to the requested energy, of about 4.5 s. Besides three treatment rooms (2 horizontal beamlines and 1 gantry), an additional room equipped with the equivalent beam scanning technique is available, which is dedicated to quality assurance (QA) and pre-clinical research and has therefore been used for all measurements performed within this thesis. In the following, this room will be referred to as 'QA-room'.

In order to control the beam delivery, the beam application monitoring system (BAMS) developed by SIEMENS AG is used at HIT, which is based on the original design from GSI [Haberer et al., 1993], [Kraft and Weber, 2011]. Fig. 4.9 shows a schematic drawing of the BAMS located in the beam nozzle of each irradiation room. It basically consists of a redundant system of 3 identical ionization chambers (ICs), which are framed by 2 multi-wire proportional chambers (MWPCs) (Sec. 4.4.2) [Parodi et al., 2012]. The first MWPC passed by the beam regulates the position of the beam in horizontal and vertical direction, while the first IC regulates the number of particles delivered per irradiation spot. For quality assurance purposes, the time-resolved measurements of the MWPCs as well as the ICs containing all the irradiation-relevant information like position, irradiation duration, beam width in x and y, and number of delivered particles per spot are recorded for each irradiation within the so-called machine beam records.

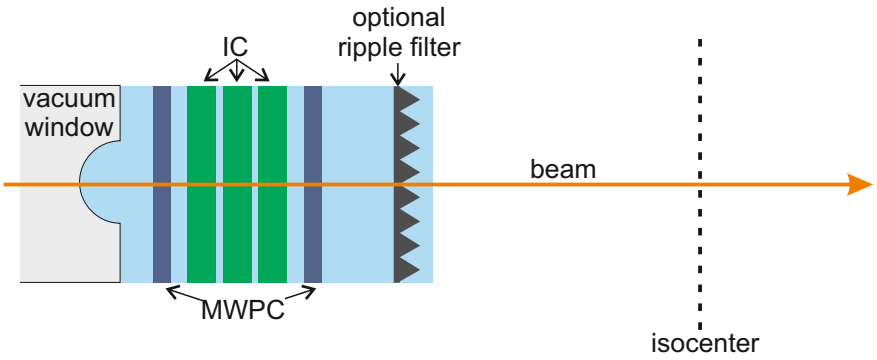

Fig. 4.9: *Schematic illustration of the beam delivery monitoring system (BAMS) used at HIT and the position of the optional ripple filter. Reproduction according to Parodi et al. [2012].*

4.6 Monte Carlo particle transport simulations

For the performance of Monte Carlo (MC) particle transport simulations of carbon ion beams, the MC code FLUKA [Böhlen et al., 2014; Ferrari et al., 2005] has been chosen being used since 2006 for multiple applications in the preparation of the clinical operation of proton and carbon ion therapy at HIT [Parodi et al., 2012]. Within this thesis, MC simulations were performed to (I) obtain laterally integrated depth dose distributions, to (II) estimate the dose deposited by primary particles and fragments in actual irradiation conditions, and to (III) determine the LET distribution of the particle spectrum at the actual measurement position.

For all simulations, the recommended default settings for hadrontherapy, HADROTHE, were used ensuring detailed transport of primary and secondary particles including accurate treatment of multiple Coulomb scattering of charged particles. Except for some specific applications where changes are explicitly stated in the text, the HADROTHE default threshold of 100 keV kinetic energy for hadron transport (except for neutrons, which are explicitly transported down to a threshold of 1e-5 eV) was used. Below this threshold value, particles are ranged to rest in one step with uniform energy deposition. Further, the particle transport step size of charged hadrons is restricted by default to a corresponding 5 % loss of kinetic energy, explicit δ-ray production is considered above a threshold of 100 keV, and transport of electrons, positrons and photons is activated (*cf* defaults HADROTHE in FLUKA manual). In addition to these defaults, full transport of light and heavy ions was activated with the IONTRANS card and the evaporation of heavy fragments considered by using the 'new evaporation model' within the PHYSICS card to accurately describe residual nuclei and fragment production in ion beams. To build the executable FLUKA file, the DPMJET-III and RQMD libraries were used.

Chapter 5

Comparison of Ionization- and Fluence-based Dosimetry

This chapter deals with the direct comparison of fluence-based dosimetry by means of FNTDs and ionization-based dosimetry using a thimble ionization chamber performed in the clinical carbon ion beam at HIT within the first part of this thesis. As this work has already been published in Osinga et al. [2014b], the content of this chapter adheres closely to the named publication.

5.1 Experimental set-up and irradiations

For the direct comparison of ionization- and fluence-based dosimetry, the Farmer-type ionization chamber TM30013 S/N 1714 by PTW, Freiburg (specifications are given in Tab. 4.1 and Tab. 4.2) and Al_2O_3:C,Mg-based FNTDs (*cf* Sec. 4.3) of dimension $4 \times 8 \times 0.5\,mm^3$ were used. All irradiation have been performed in the QA-room at HIT (*cf* Sec. 4.5) with 270.55 MeV/u carbon ions. In order to allow for optimal measurement conditions of the FNTD and ensure a fair comparison of both methods, the following aspects have been considered in the choice of irradiation parameters:

- Although it has been shown that the fluorescence amplitude of the particle tracks on the FNTD is related to the LET of the particles enabling particle discrimination on a wide range of LET [Sykora et al., 2008a], the performance of FNTDs for particle spectroscopy in clinical applications with the read-out protocol used within this study has still to be specified in more detail [Niklas et al., 2013]. Thus, all irradiations have been performed in the entrance channel of the ion beam without ripple filter in order to keep the percentage of fragments as well as the effect of energy straggling on the initial monoenergetic carbon ion beam as small as possible (*cf* Sec. 2.7 and Sec. 2.3). Further, scattering effects of the primary carbon ions are especially small in the entrance channel (*cf* Sec. 2.6) enabling the determination of the particle fluence by means of a simplified, non-differential equation as discussed in Sec. 4.3.3.

- In addition, an initial particle fluence of $3 \times 10^6\,cm^{-2}$ has been chosen lying within the optimal working range of FNTDs [Osinga et al., 2013], [Osinga et al., 2014a]. At the same time, the delivered dose corresponding to this particle fluence is still high enough to enable accurate ionization-based dosimetry.

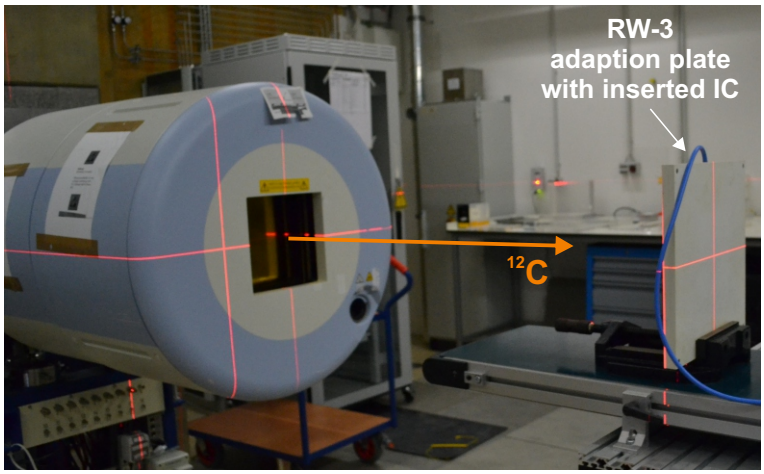

Fig. 5.2: *Experimental set-up used for the direct comparison of fluence-based dosimetry by means of FNTDs and ionization-based dosimetry using the Farmer-type ionization chamber TM30013. For the measurements, the RW-3 adaption plate containing the ionization chamber/FNTD, respectively, was positioned in the isocenter in the QA-room at HIT.*

- Because the detection area of the FNTD does not coincide with the sensitive volume of the ionization chamber (IC) as schematically shown in Fig. 5.1, an irradiation field of 10 cm × 10 cm has been chosen to achieve a preferably homogenous dose distribution in the center of the field where the measurements were performed.

For the measurements, the ionization chamber was placed in a 30 cm × 30 cm water-equivalent RW-3 adaption plate (PTW, Freiburg, Germany) with 7 mm RW-3 in front and 13 mm RW-3 as backscatter material as shown in Fig. 5.2. According to the manufacturers' instructions, a fixed positive bias potential of + 400 V has been applied to the chamber thimble with the background-corrected integral signal of the ionization chamber reading measured by means of a UNIDOS electrometer (PTW, Freiburg). The absorbed dose to water was determined according to TRS-398 [IAEA, 2000] using the chamber-specific k_Q-factor of 1.032 as discussed in Sec. 3.1. Polarization and saturation effects were assumed to be unity with the correction for air temperature and pressure applied before the first measurement (*cf* Sec. 4.2.2).
In order to ensure comparable measurement conditions, the same experimental set-up as used for the ionization chamber has been used for the FNTD with the only exception of using 4.7 mm instead of 7.0 mm RW-3 in front of the detector taking into account the effective point of measurement of the cylindrical ionization chamber as discussed in chapter 3 and schematically illustrated in Fig. 3.1.
In total, four measurements have been performed with FNTDs and 18 measurements with the ionization chamber.

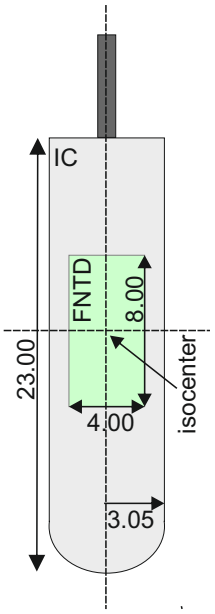

Fig. 5.1: *Comparison in size of FNTD and IC. Dimensions are given in mm.*

5.2 FNTD read-out and fluence-based dose approximation

According to the procedure described in Sec. 4.3.2, all FNTDs were read-out starting 20 µm below the detector surface acquiring a 'z-stack' of five images separated by $\Delta z = 5$ µm covering an area of 1.02 mm^2. The information in depth was used for two purposes, namely (I) the determination of the polar angle ϑ accounting for a possible non-perpendicular irradiation

or misalignment of the FNTD under the microscope needed for the correct calculation of the planar area $A_{\perp}$ according to Eq. 4.14 and (II) the generation of a median intensity projection in order to minimize the influence of the 'reduced intensity effect' on the particle detection efficiency as explained in Sec. 4.3.2. All tracked particles were discriminated concerning the relative fluorescence amplitude of their tracks into primary carbon ions and secondary lighter fragments in general as exemplary shown in the insert of Fig. 5.3. For all four FNTDs, ϑ of the primary carbon ions was found to be very small ($< 1°$) resulting in an almost negligible correction factor k_A used for the determination of the primary carbon ion fluence, $\Phi_{^{12}C,prim}$, according to Eq. 4.13. As the measurements have been performed in the entrance channel of the ion beam, the contribution of fragments to the total absorbed dose is assumed to be negligible. Thus, only Φ_{prim} as determined by means of FNTDs has been considered for the calculation of absorbed dose to water using the approach described in Sec. 2.5 by multiplying the primary particle fluence with the corresponding mass stopping-power of water taken from ICRU [2005]. Therefore, the particle energy at the detector surface, E_{prim}, has been calculated using the continuous slowing down approximation (CSDA) by the 'libamtrack' library [Greilich et al., 2010] considering a nominal energy of 270.55 MeV/u and a total WET of 7.71 mm. This WET consists of 2.89 mm comprising all traversed materials between the high-energy beam line and the isocenter in the QA-room at HIT as well as 4.82 mm being the WET of 4.7 mm RW-3 using the corresponding WEPL of 1.025 ± 0.011 [Jäkel et al., 2001] (*cf* Sec. 2.4).

5.3 MC simulation of the particle energy and spectrum

In order to verify the assumption of a monoenergetic primary carbon ion beam as well as the negligence of fragments contributing to the overall absorbed dose to water at the actual measurement position, MC transport simulations were performed [Dr. Steffen Greilich, DKFZ, personal communication]. Therefore, the FLUKA code version 2011 vs.17 (*cf* Sec. 4.6) has been used to estimate the dose deposited by primary carbon ions and fragments at the actual measurement position as well as to determine the particle fluence of both primary and secondary particles as a function of energy. The absorbed dose to water deposited at the measurement position of the FNTD was estimated using FLUKA's USRBIN scorer in a water volume of 1 cm$\times$1 cm$\times$0.003 cm behind 7.7 mm of water (*cf* previous section) using the MC settings explained in Sec. 4.6. With respect to the particle spectrum (fluence versus energy), FLUKA's USRTRACK estimator with linear energy binning was used in combination with the user routine FLUSCW allowing for particle discrimination. In order to calculate the absorbed dose to water resulting from this particle spectrum, the corresponding particle LET was evaluated at the center of each energy bin using LET values in liquid water from ICRU [1993] and ICRU [2005] by the 'libamtrack' library [Greilich et al., 2010]. Further, additional simulations were done where the water surrounding the target volume was replaced by RW-3 of corresponding thickness and the target volume by Al_2O_3, respectively, in order to investigate any significant influence of the phantom and the detector material.

5.4 Irradiation field homogeneity

While no direct measurements were performed to investigate the lateral dose distribution of the irradiation field used for the comparison of ionization- and fluence-based dosime-

Quantity	H / %	He /%	Li / %	Be / %	B / %	C / %	
						Low E	High E
Fluence	14.8	2.4	0.3	0.2	0.4	0.1	81.8
Dose	1.7	0.6	0.1	0.1	0.3	0.2	97.1

Table 5.1: *MC transport simulation results on relative fluences and doses for a water volume at 7.7 mm WET for 270.55 MeV/u carbon ions.*

try, cross sections of the irradiated FNTDs in horizontal (4.00 mm × 0.14 mm) and vertical (0.14 mm × 8.00 mm) direction were acquired in order to approximate the spatial fluence distribution. However, as the detection area of the FNTD and especially the analyzed cross-sections do by far not cover the sensitive area of the ionization chamber (*cf* Fig. 5.1), additional information on the irradiation field homogeneity were derived retrospectively from the beam application monitoring system (BAMS). As explained in Sec. 4.5, all irradiation-relevant information like pencil beam position, beam width in x and y, irradiation duration, as well as number of delivered particles per spot are recorded for each irradiation within the so-called machine beam records acquired by the time-resolved measurements of the multi-wire proportional chambers (MWPCs) as well as ionization chambers (ICs) located in the beam nozzle. Internally, the information of the machine beam records, which refer to the measurement position within the beam nozzle, are transferred to the isocenter via a linear relation and stored in the so-called physical beam records. Thus, by using the spatial irradiation pattern of the physical beam records as well as the number of particles delivered to each raster spot, the resulting two-dimensional dose distribution has been calculated by superimposing single carbon ion pencil beams. This data was analyzed for all performed irradiations regarding deviations from the nominal particle fluence in order to estimate the homogeneity of the entire irradiation field with respect to the isocentric measurement position.

5.5 Results

The mean dose value based on Φ_{prim} of 61.45 mGy ± 0.7 % as determined by means of FNTDs (Fig. 5.3, blue line) was found to be 7.4 % lower than the ionization-based value of 66.35 mGy ± 0.4 % (green line) assuming a monoenergetic carbon ion beam of E_{prim}(CSDA) = 261.88 MeV/u corresponding to $S_{CSDA} = 13.64$ keV/µm by a continuous slowing down approximation. The performed MC transport simulations summarized in Tab. 5.1 have shown that this assumption is true for $\Phi_{prim}(E_{prim}) = 81.8$ % of the detected carbon ions, while only $\Phi_{prim}(E < E_{prim}) = 0.1$ % exhibit a lower energy having a small contribution of 0.2 % to the total deposited dose. However, even in the entrance channel of the carbon ion beam, the MC transport simulation showed that the contribution of fragments to the total absorbed dose is not, as assumed, negligible. According to the simulation, primary carbon ions account for 97.1 % of the total deposited dose, while protons (helium) with a relative fluence of 14.8 % (2.4 %) contribute 1.7 % (0.6 %). The influence of heavier fragments has shown to be negligible. Thus, by taking the contribution of fragments into account as well as considering the small energy distribution of the carbon ions by means of an effective stopping-power, the discrepancy between fluence- and ionization-based dose determination reduces by 2.9 pp (percentage points) leaving 4.5 % (Fig. 5.3, red line).

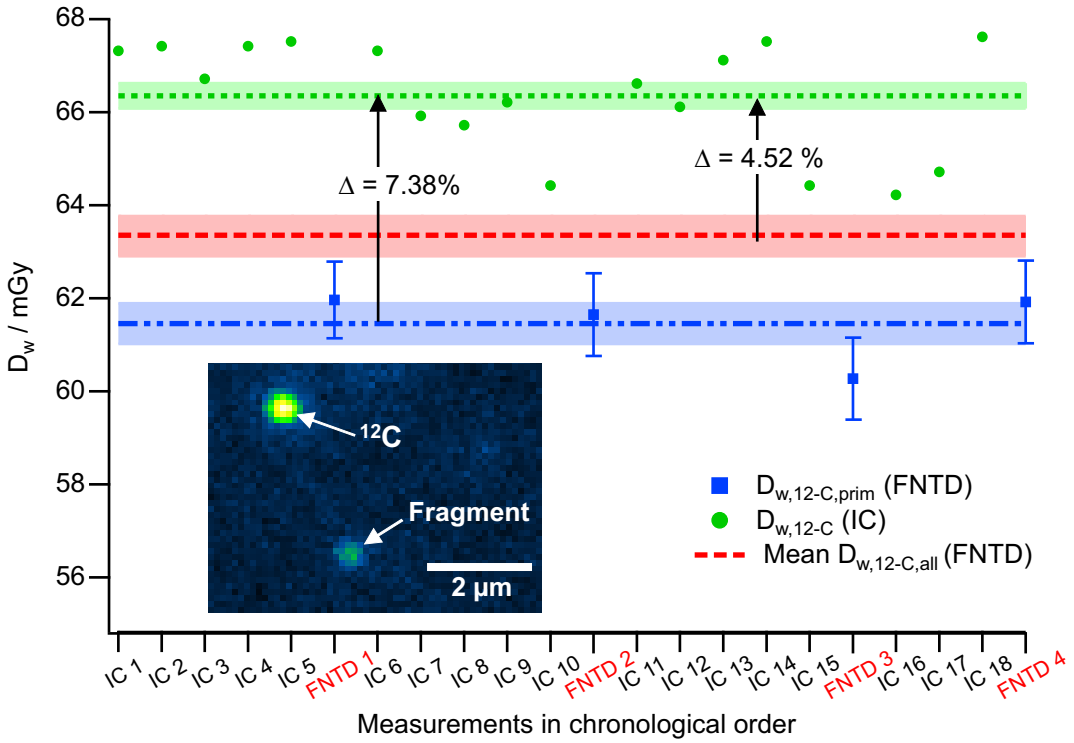

Fig. 5.3: *Result of the direct comparison between fluence-based dosimetry using FNTDs and ionization-based dosimetry using the thimble ionization chamber TM30013 in the clinical carbon ion beam at HIT revealing a discrepancy of 4.52 %. Here, the contribution of fragments to the total deposited dose as shown by MC transport simulations has been taken into account. The insert shows a corresponding FNTD microscope image emphasizing the possibility to discriminate particle tracks from primary carbon ions and secondary particles in general due to their very different fluorescence intensity. Modified reprinted from Osinga et al. [2014b].*

Further, the simulations have shown that the influence of the RW-3 phantom on absorbed dose to water as determined at the measurement position of the FNTD/IC is negligible. In addition, the Al_2O_3 of the FNTD did not change the particle spectrum noticeably within the 20 µm in front of the readout depth and can thus not explain the discrepancy seen.
According to the procedure described in Sec. 5.4, forward calculations of the physical beam records have shown that the uniformity of the irradiation fields was within $\pm 0.8\,\%$ for all performed irradiations as exemplary shown in Fig. 5.4. Although this information is based on a retrospectively performed calculation and not on a 'real' measurement of the relative lateral dose distribution, it seems reasonable to assume from this result that dose inhomogeneities do not explain the observed discrepancy. In addition, no significant measured fluence gradients were found over the length and width of the FNTDs.

5.6 Discussion

By means of MC particle transport simulations it has been shown that, even in the entrance channel of a high-energy carbon ion beam, the contribution of fragments to the total absorbed dose is not negligible. However, also when considering the complete particle spectrum derived by the simulation in the fluence-based dose approximation by means of FNTDs, a

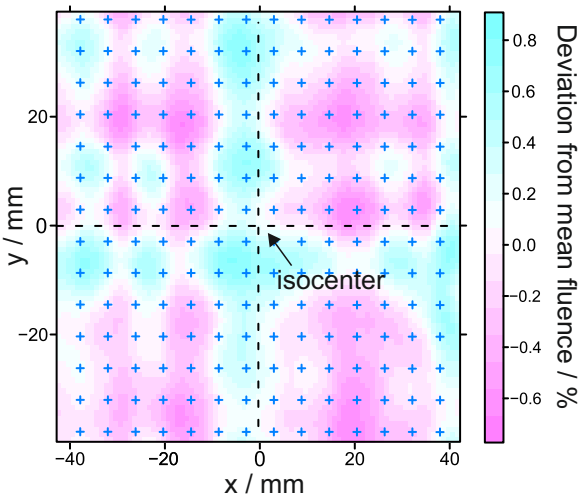

Fig. 5.4: *Deviations from the mean particle fluence as derived by the calculated two-dimensional dose distribution by means of the physical beam record as explained in Sec. 5.4.*

discrepancy of 4.5 % between fluence- and ionization-based dose determination remains. Considering the track detection efficiency of FNTD technology ($\geq$ 99.83 % [Osinga et al., 2013]), which covers the entire LET spectrum used in ion beam radiotherapy, and the ideal measurement conditions with respect to single particle detection, it seems unlikely that a significant portion of tracks were not registered by the FNTD, as would be necessary to explain the discrepancy. However, it is still puzzling that the relative secondary particle fluence of approximately $\Phi_{H,He,Li} = 3.3\,\%$ as detected by means of FNTDs shows a significant difference to the 17.5 % as predicted by the MC particle transport simulation. Using these values for dose assessment, the discrepancy would amount to 7.0 % instead of 4.5 %. As detailed information on the exact composition of the vacuum window and the beam monitoring system employed in the beam nozzle at HIT were not available for experimenters at the time of this comparison, a simplified model has been applied within the presented simulations by considering an additional WET of 2.89 mm. This includes all traversed materials between the high-energy beam line and the isocenter in the QA-room at HIT. Nowadays, so called 'phase-space files' are provided by HIT containing the full particle spectrum of primary and secondary particles of the nominal requested beam after the passage of the beam nozzle, therefore serving as a much more realistic starting point for the MC simulation of user-specific experimental set-ups [Tessonnier et al., 2016]. Thus, a direct comparison of both models might provide information about the puzzling abundance of fragments seen in the simulation. Another plausible explanation for the difference between simulated and detected secondary particle fluence are type B (systematic) uncertainties related to the applied MC code FLUKA, which have shown to be in the order of some tens of percent for differential quantities like the particle yield with respect to LET and energy [Böhlen et al., 2014].

When assuming negligible uncertainties from the experimental design like *e.g.* inhomogeneities in the lateral dose distribution, instabilities of the beam delivery system, as well as inaccuracies of the fluence determination by means of FNTDs, one might also question the accuracy of the calculated k_Q-factor for carbon ion beams currently used for clinical dosimetry by means of calibrated ionization chambers (*cf* Sec. 3.1). This re-opens the discussion by Hartmann et al. [1997] and others on the contested accuracy of the currently used constant W_{air}-value of 34.50 ± 0.52 eV (1.5 %), which dominates the total standard measurement uncertainty of the k_Q-factor (2.8 % with respect to thimble ionization chambers) [IAEA, 2000]. The findings presented in this chapter would rather suggest a W_{air}-value of 32.10 ± 0.83 eV

(2.6 %) with the given uncertainty including all conceivable sources of errors with respect to fluence assessment by means of FNTDs as well as ionization-based dosimetry according to TRS-398 (except for the uncertainties given for long-term stability of user dosimeter, establishment of reference conditions, dosimeter reading relative to beam monitor and beam quality correction). In order to investigate the contested accuracy of the currently used k_Q-factor for carbon ion beams in more detail, the second part of this thesis is devoted to absolute dose to water measurements in the clinical carbon ion beam at HIT by means of water calorimetry. This will allow to directly calibrate ionization chambers in units of absorbed dose to water and thus to experimentally determine the k_Q-factor for carbon ion beams.

As more conclusive results with respect to the findings of this chapter are expected from the water calorimetric measurements, a final conclusion will be given in chapter 7. In retrospect, besides the experimentally determined k_Q-factor for carbon ion beams, also the knowledge gained from the detailed investigation of the irradiation field used for water calorimetry is of major relevance for the evaluation of the measurements performed during the comparison of fluence-based and ionization-based dosimetry, which will be elaborated in detail in the concluding chapter.

Chapter 6

Experimental Determination of k_Q by means of Water Calorimetry

Three main calorimetric/ionometric beamtimes were performed within this thesis for the final determination of k_Q according to the calibration procedure described in Sec. 3.2. Each beamtime consisted of two consecutive night shifts for the calorimetric measurements and one additional night shift for the performance of corresponding ionometric measurements for the direct calibration of the ionization chambers in the carbon ion beam and thus the experimental determination of k_Q. All three beamtimes were performed within a time period of 7 months.
In Sec. 6.1, the experimental set-up of the water calorimeter at HIT will be described followed by Sec. 6.2 dealing with the selection of optimal irradiation parameters for the subsequent calorimetric measurements and a detailed presentation of the radiation field specifications given in Sec. 6.3. The measurement procedure and data analysis of the calorimetric measurements will be described in Sec. 6.4 including the determination of correction factors and their uncertainties. Analogue, corresponding ionometric measurements will be described in Sec. 6.5 with the resulting k_Q-factors presented in Sec. 6.6 and discussed in Sec. 6.7.

6.1 Set-up of the transportable PTB water calorimeter

The transportable PTB water calorimeter (*cf* Sec. 4.1) has been installed in the QA-room (*cf* Sec. 4.5) at HIT as shown in Fig. 6.1. Four earth anchors have been mounted to the floor of the QA-room with corresponding counterparts installed at the moveable equipment car of the water calorimeter ensuring reproducible measurement conditions. As a compromise, the water calorimeter had to be positioned well behind the isocenter (655 cm between isocenter and calorimeter surface) in order to enable other experimenters to perform irradiations in the isocenter while leaving the water calorimeter at its fixed position. This corresponds to a measurement position of the calorimetric detector at about 6.7 cm WET considering a nominal measurement depth of the thermistor probes of 50 mm with respect to the beam entrance window (*cf* Fig. 4.1 b). As all pre-defined beam parameters like focus size, spot position, *etc.* provided by HIT refer to the isocenter and are not valid at the measurement position of the calorimeter due to the beam divergence, similar beam characterization measurements had to be repeated for the measurement position of the calorimetric detector, which will be described in Sec. 6.3.

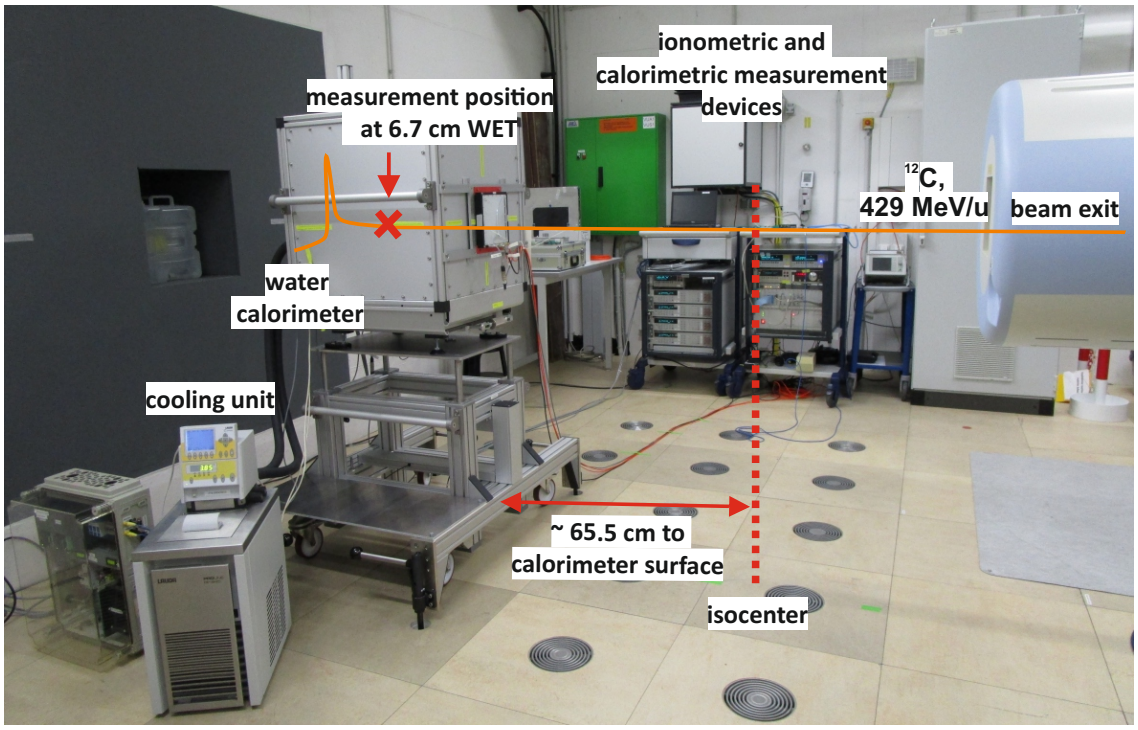

Fig. 6.1: *Experimental set-up of the transportable PTB water calorimeter in the QA-room at HIT. The electronic equipment for the calorimetric and ionometric measurements has been located well outside the beam path in order to not influence the read-out systems. Please note that the indicated Bragg curve is not true to scale.*

6.2 Selection of optimal irradiation parameters

Since the measurements with the water calorimeter at HIT are performed under special conditions, namely (I) the active beam delivery technique using intensity-controlled raster scanning and (II) the irradiation with a pulsed beam (*cf* Sec. 4.5), a number of aspects need to be considered when choosing irradiation parameters to allow for optimal irradiation conditions of the water calorimeter.

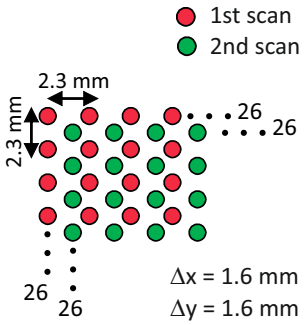

Fig. 6.2: *Schematic illustration of the spatial irradiation pattern. Line-wise horizontal scanning has been chosen in terms of beam delivery.*

Firstly, the irradiation time needs to be as short as possible in order to minimize heat conduction effects occurring during the calorimetric measurements. At the same time, the delivered dose needs to be well above 1 Gy in order to allow for an adequately large thermistor signal. However, it is not constructive to reduce the irradiation time by just limiting the field size. As shown by Krauss [2006a], radiation fields with a geometric width greater than 40 mm should be used to keep heat conduction effects small, which is necessary in order to achieve a low standard uncertainty in the later calorimetric measurements. In addition, the dose distribution needs to be homogenous and reproducible, as inhomogeneities of the lateral dose distribution have a strong effect for example on the corrections for heat conduction, k_c, the lateral measurement position, k_l, as well as the volume effect, k_V. With the expertise from the medical physicists at HIT, an irra-

Particle	^{12}C
Nominal energy	428.77 MeV/u (E254)
D_w	$\approx$ 1.5 Gy
Irradiation duration	$\approx$ 90 s (*cf* Tab. 6.4)
Intensity	8e7 ions/s (I10)
Measurement position	Entrance channel, WET: 6.7 cm (*cf* Sec. 6.1)
Focus size	$\approx$ 5.5 mm FWHM (F1) (*cf* Tab. 6.2)
Spatial irradiation pattern	see Fig. 6.2

Table 6.1: *Overview of the irradiation parameters used for the determination of k_Q. All irradiations were performed without ripple filter.*

diation plan has been generated allowing for an optimal trade-off between the aspects named before. As schematically shown in Fig. 6.2, a spatial irradiation pattern consisting of 26×26 spots deposited on a grid with 2.3 mm spacing in both x and y direction has been chosen in combination with a carbon ion pencil beam of about 5.5 mm FWHM (F1). Please note that already at this point the beam parameters and dimensions given refer to the measurement position of the water calorimeter and not to the isocenter, although the corresponding measurements for the off-isocentric beam characterization will not be described until Sec. 6.3.2. By irradiating the same raster pattern a second time but shifted by $\frac{1}{2} \cdot 2.3$ mm in both x and y direction, the effective distance between adjacent raster spots is reduced to 1.6 mm with a total irradiation field size of about 5.8 cm $\times$ 5.8 cm. As shown in Fig. 6.2, the resulting raster pattern is comparable to the close-packing of equal spheres commonly seen in crystal structures allowing to achieve the highest average density. This spatial raster pattern in combination with rescanning has been chosen as the resultant averaging effects are known to be beneficial in terms of homogeneity and reproducibility. The focus size F1 has been selected, as the corresponding carbon ion pencil beam shows the best symmetry and can be well approximated by a Gaussian distribution in both horizontal and vertical direction (*cf* Sec. 6.3.2.1). This is an important aspect with respect to the realistic mathematical reproduction of the beam parameters being essential input-values for the later performed heat conduction calculations. Further, as the dose is deposited sequentially spot by spot, the small spot size leads to temperature gradients which are orders of magnitude higher than in the case of photon fields. Since these temperature gradients appear only during the limited time interval when a given spot is not yet surrounded by other spots, an adequately high scanning speed compensates this effect and therefore minimizes corresponding heat conduction effects. Therefore, the highest clinically used (and therefore quality controlled) particle intensity of 8e7 ions per second (I10) was chosen. As strong temperature gradients in the vicinity of the Bragg peak inhibit the direct calorimetric determination of absorbed dose to water in that region [Krauss, 2006a], a measurement position in the flat entrance region of the Bragg curve has been chosen for the determination of k_Q. In order to allow for a large distance between calorimetric measurement position and Bragg peak, the second highest energy of 428.77 MeV/u (E254) available at HIT has been selected.

6.3 Radiation field specifications

In order to investigate the radiation field used for the determination of k_Q in detail, an experimental set-up was designed to mimic the real measurement conditions of the water calorime-

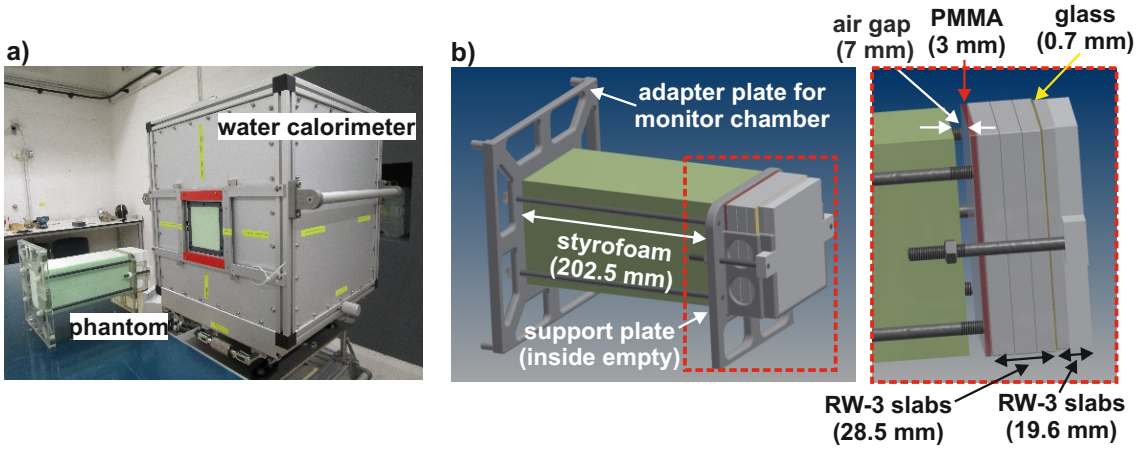

Fig. 6.3: *The figure shows the developed water-equivalent slab phantom mimicking the water calorimeter. In (a) the phantom is directly compared in size with the 'real' water calorimeter, while (b) schematically illustrates the exact composition of the phantom with all dimensions given as geometrical material thicknesses.*

ter by means of a water-equivalent slab phantom. In the following, the phantom design and its benefits regarding the radiation field characterization will be explained. Afterwards, the individual measurements performed to specify and monitor the radiation field over the course of the successively performed three calorimetric/ionometric beamtimes will be presented, which are of major importance for the later accurate determination of corresponding calorimetric and ionometric correction factors. In excess of the precise knowledge of the lateral and depth dose distribution needed for the determination of a series of correction factors (k_l, k_V, k_d, k_c), it is essential to precisely determine the spatial irradiation pattern, *i.e.* the position of each irradiated raster spot, the exact size and shape of the carbon ion pencil beam used, as well as the temporal irradiation structure, as these experimental information are required to precisely reproduce the real calorimetric measurement condition within the finite-element heat conduction calculations for the determination of k_c. Based upon these results, the determination of the correction factors will be described in Sec. 6.4.1 and Sec. 6.5.1. Further, MC simulations of the particle spectrum at the measurement position of the water calorimeter will be presented to additionally characterize the radiation field.

6.3.1 Development of a water-equivalent slab phantom

The following requirements were taken into account for the development of the phantom mimicking the measurement conditions of the water calorimeter:

- The material composition of the phantom had to be as close as possible to the materials used within the water calorimeter in order to ensure measurement conditions equal to the conditions used for the determination of k_Q. Only by doing so, the radiation field specifications determined using the phantom can be used to accurately determine the subsequent calorimetric and ionometric correction factors.

- While offering a high flexibility to be used for the variety of measurements necessary for field characterization, the set-up had to be easy to handle.

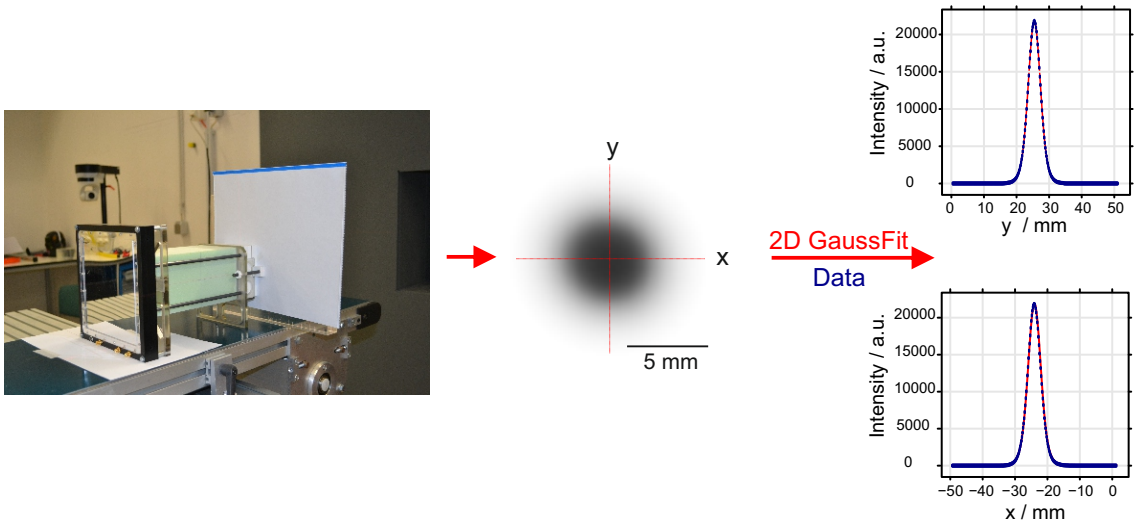

Fig. 6.4: *Experimental set-up for the determination of the focus size of the carbon ion pencil beam used for the determination of k_Q. Further, a processed EDR2 film showing the relative dose distribution of a single pencil beam is shown, which can be well approximated by a 2D Gaussian distribution.*

- In order to enable the combination of the phantom with all kinds of detectors (*e.g.* STARCHECK, PEAKFINDER, *etc.*), the design of the phantom had to ensure 'dry' conditions at the effective measurement position of the water calorimeter.

In order to fulfill these requirements, the phantom has been designed as a water-equivalent slab phantom consisting of the very same materials as the water calorimeter (*cf* Sec. 4.1.1) with the only exception of replacing liquid water by solid water (RW-3, WEPL = 1.025 ± 0.011 [Jäkel et al., 2001]) of corresponding WET ensuring 'dry' measurement conditions (Fig. 6.3). Further, the total WET of RW-3 has been subdivided in RW-3 slabs of different thickness in order to ensure a high flexibility in the set-up as schematically shown in Fig. 6.3 b. Thus, when combining the phantom with a detector having a certain WET until its effective measurement position, this additional off-set can be accounted for by appropriately reducing the total thickness of the RW-3 plates. As a result, it can be ensured that measurements with all kind of detectors refer to the effective measurement position of the water calorimeter. Additionally, the phantom allows to adapt the external monitor chamber, which has been used during the calorimetric and ionometric measurements as an additional monitoring system.

6.3.2 Measurements for field characterization

6.3.2.1 Focus size

In order to determine the focus size of the carbon ion pencil beam at the measurement position of the calorimeter, radiographic EDR2 films (*cf* Sec. 4.4.4) have been irradiated directly behind the water-equivalent slab phantom with mounted external monitor chamber at the geometric measurement position of the calorimetric detector (Fig. 6.4). The same energy and focus size of the carbon ion pencil beam as used for the determination of k_Q have been used (*cf* Tab. 6.1). Per film, five spots with 1.5e8 particles each have been irradiated using the linear working area of the film to full capacity. After the irradiation, the films have been directly developed and scanned as described in Sec. 4.4.4. In order to determine the focus

Beamtime	ρ	FWHM$_{x1}$	FWHM$_{x2}$	FWHM$_{y1}$	FWHM$_{y2}$
BT1 (08/2014)	-0.055 ± 0.002	4.38 ± 0.03	7.42 ± 0.13	4.20 ± 0.02	7.13 ± 0.14
BT2 (12/2014)	-0.053 ± 0.001	4.30 ± 0.05	7.08 ± 0.18	4.14 ± 0.04	6.82 ± 0.17
BT3 (02/2015)	-0.056 ± 0.001	4.49 ± 0.05	7.92 ± 0.18	4.32 ± 0.03	7.69 ± 0.14
mean	-0.055 ± 0.001	4.39 ± 0.06	7.47 ± 0.24	4.22 ± 0.05	7.21 ± 0.25

Table 6.2: *Overview of the mean focus sizes in mm determined before each calorimetric beamtime as well as the overall mean value. In addition, the correlation coefficient ρ is specified. The errors given are the corresponding standard errors.*

size, the following function consisting of a superposition of two 2D Gaussian distributions has been fitted to the measured relative dose distribution of the pencil beam centered at (0,0) after subtraction of the film´s intrinsic background signal:

$$f(x,y) = \frac{A_1}{2\pi\sigma_{x1}\sigma_{y1}\sqrt{1-\rho^2}} \cdot exp\left\{-\frac{1}{2(1-\rho^2)} \cdot \left[\frac{x^2}{\sigma_{x1}^2} + \frac{y^2}{\sigma_{y1}^2} - \frac{2\rho xy}{\sigma_{x1}\sigma_{y1}}\right]\right\} + \frac{A_2}{2\pi\sigma_{x2}\sigma_{y2}\sqrt{1-\rho^2}} \cdot exp\left\{-\frac{1}{2(1-\rho^2)} \cdot \left[\frac{x^2}{\sigma_{x2}^2} + \frac{y^2}{\sigma_{y2}^2} - \frac{2\rho xy}{\sigma_{x2}\sigma_{y2}}\right]\right\} + B\,. \tag{6.1}$$

Here, A is the amplitude, σ_x and σ_y are the spreads of the beam in x and y direction, B an off-set value taking into account any residual background signal, and ρ the correlation coefficient considering a possible asymmetry of the pencil beam. The corresponding FWHM of the pencil beam is then given by $\sigma \cdot 2.3548$. As exemplary shown in Fig. 6.4, the pencil beam can be well described by the given distribution. The focus size has been determined before each of the three calorimetric/ionometric beamtimes with the characteristic values per beamtime summarized in Tab. 6.2. The data shows that the focus size of the carbon ion pencil beam has been very stable over the course of measurements having a negligible asymmetry.

6.3.2.2 Spatial irradiation pattern

The experimental set-up for the investigation of the spatial irradiation pattern at the measurement position of the calorimetric detector is shown in Fig. 6.5. In addition to the two multiwire proportional chambers (MWPCs) of the beam application monitor system (BAMS) positioned in the beam nozzle, an identical MWPC for external use has been positioned behind the water-equivalent slab phantom with its effective measurement position placed at the geometrical measurement depth of the calorimetric detector. Since the WET of the distance between MWPC surface and its effective measurement position is negligible, the total thickness of the water-equivalent slab phantom has not been modified for this experiment. As explained in Sec. 4.4.2, the MWPC allows for a time-resolved measurement of the pencil beam position and with that the localization of each irradiated raster spot. By using the external MWPC at the measurement position of the calorimetric detector, each spot position can be determined under 'real' calorimetric measurement conditions. Meanwhile, the MWPCs of the BAMS measure the same information with respect to their measurement position in the beam nozzle. As described in Sec. 4.5, this information is recorded for each irradiation within the so-called maschine beam records. Thus, by radiating the very same irradiation

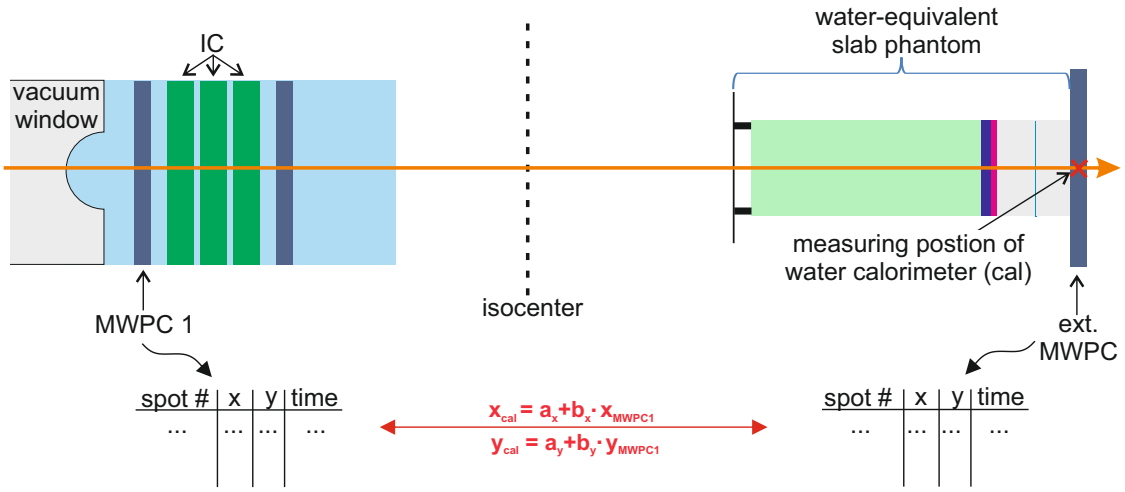

Fig. 6.5: *Experimental set-up for the investigation of the spatial irradiation pattern.*

plan as used for the determination of k_Q, the position of each irradiated spot is measured by MWPC1, MWPC2, and the external MWPC. As schematically illustrated in Fig. 6.5, the information of the position-regulating MWPC1 as well as the external MWPC have been used to determine a mathematical relation between both measuring positions. The following linear relations for the x and y position measured by MWPC1 (x_{MWPC1} and y_{MWPC1}, respectively) and external MWPC (x_{cal} and y_{cal}, respectively) have shown to sufficiently describe the divergence of the ion beam, with a being the y-intercept and b the slope of the line:

$$x_{cal} = a_x + b_x \cdot x_{MWPC1}, \; y_{cal} = a_y + b_y \cdot y_{MWPC1} \; . \tag{6.2}$$

Before each calorimetric beamtime, this experiment has been performed five times enabling the determination of a reliable relation between MWPC1 and external MWPC. This linear function has then been used to transfer the machine beam records of MWPC1 recorded for each 'real' calorimetric measurement to the position of the calorimetric detector. In Tab. 6.3, the parameters of the linear relations determined before each of the three main beamtimes are summarized showing unchanged values for the slopes in both x and y direction. The off-set values a_x and a_y vary within ± 0.3 mm, which is most likely due to uncertainties in the positioning of the external MWPC. Both residual standard errors in x and y are below 0.1 mm.

Beamtime	a_x	b_x	res. std. error x	a_y	b_y	res. std. error y
BT1 (08/2014)	1.16	1.39	0.08	0.60	1.34	0.06
BT2 (12/2014)	0.71	1.39	0.08	0.43	1.34	0.07
BT3 (02/2015)	0.81	1.39	0.09	0.08	1.34	0.08
mean $\pm$ s.e.	1.04 ± 0.28	1.39 ± 0.00	0.08 ± 0.00	0.37 ± 0.15	1.34 ± 0.00	0.07 ± 0.01

Table 6.3: *Fit parameters determined for the linear relation between MWPC1 and external MWPC located at the measurement position of the calorimetric detector. The errors given are the corresponding standard errors. Values for a_x, a_y, and the res. std. errors are specified in mm.*

Beamtime	Time per spot / s	Spill pause / s	# of spills	Irradiation time / s
BT1 (08/2014)	0.032 ± 0.003	4.72 ± 0.16	1×13 spills	13 spills: 104.5
			17×12 spills	12 spills: 95.7 ± 1.2
			9×11 spills	11 spills: 90.4 ± 0.4
			26×10 spills	10 spills: 85.8 ± 0.4
BT2 (12/2014)	0.032 ± 0.001	4.71 ± 0.07	45×14 spills	14 spills: 104.6 ± 0.3
			2×13 spills	13 spills: 99.8 ± 0.2
			30×12 spills	12 spills: 95.4 ± 0.7
BT3 (08/2014)	0.032 ± 0.001	4.73 ± 0.10	78×12 spills	12 spills: 95.5 ± 0.6

Table 6.4: *Temporal structure of the calorimetric irradiations extracted from the machine beam records of MWPC1 not considering the much longer irradiations due to system interlock induced additional beam-off times. The uncertainties given refer to the standard deviations.*

6.3.2.3 Temporal structure of the irradiation

As explained in Sec. 4.5, the position of each irradiated raster spot is recorded by the MWPC of the BAMS together with the corresponding time stamp (*cf* Fig. 6.5) and can thus be used to reconstruct the temporal structure of the entire irradiation, *e.g.* the total irradiation time, the irradiation time per spot position, as well as the spill cycle. The machine beam records of the MWPC1 have been analyzed for each calorimetric measurement performed within this thesis. Although the very same irradiation plan has been used for all measurements, the total irradiation time varies as shown in Tab. 6.4. This effect is mainly caused by a different filling condition of the synchrotron from day to day resulting in the need for more or less spill numbers in order to irradiate the total volume. On the other hand, the time per spot as well as the duration of a spill pause is nearly constant over the time of all three calorimetric/ionometric beamtimes. During some irradiations, system interlocks temporary interrupted the running irradiation. This occurred 7 times during the first beamtime and two times during both second and third beamtime resulting in a much longer mean irradiation time of about 114 s due to the system interlock induced additional beam-off time of about 20 s.

6.3.2.4 Lateral dose distribution

Precise knowledge of the relative lateral dose distribution at the calorimetric/ionometric measurement position is essential as it is required for the determination of multiple calorimetric (k_c, k_l) and ionometric correction factors (k_V). Thus, for the subsequent determination of these correction factors with high accuracy, a detector is needed to measure relative lateral dose distributions with high spatial resolution while offering a low measurement uncertainty. Comparing the different types of detectors available with respect to this specific ion-beam application, the ionization chamber array STARCHECK (*cf* Sec. 4.4.1) was found to offer the best trade-off between spatial resolution, reproducibility of the measurements, as well as accuracy. Before STARCHECK has been applied for the detailed characterization of the irradiation field used for the determination of k_Q, the detector array has been investigated in the well-defined ^{60}Co irradiation field at PTB with the main measurements and results described in the following.

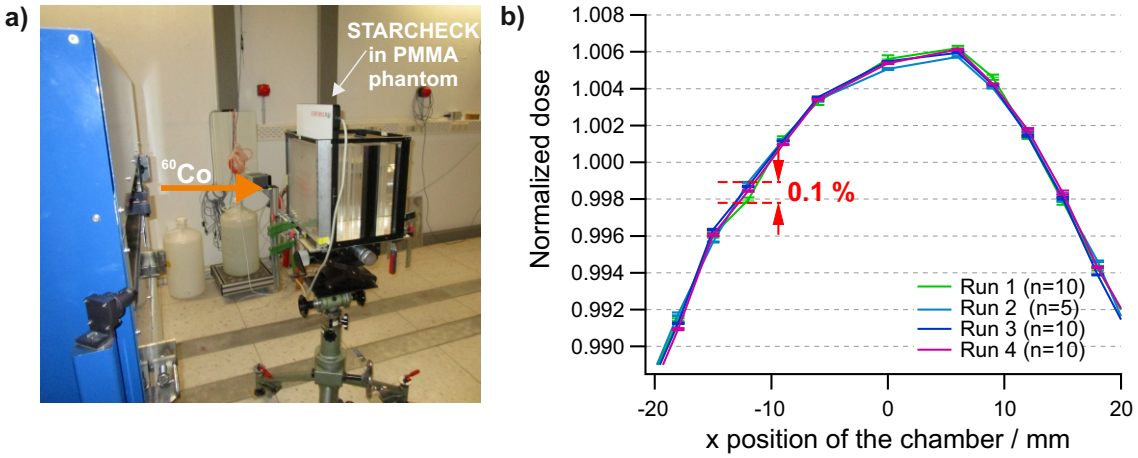

Fig. 6.6: *a) Experimental set-up of the measurements performed in the ^{60}Co irradiation field at PTB for the investigation and calibration of* STARCHECK. *b) Exemplary result of the repeated measurements for a selection of ionization chambers located on the main horizontal axis of* STARCHECK *showing a very good reproducibility.*

Investigation of STARCHECK at PTB

The primary reason for performing measurements with STARCHECK in the ^{60}Co irradiation field at PTB was to investigate the possibility to further decrease the array´s calibration uncertainty of $\pm 1\,\%$ [PTW, 2013b], as the uncertainty of the array and thus of the measured lateral dose distribution has a strong impact on the overall uncertainty of k_Q. In this context, the term 'calibration' is used as synonym for the determination of the relative response of each ionization chamber with respect to the central chamber, which is given as the ratio of the individual ionization chamber reading and the expected measurement value within a ^{60}Co reference field. Additionally, the reproducibility of measurements, which is stated by the manufacturer as $\leq 0.5\,\%$, has been further investigated. All measurements were confined to those ionization chambers of the array which were actually used for the later characterization of the carbon ion field at HIT. Fig. 6.6 a shows the experimental set-up of the measurements performed with STARCHECK at PTB using a source-to-surface distance of 95 cm, a measuring depth of 50 mm in water realized by PMMA-plates of adequate thickness placed in front of the array, sufficient thickness of PMMA as backscatter material, and a field size of $10\,\text{cm} \times 10\,\text{cm}$. The irradiation duration was chosen to 100 s corresponding to an absorbed dose to water of about 1.5 Gy similar to the experimental conditions used for the determination of k_Q in the carbon ion field at HIT. All measurements were corrected for changes in temperature and pressure.

The reproducibility of measurements performed with STARCHECK has been investigated by frequently repeating the very same irradiation over one week with the corresponding data for a selection of ionization chambers exemplary shown in Fig. 6.6 b. As a main result it could be shown that the relative standard deviation of the repeated measurements is well below 0.1 % for all considered ionization chambers.

For the calibration of STARCHECK, only an area of $\pm 20\,\text{mm}$ around the central beam of the well-characterized $10\,\text{cm} \times 10\,\text{cm}$ ^{60}Co irradiation field has been used in order to keep the dose gradient small (only about 1.5 % relative dose difference between central beam and $\pm 20\,\text{mm}$) and thus increase the robustness of the calibration procedure against small misalignments of the ionization chamber array. In order to cover a larger area of the detector

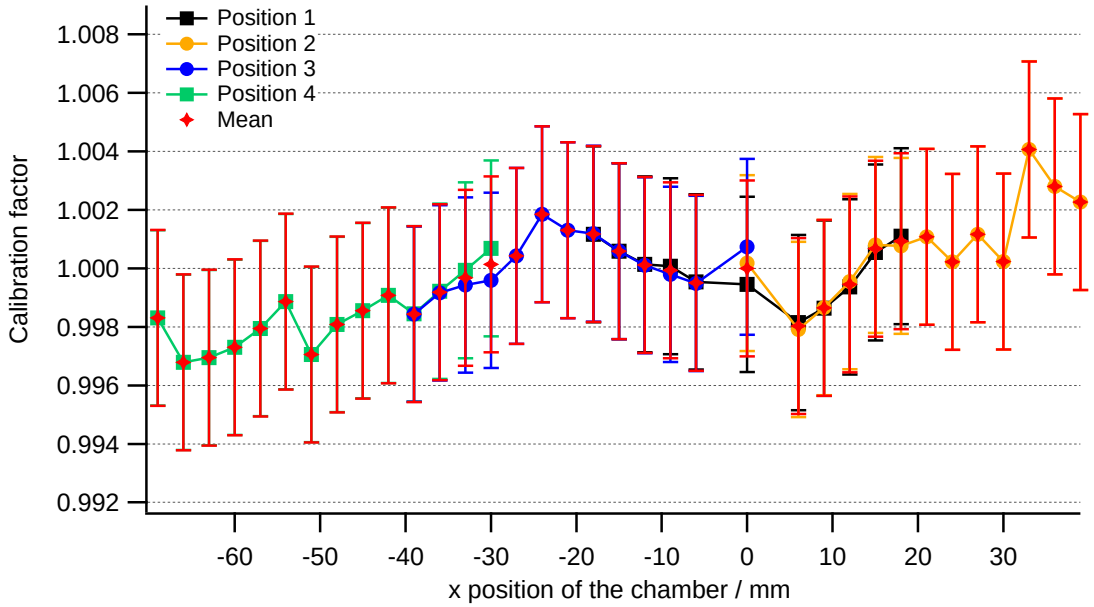

Fig. 6.7: *Final calibration factors, i.e. relative responses with respect to the central chamber, as determined in the ^{60}Co irradiation field at PTB for all ionization chambers positioned on the main horizontal axis of* STARCHECK *being relevant for the measurements performed within this thesis. As a main result it could be shown that a calibration uncertainty of $\pm$ 0.3 % is achievable via an extensive calibration procedure.*

array than $\pm$ 20 mm around the central axis, STARCHECK has been repositioned with respect to the central beam multiple times keeping an overlap of at least 10 mm between adjacent measurement positions. Thus, ionization chambers located within this overlapping area were calibrated twice, which has been used as an internal quality check of the results. The resulting calibration factors, *i.e.* relative responses, for the ionization chambers located on the main horizontal axis of the detector array are exemplary shown in Fig. 6.7. Different colors indicate different lateral positions of STARCHECK enabling the calibration of all ionization chambers located on the horizontal axis of the array being relevant for the measurements performed within this thesis. The final calibration factor per ionization chamber is taken to be the mean value of calibration factors independently determined at different positions with respect to the ^{60}Co irradiation field, which have shown to agree very well as shown in the graph. The relative standard uncertainty of the final calibration factors is estimated to 0.3 % comprising the uncertainty of the lateral dose distribution of the ^{60}Co radiation field at PTB as well as possible misalignments of STARCHECK both in depth and lateral direction. Thus, due to this extensive calibration procedure, a reduction of the calibration uncertainty for the ionization chambers used within this thesis from $\pm$ 1 % as determined by the manufacturer to $\pm$ 0.3 % could be achieved, which has a significant impact on the later determination of ionometric and calorimetric correction factors.

Measurements performed in the carbon ion irradiation field at HIT

Before each of the three main calorimetric/ionometric beamtimes, the lateral dose distribution has been measured by means of STARCHECK behind the water-equivalent slab phantom. Therefore, the effective measurement position of the detector array (8.5 mm below the detec-

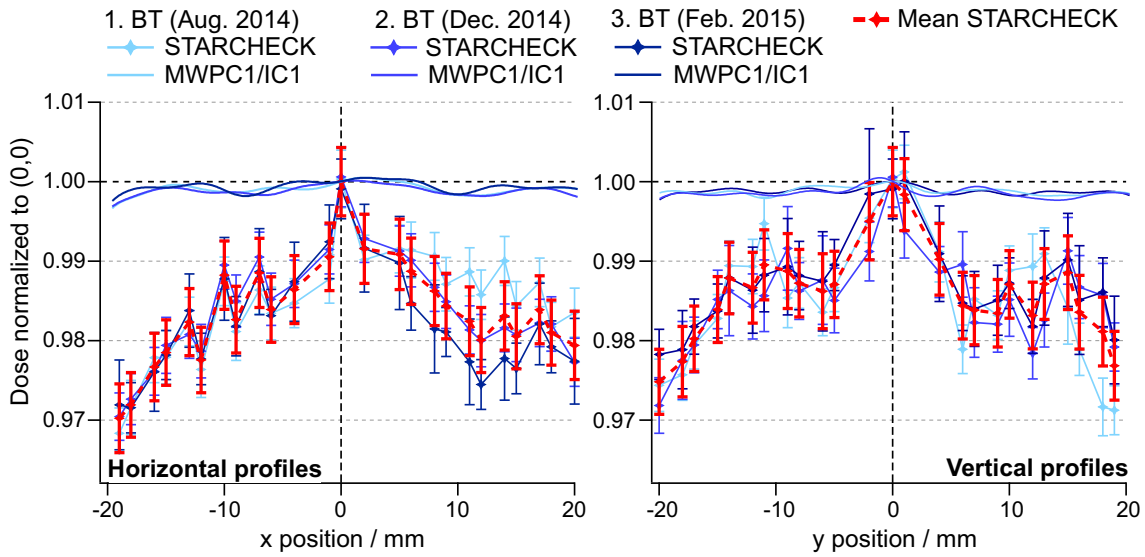

Fig. 6.8: *The figure shows the mean relative lateral dose distributions measured with* STARCHECK *(corrected for its relative response) before each of the three main ionometric/calorimetric beamtimes. The standard uncertainties illustrated by the error bars comprise the calibration uncertainty of 0.3 % as well as the corresponding individual relative standard error of the mean, which was found to be on average below 0.3 % for all repetitive measurements. Over the course of beamtimes, the measured distributions in both horizontal and vertical direction agree well within their uncertainties demonstrating reproducible measurement conditions over time. The standard uncertainty of the resulting mean relative dose distributions (red curves) considers the measurement uncertainties of the beamtime-specific lateral dose profiles as well as the standard deviation from beamtime to beamtime of 0.28 %. In addition to the measured profiles, corresponding relative lateral dose distributions were calculated on the basis of the machine beam records of MWPC1/IC1 as well as the measured focus size of the carbon ion pencil beam. In comparison to the measured data, the calculated profiles show almost homogenous lateral dose distributions.*

tor surface, $\rho = 0.995\ \mathrm{g/cm^3}$ [PTW, 2013b]) has been positioned at the measurement depth of the calorimetric detector. In order to account for this additional detector-specific WET, the amount of RW-3 slabs behind the glass plate of the phantom has been adequately reduced. The same irradiation plan as for the determination of k_Q has been applied (*cf* Tab. 6.1). By using multiple lateral measurement positions of STARCHECK with respect to the central beam, the spatial resolution of the resulting lateral dose distributions could be increased. Fig. 6.8 shows the measured lateral dose profiles normalized to the central beam within the inner 40 mm $\times$ 40 mm area of the irradiated carbon ion field. The data shown has been corrected for the relative response of the STARCHECK chambers as determined at PTB (*cf* Fig. 6.7). The standard deviation for each triple of measured values per ionization chamber has been calculated resulting in an average value over all chambers of 0.28 %. This value can be considered as a measure of reproducibility demonstrating stable lateral dose distributions over the course of beamtimes. Thus, a mean relative lateral dose distribution has been calculated for both horizontal and vertical direction, which will be used for the later determination of corresponding calorimetric and ionometric correction factors.

Already within this central area of the irradiation field, the measured relative dose profiles deviate within $\pm$ 1.5 % showing a maximal difference of 3 % between the central beam and

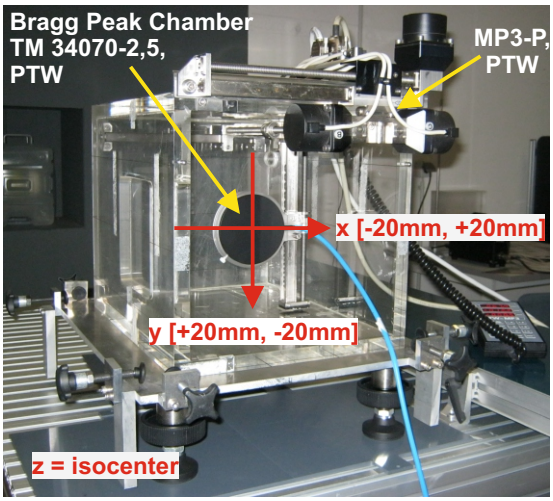

Fig. 6.9: *Experimental set-up used in the QA-room at HIT to test the hypothesis of an spatial dependency of the number of irradiated particles caused by a dysfunction of IC1. As 3D scanning system, the MP3-P in combination with a TANDEM^{XDR} electrometer and corresponding* MEPHISTO *mc^2 software package facilitating data acquisition and evaluation has been used (all from PTW, Germany). For practical reasons, the scanning system was mounted to a water phantom, although the measurements were performed free in air with the Bragg Peak chamber positioned at the isocenter.*

the marginal regions. These large deviations are not expected from the spatial irradiation pattern as derived from the measurements with the position-regulating MWPC1 nor the number of particles delivered to each raster spot as determined by the particle-number regulating IC1, which are recorded for each irradiation within the machine beam records (*cf* Sec. 4.5). As explained in Sec. 6.3.2.2, the information from the MWPC1 can be used to calculate the corresponding spot positions with respect to the measurement depth of the calorimetric detector. By using the spatial irradiation pattern as well as the number of particles delivered to each raster spot, the resulting 2-dimensional dose distribution has been calculated by superimposing single carbon ion pencil beams of measured focus size (*cf* Sec. 6.3.2.1). As shown in Fig. 6.8, the derived dose profiles in both horizontal and vertical direction indicate an almost homogenous irradiation field for all three beamtimes and thus show no agreement with the experimental data. From the previous detailed investigation of STARCHECK, a dysfunction of the ionization chamber array causing the disagreement between experimental and calculated data can be excluded. Thus, the calculated lateral dose profiles are assumed to be incorrect and the measured relative dose distributions are taken to be the 'true' profiles.

Explaining the discrepancy between measured and calculated dose profiles

Although the 'true' relative lateral dose distributions are taken to be the measured profiles, it is important to further investigate the reason for the discrepancy seen, as the information about the spatial irradiation pattern as derived from the measurements with the position-regulating MWPC1 and the relative particle number per raster spot as determined by the particle-number regulating IC1 are essential input data for the later performed heat conduction calculations. Thus, two possible explanations seeming the most likely are hypothesized and tested in the following.

1st hypothesis: Spatial variation of the number of delivered particles One possible explanation for the discrepancy seen between calculated and measured lateral dose distributions could be a spatial dependency of the number of particles irradiated per spot position. With respect to the measured lateral dose distribution in both horizontal and vertical direction, this would mean that significantly more particles were delivered to the central part of the field than to the sides. The reason for this effect could be a spatially dependent dysfunction of

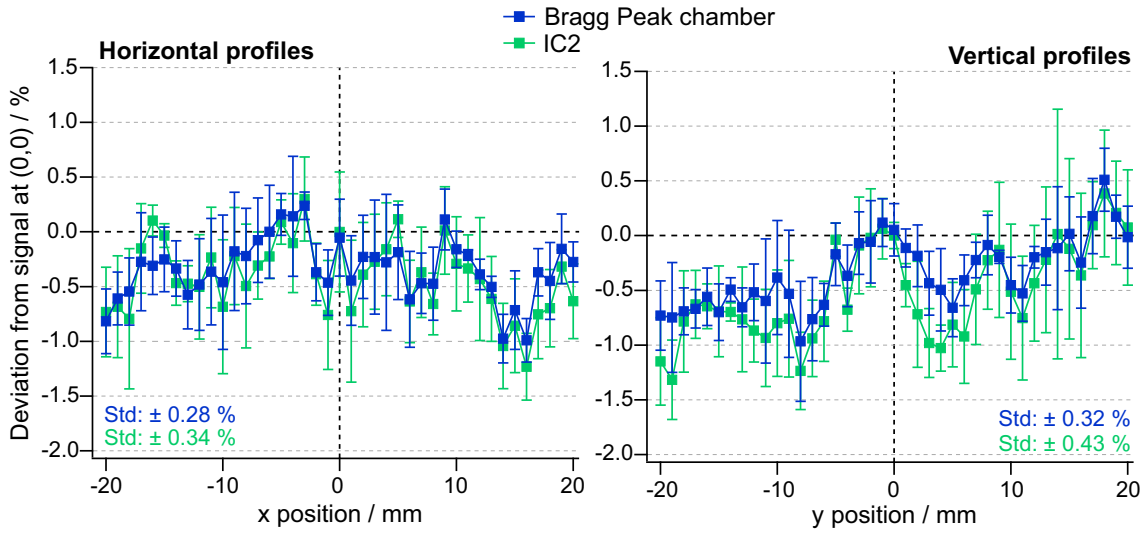

Fig. 6.10: *Mean horizontal and vertical profiles with corresponding standard errors as measured with the Bragg Peak chamber and the redundant IC2 of the BAMS to verify the first hypothesis.*

the particle-number regulating IC1 of the BAMS. In order to test this hypothesis, a plane-parallel Bragg Peak ionization chamber has been chosen as its large diameter (∅: 81.6 mm) allows for the measurement of the complete carbon ion pencil beam including scattered particles. The chamber has been fixed to a 3D scanning system allowing to precisely vary the lateral position of the isocentric positioned chamber in increments of 100 µm (Fig. 6.9). The irradiation plan was generated in such a way that 41 raster spots were positioned on the horizontal axis between ± 20 mm separated by 1 mm and analog for the vertical axis. Per spot position, 8e7 particles were irradiated within the duration of one spill using the same energy and focus size as for the determination of k_Q (*cf* Tab. 6.1). In order to automate the measurement procedure, the 3D scanning system has been synchronized with the spill structure of the synchrotron such that the movement from one pre-defined position to the next (equal positions as in the irradiation plan were used to track each raster spot) was performed during the spill pause. Thus, by measuring the delivered particle number/dose spot by spot on the 1 mm grid with the isocentric Bragg Peak chamber, the performance of the particle-number regulating IC1 could be verified. Both horizontal and vertical profiles were measured four times with the mean profiles shown in Fig. 6.10. As shown in the figure, the relative standard deviation of the particle numbers measured with the Bragg Peak chamber in both horizontal and vertical direction account to only ± 0.3 % with the shape of the profiles showing no similarity to the measured lateral dose distributions shown in Fig. 6.8. In addition to the recorded signal of the IC1, which, as particle-number regulating system, shows a relative standard deviation of 0.001 % concerning the number of delivered particles, the signal of the redundant IC2 has been additionally analyzed and plotted supplementary to the data of the Bragg Peak chamber. Although the relative standard deviation of the signal from the IC2 is slightly higher, both horizontal and vertical profiles agree very well with the corresponding profiles measured with the Bragg Peak chamber thus confirming the validity of the performed experiment. Consequently it can be concluded that the measured lateral dose distributions using STARCHECK are not caused by a spatial variation of the delivered particle number due to a dysfunction of the particle number-regulating IC1. Thus, this first hypothesis could not be corroborated.

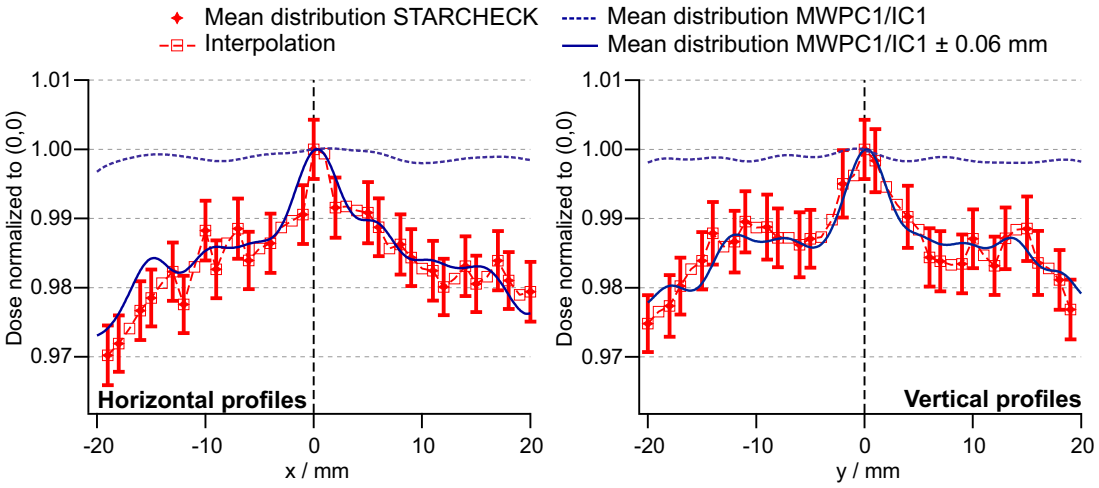

Fig. 6.11: *Comparison of the measured mean lateral dose distributions in horizontal and vertical direction with the corresponding calculated profiles on the basis of the unmodified/modified machine beam records of MWPC1/IC1. The figure demonstrates that a variation of single raster spot positions within ± 0.06 mm due to a possible misplacement of corresponding MWPC1 wires very well approximates the measured profiles.*

2nd hypothesis: Defective raster spot positions Another plausible explanation for the disagreement seen are uncertainties of the raster spot positions as regulated by the MWPC1. If single wires of the MWPC1 are not located at their nominal position but within the given uncertainty of ± 0.1 mm (*cf* Sec. 4.4.2), ion beams delivered to this specific position will have a systematic shift due to the misplaced MWPC1 wires, while the machine beam records of MWPC1 would record the coordinates of the nominal raster spot position. This systematic and therefore permanent effect would also explain the good reproducibility of the lateral dose distributions measured with STARCHECK over the course of beamtimes. It could be shown by repetitive simulations, that by manually varying the position of single raster spots as recorded by the MWPC1 within ± 0.06 mm assuming an systematic shift of the corresponding MWPC1 wires, the measured relative lateral dose distributions in both horizontal and vertical direction can be well approximated by the calculated profiles as shown in Fig. 6.11. Although this hypothesis has not been verified experimentally as the clear separation of this effect from others is challenging, the results from the theoretical verification seem convincing to corroborate this second hypothesis. Thus, these slightly modified raster spot positions have been used for the later simulation of k_c.

6.3.2.5 Depth dose distribution

The depth dose distribution (*ddd*) was measured behind the water-equivalent slab phantom mimicking the water calorimeter using PEAKFINDER (*cf* Sec. 4.4.3) with the experimental set-up shown in Fig. 6.12. Since the PEAKFINDER fails to detect the first 17.4 mm of the Bragg curve in water due to the detector system itself (*cf* Tab. 4.3), the adjustable 19.6 mm RW-3 slabs (corresponding to 20.1 mm WET) behind the glass plate of the phantom have been removed. In this way, the Bragg curve at the measurement position of the water calorimeter at about 20 mm of water behind the glass plate can still be detected. Due to the removal of the RW-3 plates, an air gap of 19.6 mm remained between the glass plate and the surface of the PEAKFINDER. Because of spatial constrains, the phantom and the

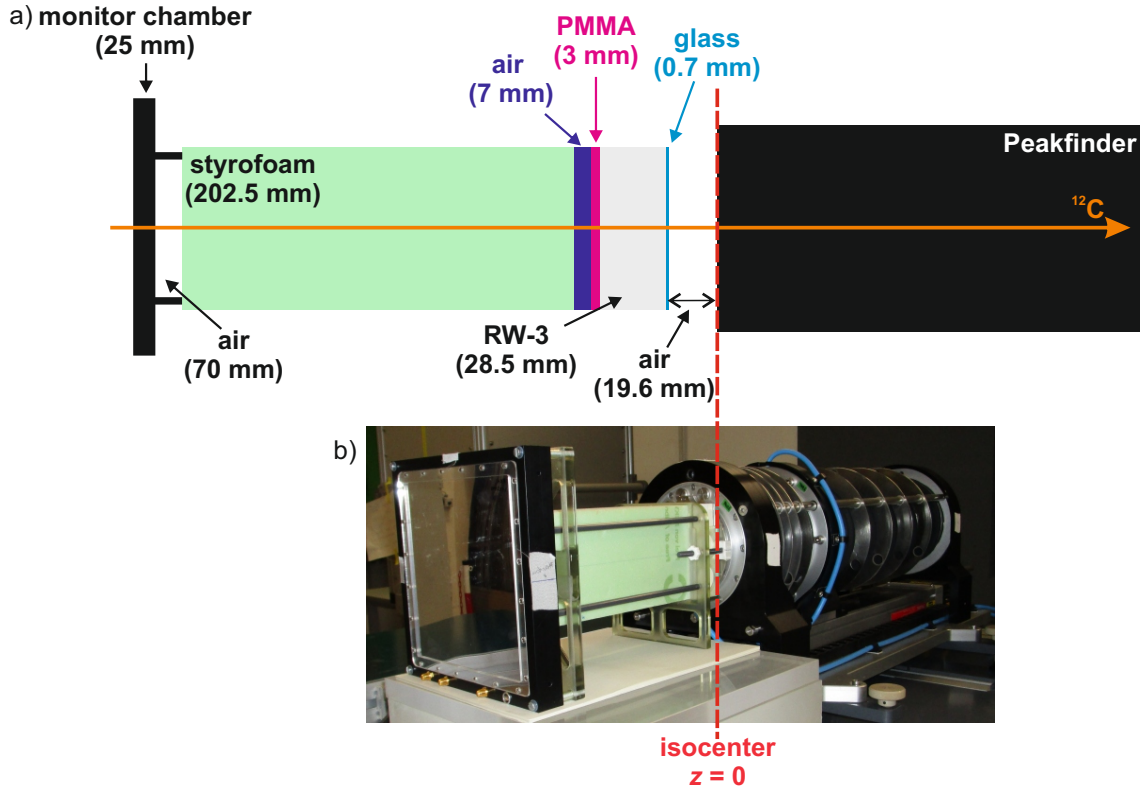

Fig. 6.12: *Experimental set-up for the measurement of the ddd behind the water-equivalent slab phantom mimicking the water calorimeter using* PEAKFINDER. *As illustrated in a), the adjustable 19.6 mm RW-3 slabs behind the glass plate of the phantom have been removed to account for the 17.4 mm off-set of the* PEAKFINDER. *Thus, an 19.6 mm air gap between* PEAKFINDER *and phantom results. Please note that the schematic drawing is not true to scale in the sake of better illustration of thin materials.*

PEAKFINDER could not be set-up at the off-isocentric measurement position of the water calorimeter. Instead, the surface of the PEAKFINDER was positioned at the isocenter of the QA-room at HIT with the phantom placed directly in front. The irradiation was performed using the same settings as for the calorimetric measurements (*cf* Tab. 6.1), with the only exception of a continuous, isocentric pencil beam instead of a scanned field. The step-size of the measurement was varied between 1 mm around the measurement position of the water calorimeter, 10 mm in the residual flat entrance region, 2 mm in the raising area of the Bragg Peak being step-wise decreased to 0.1 mm directly around the Bragg Peak and 5 mm in the tail region. This allows for an optimal resolution of the Bragg curve in reasonable measurement time. The geometrical difference between the off-isocentric position of the water calorimeter and isocentric performed PEAKFINDER measurements has been accounted for by adding an appropriate water-equivalent shift to the measured *ddd*. Fig. 6.13 shows the normalized PEAKFINDER signal plotted against the geometrical depth in the water calorimeter starting from its PMMA entrance window. In this geometry, the nominal calorimetric measurement position is located at a depth of 50 mm with the Bragg Peak measured at about 290 mm. The residual range, R_{res}, needed to specify the beam quality for the calculation of $(s_{w,air})_Q$ and thus k_Q according to DIN 6801-1 (*cf* Sec. 3.1) amounts to 241 mm. The zoomed insert emphasizes the flat depth dose distribution around the calorimetric measurement position having a very small relative dose gradient of -0.023 %/mm.

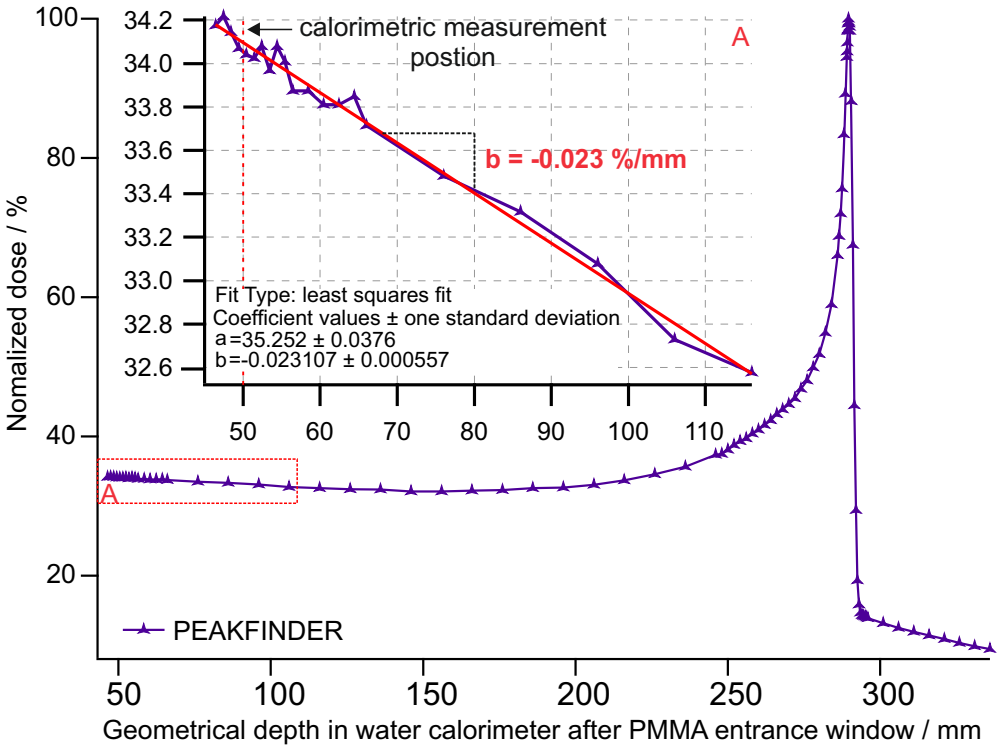

Fig. 6.13: *Depth dose distribution measured behind the water-equivalent slab phantom using* PEAKFINDER. *The zoomed insert emphasizes the flat ddd around the calorimetric measurement position at 50 mm depth showing a very small relative dose gradient of -0.023 %/mm.*

Additional PEAKFINDER measurements have been performed free in air (reference curve), behind 271.45 mm styrofoam, and behind the external monitor chamber to investigate the influence of these materials on the measured Bragg curve and determine their WET as described in Sec. 2.4. As shown in Fig. 6.14, styrofoam leads to a widening of the Bragg peak with respect to the reference Bragg peak measured free in air. This effect is caused by the primary and secondary particles experiencing range straggling when passing the inhomogeneous styrofoam (*cf* Sec. 2.3). In comparison, the monitor chamber does not change the shape of the Bragg peak and can thus be assumed as a composition of homogenous materials. Further, the experimentally determined WET of the materials as well as the corresponding WEPL are summarized in the figure being important parameters for the later performed MC simulation of the calorimetric experiment.

6.3.2.6 Reproducibility of the irradiation

In order to monitor the long-term reproducibility of the beam delivery system, frequent measurements were performed with a Farmer-type ionization chamber (TM30013 S/N 1714, PTW). Therefore, the ionization chamber has been positioned in an RW-3 phantom located in the isocenter of the QA-room at HIT (Fig. 6.15, insert). The very same irradiation plan as used for the determination of k_Q has been applied (*cf* Tab. 4.3). As shown in Fig. 6.15, more than 140 measurements were performed over a period of 7 months covering the course of all three ionometric/calorimetric beamtimes as indicated in the graph. The data shows that the beam delivery system at HIT in combination with the irradiation plan used allows for very reproducible measurement conditions with a relative standard deviation of only $\pm 0.3\,\%$.

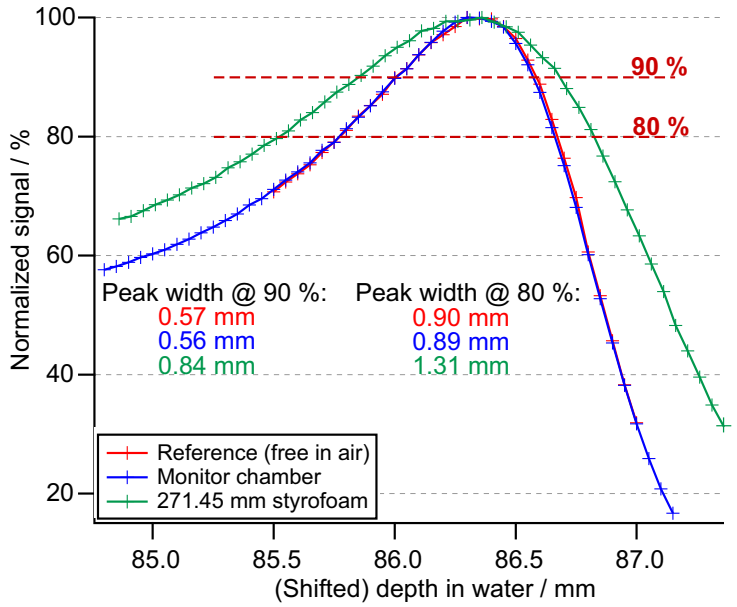

	Styrofoam	Monitor chamber
Length	271.45 mm	25.00 mm
WET	8.64 mm	2.84 mm
WEPL	0.032	0.114
Δ	±0.5 %	±0.2%

Fig. 6.14: *Bragg peaks measured with* PEAKFINDER *free in air (reference curve), behind 271.45 mm styrofoam, and behind the external monitor chamber used during the calorimetric and ionometric measurements. The measured curves are shifted with respect to the Bragg peak position of the reference curve in order to emphasize similarities/differences concerning the peak width. The table on the right summarizes the results of the* PEAKFINDER *measurements, namely the WET of the material and the corresponding WEPL. The uncertainties given are the relative standard errors of the repeated measurements.*

6.3.3 MC simulation of the particle spectrum

Prior to the MC simulation of the particle spectrum at the measurement position of the water calorimeter, the *ddd* measured with PEAKFINDER behind the phantom mimicking the water calorimeter (*cf* Sec. 6.3.2.5) has been used as reference data to assess the optimal configuration of the MC simulation best reproducing the measured Bragg curve. In the following, the MC simulation of the PEAKFINDER experiment will be described in detail being the basis for the final MC simulation of the particle spectrum under real calorimetric measurement conditions. All simulations described in the following were performed with the FLUKA code version 2011.2c.0.

6.3.3.1 MC simulation of the PEAKFINDER experiment

Geometry The phantom mimicking the water calorimeter was simulated in FLUKA by using rectangular material slabs of $10\,cm \times 10\,cm$ and corresponding thickness as depicted in Fig. 6.12 a. Tab. 6.5 summarizes the implementation of the different materials in the FLUKA simulation including the constituents of the monitor chamber. Except for air, PMMA and water, where the parameters currently used at HIT were adopted [personal communication Thomas Tennosier, PhD student at HIT], FLUKA's pre-defined materials were used when available, for which the Sternheimer density effect parameters and ionization potentials (I-values) can be found in Sternheimer et al. [1984]. The ratio of polystyrene and air constitut-

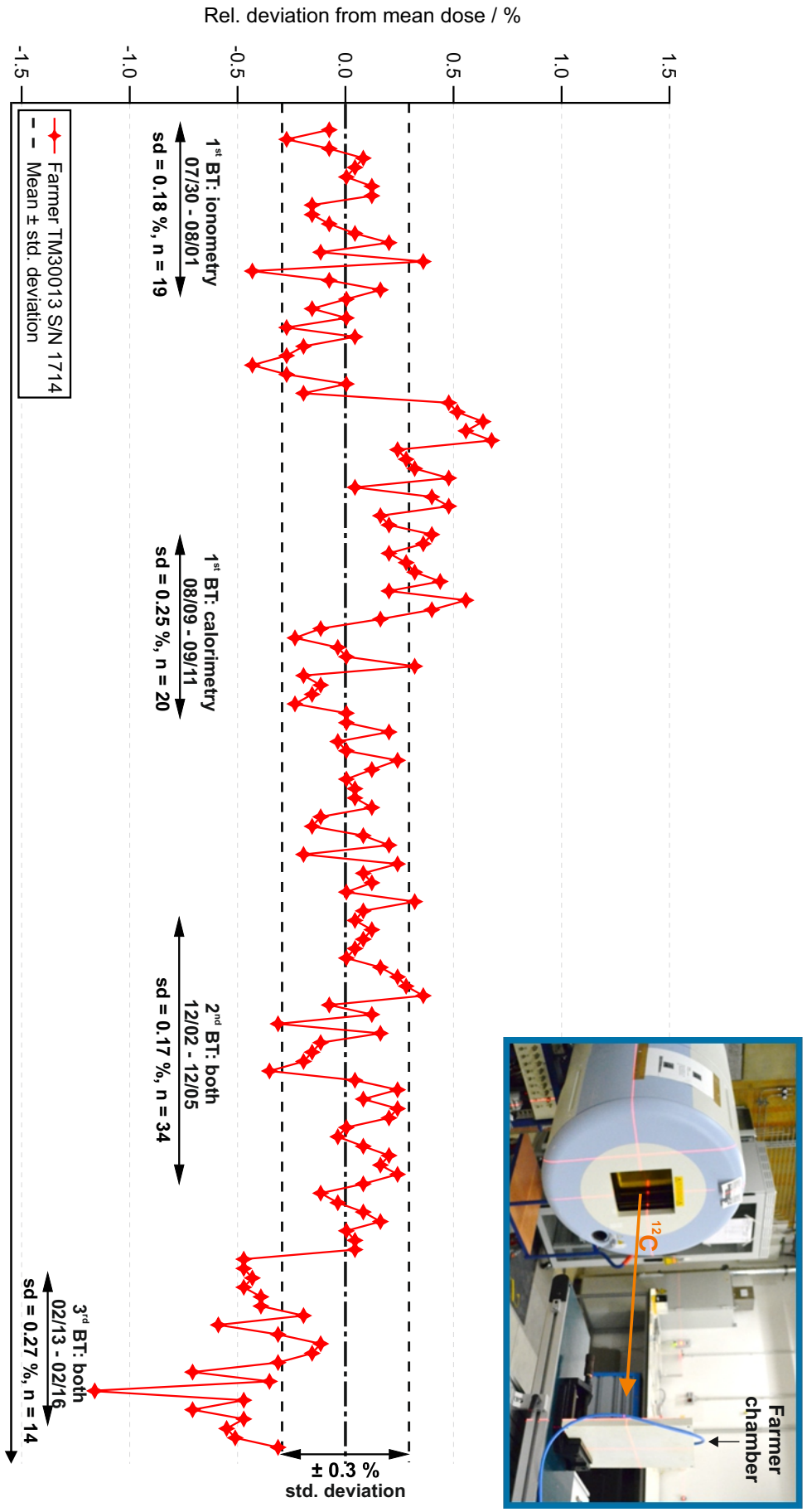

Fig. 6.15: *Long-term reproducibility of the beam delivery system at the QA-room at HIT monitored over the course of the calorimetric and ionometric measurements performed for the determination of k_Q. The insert shows the experimental set-up used.*

Element	Implementation in FLUKA	Comment
Monitor chamber		
- 0.1 mm graphite	0.1 mm 906 graphit (carbon)	Pre-defined in FLUKA
- 0.2 mm parachute silk	0.2 mm Nylon du pont elvamide 8062m	Pre-defined in FLUKA
- 0.005 mm aluminum	0.005 mm aluminum	Pre-defined in FLUKA
- 2 mm PMMA	2 mm PMMA^{HIT}	$\rho = 1.19\,\frac{g}{cm^3}, I = 74.0\,eV, \bar{C} = 3.329, X_0 = 0.1824, X_1 = 2.6681, a = 0.11433, m = 3.3836$
- 22.695 mm air	22.695 mm air^{HIT}	$\rho = 0.0012\,\frac{g}{cm^3}, I = 85.7\,eV, \bar{C} = 10.5961, X_0 = 1.7418, X_1 = 4.2759, a = 0.10914, m = 3.3994$
70 mm air	70 mm air^{HIT}	already defined above
202.5 mm Styrofoam	- 6.154 mm 226-Polystyrene - 196.346 mm air^{HIT}	Pre-defined in FLUKA, $\rho = 1.06\,\frac{g}{cm^3}$ already defined above
7 mm air	7 mm air^{HIT}	already defined above
3 mm PMMA	3 mm PMMA^{HIT}	already defined above
28.5 mm RW-3	29.25 mm water^{HIT}	Calculated by means of $WEPL_{RW\text{-}3} = 1.025 \pm 0.011 (\pm 1.07\,\%)$ [Jäkel et al., 2001], Water^{HIT}: $\rho = 0.998\,\frac{g}{cm^3}, I = 76.8\,eV, \bar{C} = 3.5017, X_0 = 0.24, X_1 = 2.8004, a = 0.09116, m = 3.4773$
0.7 mm BOROFLOAT® 33 glass	0.7 mm BOROFLOAT glass	Self-defined by its chemical composition (13 % B_2O_3, 4 % Na_2O/K_2O, 2 % Al_2O_3, 81 % SiO_2) and density ($\rho = 2.2\,\frac{g}{cm^3}$) as stated by SCHOTT. The corresponding I-value of 135.8 eV was calculated according to Bragg's additivity rule for compounds given in Eq. 2.2.
19.6 mm air	19.6 mm air^{HIT}	already defined above
PEAKFINDER	300 mm water^{HIT}	17.4 mm PEAKFINDER-off-set is already considered in the experimental data. Thus, the simulated PEAKFINDER is approximated as a water phantom starting at the isocenter.

Table 6.5: *Overview of the implementation of the different materials in the* FLUKA *simulation.*

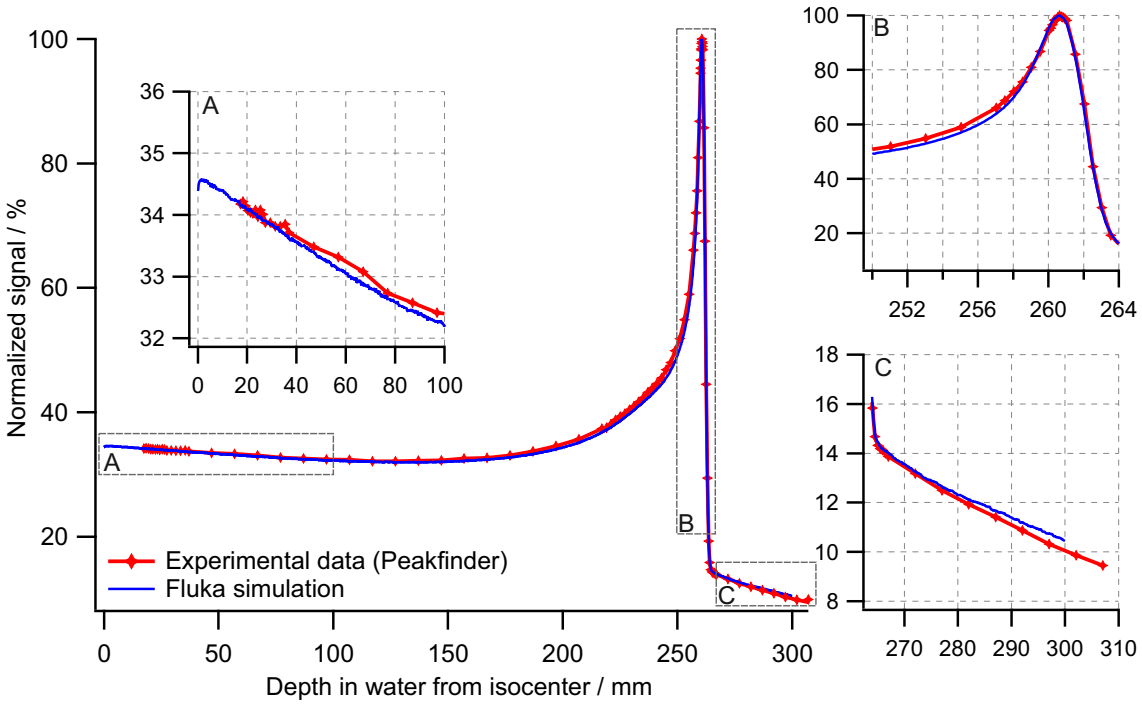

Fig. 6.16: *Comparison of experimental and MC simulated ddd behind the modified water-equivalent slap phantom. The statistical uncertainties associated with the MC simulated values are typically well below 0.5 % and are omitted in the graph for clearness.*

ing styrofoam was estimated according to

$$x \cdot \rho_{poly} + (1-x) \cdot \rho_{air} = \rho_{styr} \;\Rightarrow\; x = 0.0297\,, \tag{6.3}$$

with the density of styrofoam measured to $\rho_{styr} = 32.65\,\frac{kg}{m^3}$ and the densities of polystyrene and air given in Tab. 6.5. Thus, the styrofoam used within this thesis consists of approximately 97 % air and 3 % polystyren. Using this composition, the experimentally determined WEPL of styrofoam as given in Fig. 6.14 is in good agreement with the MC simulated WEPL. In order to account for the energy straggling caused by the inhomogenous nature of styrofoam as shown in Fig. 6.14 while using the simplest approach of a homogenous geometry within FLUKA, an artificial energy spread has been added to all primary and secondary particles in the MC simulation before passing the phantom. The PEAKFINDER was mimicked as a water phantom of 10 cm$\times$ 10 cm $\times$ 30 cm positioned at the isocenter ($z = 0$). The PEAKFINDER off-set is not considered in the MC simulation, since it is already taken into account in the experimental data. In order to include the vacuum window and the beam monitor system (BAMS) of the beam nozzle at HIT, the appropriate phase-space (PS) file without ripple filter provided by HIT has been used [Tessonnier et al., 2016]. This file contains the full particle spectrum of primary and secondary particles of the nominal requested beam after the passage of the beam nozzle (*i.e.* origin of PS at $z = -112.6$ cm before the isocenter) and thus serves as a starting point for the MC simulation of user-specific experimental set-ups. For the simulation of the PEAKFINDER experiment, a ^{12}C pencil beam with a diameter of 3.4 mm FWHM with respect to the isocenter (F1) and a nominal energy of 428.77 MeV/u (E254) impinged from air on the phantom and the PEAKFINDER along the positive z direction as illustrated in Fig. 6.12.

Laterally integrated *ddd* The laterally integrated *ddd* was estimated by scoring the energy deposition (DOSE) within the water phantom mimicking the PEAKFINDER ($z = 0$ cm to $z =$ 30 cm) using FLUKA's USRBIN scorer. In order to best reproduce the measured Bragg curve shown in Fig. 6.16, a spatial resolution of the simulated *ddd* in z-direction of 0.1 mm was chosen. Therefore, the charged hadron transport step size in all materials had to be decreased by a factor of 10 to a corresponding 0.5 % loss of kinetic energy via the FLUKAFIX card, while all other parameters were set as described in Sec. 4.6. Input values of the energy spread and material composition of styrofoam were regarded as the sensitive parameters to be adjustd on the basis of the experimental data in an iterative trial-and-error approach. Further, for a fair comparison with the experimental data, the finite acceptance of the PEAKFINDER had to be included in the MC modeling. As shown in Parodi et al. [2012], a sufficient approach is the restriction of the radial scoring using USRBIN to the 4.08 cm active radius of the measuring thin-window Bragg peak chamber. In total, 500000 primary particles have been simulated resulting in statistical uncertainties generally below 0.5 %.

Comparison of simulated and measured data It has been shown that an energy distribution of 0.2 % FWHM and styrofoam composed of 6.154 mm polystyrene (3.04 %) and 196.346 mm air (96.96 %) yields the best agreement with the experimental data as shown in Fig. 6.16. The deviation between experimental and simulated data is in the order of 0.2 pp (percentage points) in the entrance channel, maximal 2.0 pp ($\hat{=}$3 % of the experimental data) in the raising shoulder of the Bragg peak and about 0.4 pp in the tail region. The underestimation of dose in the raising shoulder of the Bragg peak while showing good agreement with the experimental *ddd* in the falling part indicates that energy/range straggling taking place in styrofoam is not - as assumed - Gaussian distributed (*cf* Sec. 2.3). Most likely, the distribution of air bubbles with different radii causing the inhomogeneous nature of styrofoam is not normally distributed resulting in a higher percentage of particles having lower energies than higher energies after passing styrofoam. Thus, more particles deposit their dose in the raising shoulder of the Bragg peak then in the falling part explaining the differences seen in Fig. 6.16. Since the calorimetric measurements are performed in the entrance channel of the ion beam with a very small gradient of the *ddd*, the impact of the differences seen in the raising area of the Bragg peak can be assumed to be minor.

6.3.3.2 MC simulation of the particle spectrum and dose deposition at the measurement position of the water calorimeter

Geometry The 'real' set-up of the water calorimetric measurements performed at the experimental beam-line at HIT has been implemented in FLUKA using the knowledge gained from the PEAKFINDER experiment, namely an energy spread of 0.2 % FWHM, the exact composition of styrofoam as well as the implementation of all other materials as given in Tab. 6.5. In comparison to the phantom, the water calorimeter embodies a water phantom filled with liquid water (implemented in FLUKA as $\text{water}_{\text{HIT}}$) in which the glass cylinder is located. The thermistor probes are centrally arranged in the glass cylinder at about 50 mm depth of water (49.3 mm water + 0.7 mm glass) as schematically shown in Fig. 4.1 b. Further, both front and rear wall of the glass cylinder have been taken into account with the exact dimensions given in Fig. 4.1 b. Further, the distance between the water calorimeter surface and the isocenter of 655 cm (Fig. 6.1) has been explicitly considered in the MC simulation. Except for the thermistor probes, which have not been included in the MC simulation, all

other constituents of the water calorimeter and the monitor chamber have been accurately taken into account as discussed in Sec. 6.3.3.1 having a slab size of 30 cm × 30 cm. In order to simulate the particle spectrum and dose deposition of primary particles and fragments at the measurement position of the water calorimeter, following additions to the settings used in the MC simulation of the PEAKFINDER experiment were made: (I) The δ-ray production by muons and charged hadrons has been deactivated, which means that their energy transfer is assumed to take place as continuous energy loss and (II) the transport cutoff in terms of kinetic energy has been reduced via FLUKA's PART-THRES card by a factor of 10 to 10 keV for all charged hadrons allowing more accurate particle transport. In total, 300000 primary particles were simulated allowing a good compromise between computational speed and statistics.

Scoring The absorbed dose deposited at the measurement position of the thermistor probes was estimated using USRBIN in a water region of 1 mm thickness (approximately the sensitive area of the thermistor probes) and a cross-section of 30 cm × 30 cm. In addition to the scored dose deposited by all particles, D_{all}, FLUKA's AUXSCORE card has been used in order to filter the dose deposited by particles with atomic number Z=1 to Z=6 regardless of their mass number M. The particle spectrum was estimated using FLUKA's USRYIELD detector allowing to score a double-differential particle yield around an extended target. Here, USRYIELD has been applied to a cross-section of 30 cm × 30 cm water at the measuring depth of the thermistor probes to score the particle yield $\frac{d^2N}{dLET\,dE}$ with respect to LET and energy E. The LET was scored linearly from 0 -100 keV/µm in bins of 0.1 keV/µm width, while the kinetic energy was scored in one interval from 0 - 10 GeV including all particles expected in the simulation. Again, FLUKA's AUXSCORE card has been applied to filter the particle yield by atomic number Z.

Results Fig. 6.17 summarizes the final results of the MC simulation. The plot shows the number of particles, N, per primary simulated particle, N_0, over the LET in keV/µm differentiating the particles by atomic number Z. In addition, the median LET is highlighted. As expected, carbon ions (Z = 6) show the most narrow peak at the highest median LET of 11.3 keV/µm corresponding to a kinetic energy of about 368 MeV/u. This value is in agreement with the expected energy loss of the primary carbon ions (E = 428.77 MeV/u) passing the corresponding WET from the synchrotron to the measurement position of the water calorimeter. The lightest particles with Z=1 show the broadest peak at the lowest median LET of 0.4 keV/µm, while all other particles with Z = 2 to 5 are located in between. The yield of the different particles with respect to the total number of particles scored as well as their contribution to the total deposited dose (D_{all}) is given in the inserted table. Protons, deuterons and tritons (Z = 1) dominate the particle spectrum with a fraction of 48 %, while carbon ions only contribute with 39 % to the total number of particles scored at the measurement position of the water calorimeter. However, due to the difference in LET, the total dose is mainly deposited by carbon ions (85 %), while the dose contribution of particles with Z=1 is only 8 %. Helium ions (Z = 2) make 10 % of the total number of particles, while their contribution to the deposited dose is only 3 %. Lithium (Z = 3), Beryllium (Z = 4), and Boron (Z = 5) are rare in the spectrum (less than 2 % each) and deposit all together about 4 % of the total dose. Particles with higher Z have not been explicitly considered in the simulation, since the sum over the doses from $Z = 1$ to 6 agrees within 99.8 % with the total deposited dose

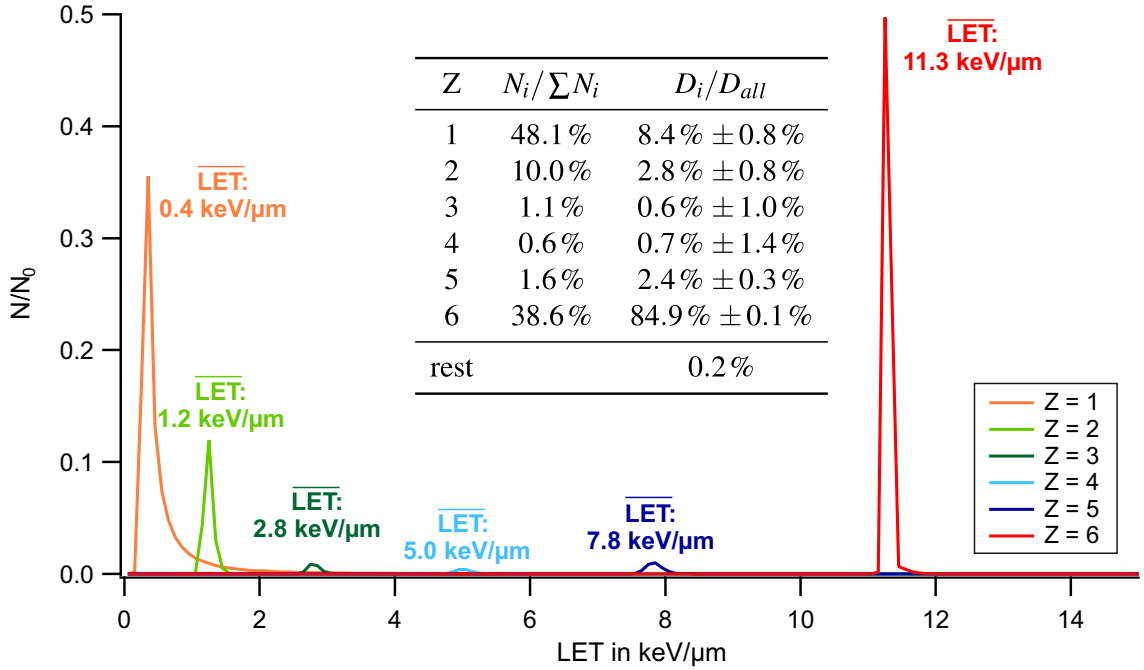

Z	$N_i/\sum N_i$	D_i/D_{all}
1	48.1 %	8.4 % ± 0.8 %
2	10.0 %	2.8 % ± 0.8 %
3	1.1 %	0.6 % ± 1.0 %
4	0.6 %	0.7 % ± 1.4 %
5	1.6 %	2.4 % ± 0.3 %
6	38.6 %	84.9 % ± 0.1 %
rest		0.2 %

Fig. 6.17: *The figure summarizes the results of the MC simulation at the measurement position of the water calorimeter showing (I) the yield of the different particles with respect to LET (median LET highlighted), (II) the percentage of the different particles with respect to the total number of particles scored, as well as their (III) percental contribution to the total deposited dose. The errors given for the dose estimation are directly taken from the MC simulation and thus only consider statistical uncertainties.*

scored independent of particle type. Thus, target fragments like oxygen and other heavier fragments only contribute with 0.2 % to the total deposited dose and are therefore neglected in the particle spectrum shown. The statistical uncertainties concerning the MC-based dose calculation are between 0.1 % for carbon ions and 1.4 % for Beryllium. However, these uncertainties do not include so-called type B uncertainties, which are assumed to be in the order of a few percent concerning the calculation of dose as shown in Parodi et al. [2012], but have shown to increase up to some tens of percent for differential quantities like the particle yield with respect to LET and energy as stated in Böhlen et al. [2014].

6.4 Calorimetric measurements

For each of the three beamtimes, between 60 and 80 calorimetric experiments were performed within 2 successive night shifts for the determination of D_w resulting in a total number of 219 calorimetric measurements. Within these irradiations, two different hydrogen-saturated calorimetric detectors were used (*cf* Tab. 6.6), which were routinely employed in the primary standard water calorimeter at PTB in ^{60}Co radiation in order to prove the response of the detectors. The nominal measurement depth of the thermistors was set to 50 mm with respect to the beam entrance window of the water phantom as shown in Fig. 4.1. As the distance of the glass cylinder with respect to the beam entrance window can slightly change with time due to a bowing of the PMMA window caused by the water pressure, the spacing has been frequently checked directly before and after each calorimetric beamtime. The mean

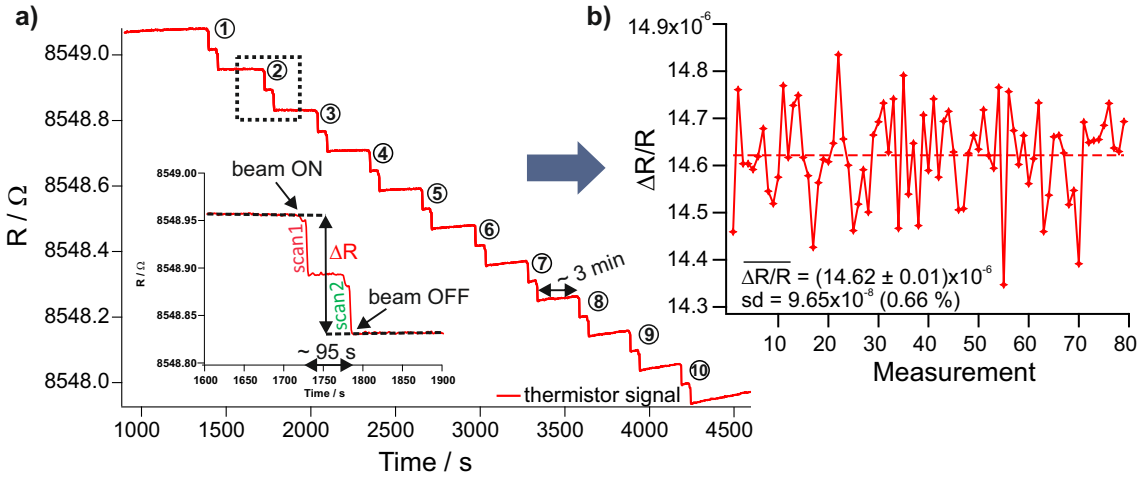

Fig. 6.18: *a) Typical calorimeter signal for 10 consecutive irradiations. The insert shows the enlarged temperature-dependent resistance change for one irradiation with the corresponding linear fits to the pre- and post-irradiation drift curves for the determination of ΔR. The step shown in the signal is due to the irradiation pattern consisting of two shifted rescans (cf Fig. 6.2). The resulting $\Delta R/R$ values needed for the determination of D_w are shown in b) for all 80 measurements performed with the thermistor probe E23 during the course of the third calorimetric beamtime performed in Feb. 2015.*

value has then been taken as real measurement position of the water calorimetric detector, although for all three calorimetric beamtimes, this effect has shown to be almost negligible. Additonally, during all calorimetric and ionometric measurements, the irradiation was monitored by means of a large-area transmission ionization chamber mounted directly in front of the radiation entrance window of the calorimeter (*cf* Fig. 4.1 b), which was corrected for a change in the air density throughout the measurements. This data has been used as an additional quality check of the irradiation stability.

For the specific irradiation conditions used within this thesis (*cf* Tab. 6.1), ten consecutive irradiations with a break of about 3 min in between could be performed within one run before the water calorimeter had to be reconditioned in order to remove radiation-induced temperature gradients in the water. Therefore, the water has been stirred for five minutes followed by a waiting time of about 50 min until residual temperature drifts were small enough allowing for further accurate calorimetric measurements. Figure 6.18 a shows a typical thermistor signal for a series of ten irradiations with the radiation-induced resistance change for one measurement enlarged depicted in the insert. Time intervals of 110 s each were used to perform linear fits to the signal of the pre- and post-irradiation drift curves in order to extrapolate the corresponding signals to the mid-run position. As the thermistor probe and the surrounding water exhibit different specific heat capacities and mass-energy-absorption coefficients, a small temperature difference between the thermistor probe and the surrounding water occurs just at the beginning of an irradiation and remains almost constant until the end of the irradiation. Afterwards, the temperature decreases approximately exponentially with time [Krauss, 2006b], which is accounted for in the linear fit of the post-irradiation drift curve by using an off-set of 10 s. The resulting difference between the extrapolated pre- and post-irradiation drift curves at mid-run position is then used to calculate $\Delta R/R$ (Fig. 6.18 b) needed for the determination of ΔT. D_w has been obtained separately for each thermistor according to Eq. 4.4 using the correction factors given in the following section with the mean

value of both D_w-values taken as the final result of a calorimetric beamtime. For the determination of the thermistor sensitivity S according to Eq. 4.2, the thermistor-specific B-values as given in Tab. 6.6 were used together with the water temperature, T, recorded throughout the calorimetric measurements.

6.4.1 Determination of correction factors and their uncertainties

According to Eq. 4.4, several correction factors are required for the calorimetric determination of D_w and the subsequent calculation of k_Q. The values of the correction factors were partly obtained by experiments, by calculations, or by both. In the following, each correction factor will be addressed separately including a detailed investigation of uncertainties.

6.4.1.1 Heat defect k_h

In the case of hydrogen-saturated water, it has been shown for ^{60}Co γ-radiation that the assumption of a zero heat defect after a small pre-irradiation dose is reasonable within a relative standard measurement uncertainty of 0.14 % [Krauss, 2006b]. Sassowsky and Pedroni [2005] performed model calculations of the radiolysis of water for proton radiation up to an LET of 25 keV/µm showing that the finding of a zero heat defect for the H_2-system is independent of LET, which confirmed the results obtained by Palmans et al. [1996]. It is assumed that this result is also valid for heavier ions within the investigated LET-region. Consequently, for the determination of $D_{w,Q}$ by means of water calorimetry in the scanned carbon ion beam at HIT having an maximum LET of about 11.3 keV/µm (*cf* Fig. 6.17), the correction factor for the heat defect, k_h, is taken to be 1.00 ± 0.14 %. However, before a detector was used at HIT, its response was proven in ^{60}Co γ-radiation at PTB to be stable and to coincide with the expected response of a zero heat defect at least within 0.1 %. This margin is considered as a possible further contribution to the uncertainty of the heat defect.

6.4.1.2 Heat conduction correction k_c

In order to account for the heat conduction effects occuring during and after a calorimetric measurement as discussed in Sec. 4.1.2.2, the real calorimetric measurement conditions need to be reproduced as precise as possible within finite-element calculations. Within this thesis, the heat conducution effects were modeled using COMSOL Multiphysics version 4.3a by Dr. Achim Krauss from PTB. For static irradiation fields, the method is well established with a detailed description given in Krauss [2006b], while the model applied for the transfer to scanned ion beams is a recent development and has thus not yet been published. Preliminary studies concerning the general application of heat conduction calculations with respect to scanned ion beams can be found in [Krauss, 2006a] and [Sassowsky and Pedroni, 2005], while a very similar approach for the calculation of heat conduction effects in scanned ion beams as used here has been simultaneously developed within a Master´s project performed at the Dutch metrology institute VSL [Zavgorodnyaya, 2015]. Briefly, in comparison to static irradiation fields, it is not feasible for scanned ion beams to model the entire irradiation field by computing every single irradiated raster spot as computational time and memory requirements would be unacceptably high. Thus, instead of modeling all 1352 raster spots used for the calorimetric measurements, only a single pencil beam was applied to the center of the water calorimeter and modeled within COMSOL Multiphysics recording the time-

and space-dependent evolution of the resulting temperature drifts during and after the irradiation within a sufficiently fine grid. This information was then used to superimpose the temperature drifts of the very same modeled pencil beam according to the spatial irradiaton pattern and time structure used in the calorimetric measurement to simulate the total temperature rise with respect to the measurement position of the thermistor probe. In Zavgorodnyaya [2015] it has been shown that this kind of convolution model is suitable for both homogenous and inhomogenous irradiation fields realizing a fast and flexible method easily applicable to different scanning patterns. k_c is then determined from such calculations by analysing the calculated excess temperature, which is the ratio of the calculated temperature with and without heat conduction being taken into account, with the same linear fit method and within the same time intervals as applied for the experimental calorimetric data.
Within the finite-element calculations, which were performed using a rotational symmetric 2-dimensional geometry model of the water phantom including the flat glass walls of the detector cylinder, the mathematical expression given in Eq. 6.1 has been used to describe the heat generating dose distribution of the carbon ion pencil beam. In order to use a 2-dimensional rotational symmetry for the calculations, a mean symmetric 2-dimensional Gauss distribution has been assumed on the basis of the measured FWHM as given in Tab. 6.2. The spatial irradiation pattern has been extracted from the modified machine beam records of MWPC1 as explained in Sec. 6.3.2.2 and Sec. 6.3.2.4, which has shown to reproduce the measured lateral dose distribution very well (*cf* Fig. 6.10). The radiation-dependent heat generation rates in depth were taken from the measured *ddd* (*cf* Sec. 6.3.2.5), which was adequately fitted to generate a mathematical expression applicable within the calculation. Further, the time structure of the irradiation has been taken from Tab. 6.4 using a mean irradiation duration of 95 s for the complete scan and 32 ms for a single spot. Using these experimental input values, the resulting heat conduction correction factor, k_c, amounts to $1.0177 \pm 0.50\,\%$ with the given uncertainty comprising the following components: (I) Variations of the lateral dose distribution and time structure occurring from irradiation to irradiation as well as in between beamtimes are accounted for by performing calculus of variations using the measured fluctuation range. This component contributes to the total uncertainty with $\pm 0.3\,\%$. (II) Uncertainties of the applied convolution model especially with respect to complex raster pattern and the influence of the detector wall on close-by positioned raster spots are estimated with $\pm 0.3\,\%$. (III) Usually, the exact time evolution of the series of consecutive irradiations is considered in the heat transport calculations, as the superposition of the heat conduction effects of the previous irradiation with those of the actual irradiation leads to an individual pattern of the experimental results as a function of the number of irradiation [Krauss, 2006b]. This is, however, not realistic for the irradiation situation in scanned ion beams due to impracticable computation times. For the measurements performed within this thesis having a break of 3 min between two consecutive calorimetric measurements, a simplified comparison using the example of a static irradiation of 95 s duration with the lateral dose distribution taken from Fig. 6.8 has shown maximal differences between the irradiation specific k_c´s of $0.2\,\%$ for a series of 10 measurements. Thus, this uncertainty is considered in the overall uncertainty of the irradiation independent heat conduction correction factor. (IV) The uncertainty of the geometrical water calorimeter model as well as the thermal parameters used within the finite-element calculations is estimated with $\pm 0.1\,\%$.

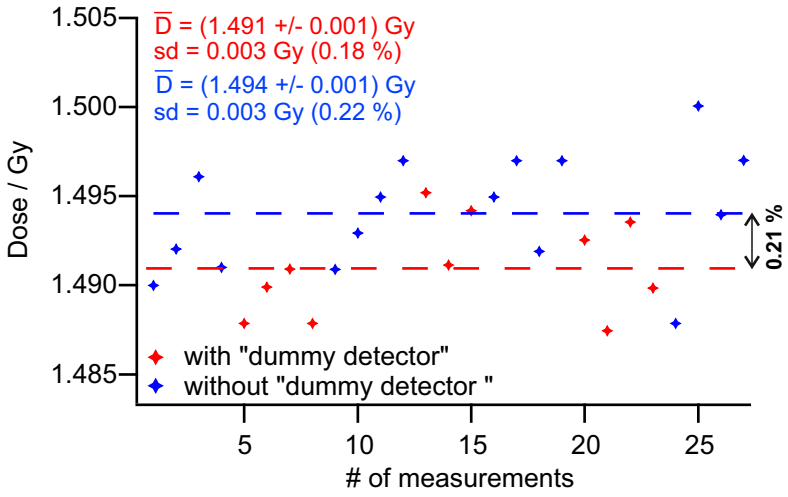

Fig. 6.19: *Measurements performed for the experimental determination of the radiation field pertubation correction factor k_p.*

6.4.1.3 Radiation field pertubation correction k_p

According to the procedure described in Sec. 4.1.2.3, k_p has been determined experimentally by using a 'dummy detector' in combination with the thimble ionization chamber TM30013 S/N 7659, which has been corrected for changes in the air density of the sensitive volume during the course of measurements. The chamber has been operated at 400 V and read-out using the UNIDOS electrometer by PTW (Freiburg, Germany). The measurements were performed at room temperature with the very same irradiation parameters and measurement position as used for the determination of D_w (*cf* Tab. 6.1). By turns, measurements have been performed with the ionization chamber placed inside the water phantom of the calorimeter with and without the surrounding glass cylinder. The distance of the ionization chamber with respect to the beam entrance window has been frequently checked during the course of measurements. In total, 16 (11) measurements were performed without (with) 'dummy detector' with the corresponding mean values given in the figure. As the relative standard deviations seen for both measurements with and without 'dummy detector' are in good agreement with the standard deviation of measurements seen during beam monitoring (*cf* Fig. 6.15), one can assume reliable and reproducible measurement conditions. Thus, k_p was determined as the ratio of the ionization chamber reading without and with the glass cylinder present to 1.0021 ± 0.0007. In addition, the radiation field pertubation factor has been verified via a FLUKA simulation comparing the dose deposition with and without presents of the glass cylinder at the measurement position of the thermistor probes. The simulated k_p-value amounts to 1.0014 ± 0.0010 and thus confirms the experimental result.
In addition to the given relative standard error of the mean (0.07 %), which includes the effects from small positioning variations of the ionization chamber during the course of measurements, a remaining systematic difference between real calorimetric and 'dummy detector' (*e.g.* absence of thermistor probes) is accounted for by an assumed uncertainty contribution of 0.2 % resulting in $k_p = 1.0021$ with an overall standard uncertainty of ± 0.21 %.

6.4.1.4 Correction for lateral measurement position k_l

As explained in Sec. 4.1.2.4, the value of D_w measured off-axis with each thermistor needs to be individually corrected to the dose deposited at the central axis in order to achieve com-

Thermistor	B-value	Horizontal position	k_l	$\Delta k_l / k_l$
E4	3199.93 K	+2.0 mm	1.0071	$\pm$ 0.44 %
E7	3103.10 K	+2.7 mm	1.0077	$\pm$ 0.36 %
E22	3224.30 K	-4.6 mm	1.0140	$\pm$ 0.33 %
E23	3140.94 K	-3.2 mm	1.0121	$\pm$ 0.34 %

Table 6.6: *Overview of the thermistor-specific k_l-factors used for the determination of D_w. The position of the thermistor probes inside the calorimetric detector, which are precisely known within less than $\pm$ 0.1 mm, are given in beam´s eye view (BEV) with respect to the central beam. Additionally, the thermistor-specific B-values needed for the calculation of ΔT are given. The thermistors E7 and E22 were used during the first and second beamtime, while another calorimetric detector comprising the thermistors E4 and E23 was applied during the third beamtime.*

parable conditions between the ionometric and calorimetric measurements. Two methods for the determination of the thermistor specific k_l-factors were applied here. The first method is based on the mean relative lateral dose distribution measured with STARCHECK with the corresponding horizontal profile shown in Fig. 6.8. As the lateral dose distribution is normalized to the central beam, k_l is given by the reciprocal of the interpolated relative dose at the individual thermistor position. The second approach is based on the calculated relative dose distribution using the adapted raster spot positions of MWPC1 as shown in Fig. 6.11 by also interpolating the corresponding data to the individual thermistor position. The differences seen between both methods are well below 0.2 % with the true thermistor-specific k_l-values taken to be the mean of both approaches as given in Tab. 6.6. The corresponding relative uncertainties result from the uncertainties of the mean lateral dose distribution measured with STARCHECK (*cf* caption of Fig. 6.8), while contributions from positioning uncertainties will be addressed separately in Sec. 6.6.

6.4.1.5 Correction for measurement position in depth k_d

As explained in Sec. 4.1.2.5, the water calorimetric measurements performed at 4 °C need to be comparable to the ionometric measurements carried out at 18 °C in order to accurately determine the corresponding k_Q-factor. Although the nominal measurement position was set to 50 mm, small deviations were seen in the frequently verified calorimetric and ionometric measurement positions. In addition to this effect, also the difference in density between water of 4 °C and 18 °C amounting to 1.00168 [Lemmon et al., 2005] needs to be accounted for as it influences the effective measurement depth. Considering the very small depth dose gradient of 0.023 %/mm at the nominal measurement position (*cf* Fig. 6.13), the differences between the calorimetric and ionometric measurement positions were found to be generally very small with the resulting beamtime- and ionization chamber- specific k_d-values being in the order of 0.999. Considering the uncertainties in the density of water [Wagner and Pruß, 2002] as well as the very small depth dose gradient, the relative standard uncertainty of the depth dose distribution correction factor $k_d = 0.999$ is estimated to be less than $\pm$ 0.01 %.

6.4.1.6 Correction for a change in the thermistor´s electrical power k_e

As the change in the thermistor´s electrical power during the course of a calorimetric measurement directly influences the temperature level of the thermistor and with that the mea-

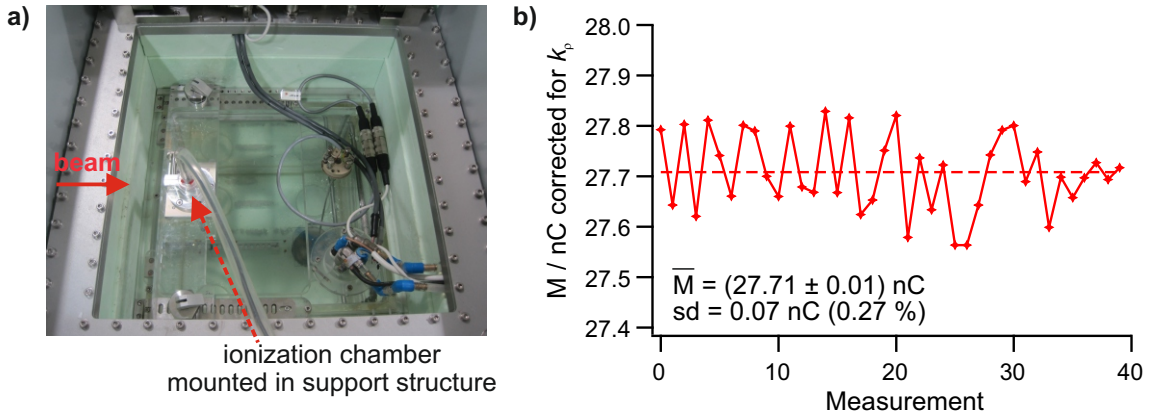

Fig. 6.20: *a) Experimental set-up for the calibration of the ionization chamber in terms of absorbed dose to water within the water phantom of the calorimeter. b) Typical ionometric measurement series consisting of 40 irradiations performed with the TM30013 S/N 7659 during the third beam time in Feb. 2015.*

surement of the radiation-induced temperature rise ΔT, the corresponding correction factor k_e needs to be applied in order to accurately determine D_w. As known from calibration (*cf* Sec. 4.1.1), the temperature level of the thermistors is raised by a factor of about $dT/dP = 1.2\,\mathrm{mK/\mu W}$ with respect to the surrounding water temperature. Considering this as well as the specific calorimetric measurement conditions and the voltage divider circuit used for the determination of R_{th} (*cf* Fig. 4.3), k_e accounts to 1.0004 with a relative standard uncertainty of $\pm\,0.01\,\%$ considering possible variations in the thermal coupling of dT/dP.

6.5 Ionometric measurements

Except for the first beamtime, where the ionometric and calorimetric measurements were delayed in time by about one week due to logistical reasons, the calibration of the Farmer-type ionization chambers FC65-G S/N 2978 and TM30013 S/N 7659 (*cf* Sec. 4.2) in terms of absorbed dose to water was performed directly after the calorimetric measurements had been finished and the water temperature in the phantom had been increased to 18 °C. In order to ensure comparable measurement conditions, the reference point of the ionization chamber was positioned at the same depth of water in the phantom of the calorimeter as the thermistor during the calorimetric measurements (Fig. 6.20 a and Fig. 3.1 b) and the very same irradiation parameters were used. According to the manufacturers' instructions, a fixed positive bias potential of + 300 V has been applied to the central electrode of the FC65-G and + 400 V to the chamber thimble of the TM30013. By using the ionometric measuring system developed by PTB, the ionization chamber charge as well as the water temperature inside the calorimeter phantom and the ambient air pressure have been recorded with a sample rate of 1 Hz allowing to continuously correct the ionization chamber reading for the influence of air temperature and pressure according to Eq. 4.7. The corresponding reference data used for calibration in ^{60}Co radiation are summarized in Tab. 4.2. Here, analogue to the analysis of the calorimetric measurement data (*cf* Sec. 6.4), the integral radiation-induced charged measured by the ionization chamber has been determined by extrapolating the linear fits of the pre- and post-irradiation drift curves to the mid-run position. In comparison, the background-corrected integral signal of the ionization chamber reading has been auto-

matically determined when the UNIDOS electrometer by PTW has been applied. In total, 90 (100) measurements have been performed with the TM30013 (FC65-G) over the course of all three ionometric beamtimes with a typical series of measurements exemplary shown in Fig. 6.20 b. The relative standard deviation of the measurement given in the figure is typical for all ionometric measurements performed within this thesis. Further, it is in good agreement with the relative standard deviation of measurements seen within the investigation of the long-term reproducibility of the irradiation conditions discussed in Sec. 6.3.2.6. As the final result of each ionometric beamtime, the radiation-induced charge measured with each ionization chamber has been corrected for the influence quantities given in the following section.

6.5.1 Determination of correction factors and their uncertainties

As described in Sec. 4.2.2, several correction factors are required for the ionometric measurements, which are separately addressed in the following.

6.5.1.1 Saturation correction k_s

According to the procedure described in Sec. 4.2.2.3, the saturation effect has been determined experimentally for both ionization chambers with the measured data and resulting Jaffé-diagrams shown in Fig. 6.21. The measurement conditions, *i.e.* irradiation parameters and measurement position, were not changed with respect to the ionometric measurements described in the previous section. By applying linear-quadratic fits to the data shown in the Jaffé-diagrams, the saturation correction factor, $k_{s,^{12}C}$, has been determined to $1.0022 \pm 0.22\,\%$ for the FC65-G chamber ($U_G = 300\,\mathrm{V}$) and $1.0023 \pm 0.22\,\%$ for the TM30013 chamber ($U_G = 400\,\mathrm{V}$) by means of Eq. 4.11. In addition to the uncertainty of the fit parameters, the total relative uncertainties given for k_s include an uncertainty contribution of the method itself, which is assumed to be in the order of $\pm 0.20\,\%$. This value results from calculus of variation where the number of data points in the Jaffé-diagram have been slightly varied and its impact on the resulting k_s-value studied.
As the $N_{D,w}$ calibration factors for ^{60}Co radiation for both ionization chambers are not corrected for the saturation effect under reference conditions, a modified correction factor according to Eq. 4.12 needs to be applied in order to adequately correct for the effect of incomplete saturation in the user beam quality ^{12}C. Using the $k_{s,^{60}Co}$-values given in Tab. 4.2 with the corresponding measurement uncertainties already included in the uncertainty of $N_{D,w}$, the final k_s-factors for the FC65-G and TM30013 chambers amount to $1.0012 \pm 0.22\,\%$ and $1.0013 \pm 0.22\,\%$, respectively.

6.5.1.2 Polarity correction k_{pol}

As the measurements for the determination of k_s have been performed at both polarities for each applied voltage, the polarity correction factor can be deduced from the data shown in Fig. 6.21 according to the procedure described in Sec. 4.2.2.2. Thus, $k_{pol,^{12}C}$ has been determined to $1.0012 \pm 0.07\,\%$ for the FC65-G chamber and $0.9993 \pm 0.07\,\%$ with respect to the TM30013 chamber. The total relative uncertainties given include the standard error of the performed measurements as well as a very small uncertainty contribution of the method itself estimated by 0.05 %, as, except for the polarity, nothing has been changed with respect

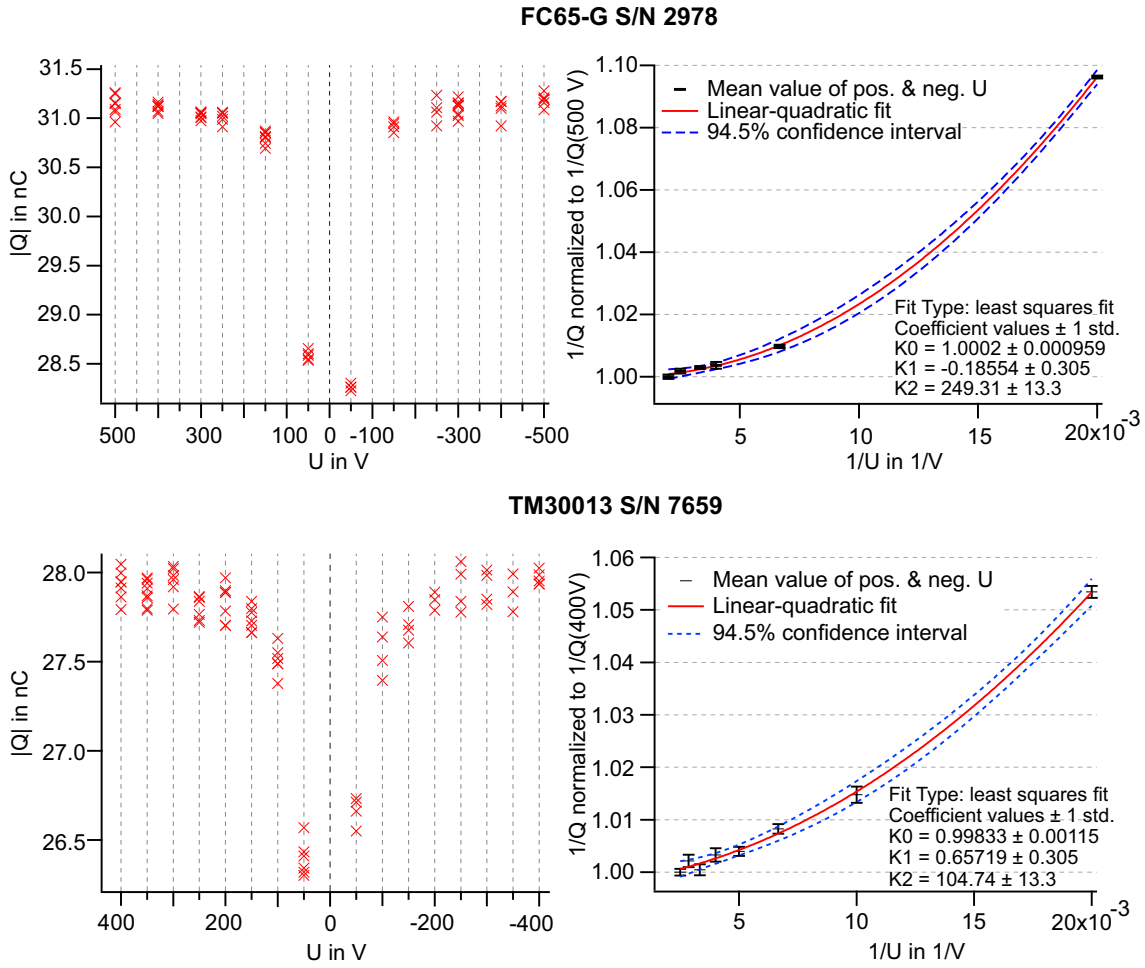

Fig. 6.21: *Measured data and resulting Jaffé-diagrams for the determination of the saturation correction factor in the user beam quality ^{12}C with the error bars referring to the standard errors of the repeated measurements with respect to U.*

to the experimental set-up during the determination of k_{pol}.
Analogue to the saturation effect, the calibration factors for ^{60}Co radiation for both ionization chambers are not corrected for the polarity effect under reference conditions. Thus, the final k_{pol}-values determined according to Eq. 4.9 amount to $1.0002 \pm 0.07\,\%$ and $1.0003 \pm 0.07\,\%$ for the FC65-G and TM30013 chambers, respectively. Again, the uncertainty of the $k_{pol,^{60}Co}$-values in Tab. 4.2 are already considered in $N_{D,w}$ and are therefore not included in the measurement uncertainties of k_{pol} given here.

6.5.1.3 Volume correction k_V

As described in Sec. 4.2.2.4, neither a standardized procedure for the determination of k_V with respect to carbon ion beams exists yet nor have corresponding spatial dose response functions of ionization chambers been determined for ^{12}C radiation. Therefore, a simplified approach has been used by numerically integrating the lateral dose distribution over the cross-sectional area of the ionization chamber perpendicular to the beam axis without considering the real cylindrical form of the Farmer-type ionization chambers. The volume correction factor has then been calculated as the ratio of the relative dose value at the posi-

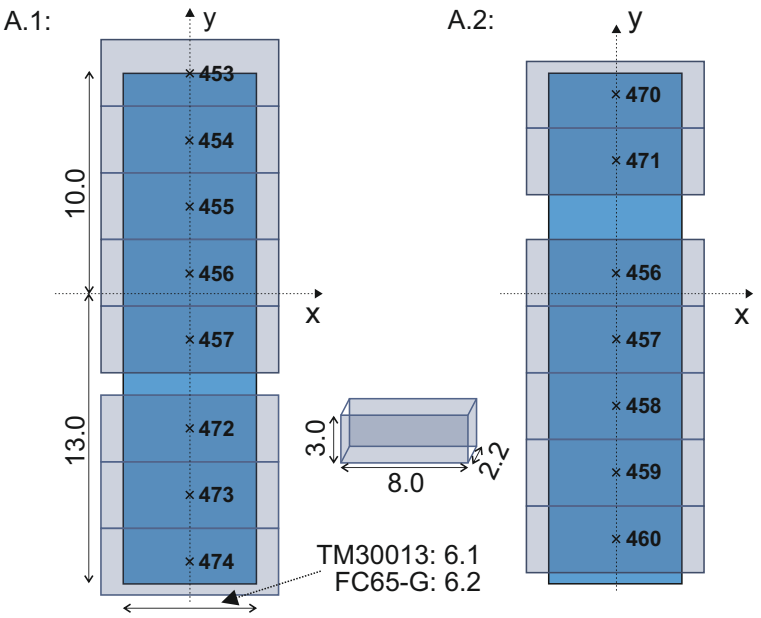

Fig. 6.22: *Considering the dimensions (given in mm) and the measurement positions of the individual ionization chambers within* STARCHECK*, the sensitive volume of the Farmer chambers (indicated by blue color) used for the determination of k_Q can be 'covered' with* STARCHECK *chambers (indicated by gray color). Here, two possibilities (A.1 and A.2) using different* STARCHECK *chambers (the IDs of the chambers are given in the figure) are shown, which cover the sensitive volume of the Farmer chambers the best, although small uncovered areas as well as exceeding parts are unavoidable.*

tion of the reference point of the chamber (located at the central axis) and the result of the 'integration', which is strictly seen not a real mathematical integration but more an adding up of relative dose values. Analog to the procedure described for the determination of the calorimetric correction factor k_l in Sec. 6.4.1.4, two methods were applied for the determination of k_V. The first method is based on the mean relative lateral dose distribution measured with STARCHECK with the corresponding vertical profile shown in Fig. 6.8. As explained in Sec. 6.3.2.4, the ionization chamber array has been repositioned multiple times during these measurements in order to increase the spatial resolution of the lateral dose profiles. Thus, considering the dimensions and the measurement positions of the individual ionization chambers within STARCHECK, the sensitive volume of the Farmer chambers can be 'covered' in two different ways (A.1 and A.2) as illustrated in Fig. 6.22. k_V has then been approximated by averaging the signal of corresponding STARCHECK chambers with the results of A.1 and A.2 agreeing within 0.02 %,.

The second approach is based on the calculated 2-dimensional dose distribution using the adapted raster spot positions derived from the measurements with the position regulating MWPC1 as shown in Fig. 6.11. In this case, the numerical integration was performed over the full cross-sectional area of the farmer chambers. The relative difference between both methods used for the approximation of k_V amounts to 0.4 % with the true value taken to be the mean of both approaches. Thus, the final k_V-value is given by $1.0129 \pm 0.26\,\%$ considering an uncertainty contribution from the mean lateral dose distribution measured with STARCHECK of 0.17 % (*cf* caption of Fig. 6.8) and the simplified method for the determination of k_V itself (0.20 %), while contributions from positioning uncertainties will be addressed separately in the following section.

6.6 Determination of k_Q and its uncertainties

The beam quality correction factor k_Q has been determined according to Eq. 3.3 with $N_{D,w}$ for both ionization chambers taken from Tab. 4.2. $N_{D,w,Q}$ has been calculated as the ratio of absorbed dose to water as determined by means of water calorimetry (*cf* Sec. 6.4) and the corresponding radiation-induced charge measured during the direct calibration of ionization chambers (*cf* Sec. 6.5) in the clinical carbon ion beam. The combined standard measurement uncertainty of the k_Q-factors is evaluated in accordance with the recommendations of the *Guide to the Expression of Uncertainty in Measurement* [Joint Committee for Guides in Metrology (JCGM/WG 1), 2008] and is composed of the uncertainty contributions from the calorimetrically determined $D_{w,Q}$, the ionometric measurement of M_Q, as well as the uncertainty of the calibration factor $N_{D,w}$. As the uncertainties for the specific heat capacity of water, for the heat defect (without the contribution of possible response variations of different detectors), and for a part of the uncertainty contributions to the calibration of the temperature probes are common in the case of both $N_{D,w}$ and $N_{D,w,Q}$, they will be omitted in the calculation of the overall standard measurement uncertainty of k_Q as discussed in detail in Krauss and Kapsch [2007]. Tab. 6.7 summarizes the complete uncertainty budget for the experimentally determined k_Q-factors with the uncertainty contributions stated in brackets indicating omitted uncertainty contributions. With respect to $N_{D,w}$, the standard measurement uncertainty of 0.25 % as stated in the calibration certificate therefore reduces to 0.20 % when omitting the named uncertainty contributions. As the uncertainties for the ionometric measurements performed with both ionization chambers are very similar and mean values have been used were necessary, the uncertainty budget is valid for the k_Q-factors determined with both ionization chambers. In addition to the uncertainties of the calorimetric and ionometric correction factors discussed before, the following additional contributions need to be considered:

Radiation-induced temperature rise, ΔT According to Eq. 4.3, ΔT results from the measured relative resistance change $\Delta R/R$ and the thermistor sensitivity S. The statistical uncertainty of a calorimetric measurement is given by 0.14 %, which is a typical standard error of a mean $\Delta R/R$ value obtained during a calorimetric experiment in the scanned carbon ion beam at HIT. This uncertainty is caused by the signal-to-noise ratio of the measurement system as well as by variations of the dose deposition occurring from irradiation to irradiation. In addition, calibration uncertainties of the voltage-divider system used for the measurement of R as well as uncertainties caused by the data analysis method are estimated with 0.05 % resulting in an overall uncertainty of $\Delta R/R$ of 0.15 %. Further, the total uncertainty of S is given by 0.07 % resulting from two sources: (I) 0.06 % are caused by the secondary standard thermometer including the corresponding reading device used for the calibration of the thermistor probes in terms of resistance change with temperature and (II) 0.03 % result from the calibration procedure itself [Krauss and Kapsch, 2007]. As the first source is common for all calibrations of the different thermistor probes used for the determination of both $N_{D,w}$ and $N_{D,w,Q}$, only the second contribution of 0.03 % has to be considered in the overall standard measurement uncertainty of k_Q.

Positioning of the thermistor probes While the positioning uncertainty in depth is already included in the uncertainty of k_d (cf Sec. 6.4.1.5), residual uncertainties with respect to the lateral thermistor position will be separately addressed here. Although

Quantity	Rel. standard uncertainty / %
Calorimetric measurements	
Radiation-induced temperature rise, ΔT	
Rel. resistance chance, $\Delta R/R$	0.15
Thermistor calibration, S	[0.06] 0.03
Specific heat capacity, c_p	[0.03]
Positioning of the thermistor probes	0.14
Heat conduction effects, k_c	0.50
Heat defect, k_h	[0.14] 0.10[a]
Lateral measurement position, k_l	0.36[b]
Radiation field pertubation correction, k_p	0.21
Change in thermistor´s electrical power, k_e	0.01
Measurement position in depth, k_d	0.01
Ionometric measurements	
Dosimeter reading	0.09
Polarity effect, k_{pol}	0.07
Ion recombination, k_s	0.22
Volume effect, k_V	0.26
Positioning of the ionization chamber	0.10
Calibration factor $N_{D,w}$	[0.15] 0.20[c]
Stability of $N_{D,w}$	0.05
Long-term reproducibility of the irradiation	0.30
Combined standard measurement uncertainty of k_Q	**0.82**

Table 6.7: *Combined standard measurement uncertainty budget for the calorimetric determination of k_Q in the scanned carbon ion beam at HIT with detailed radiation field specifications given in Sec. 6.3. Values stated in brackets indicate uncertainty contributions which are common for both $N_{D,w}$ and $N_{D,w,Q}$ and are therefore omitted in the overall standard measurement uncertainty of k_Q (see also text on page 75).* [a] *A residual uncertainty contribution of 0.10 % remains for the calorimetric determination of $D_{w,Q}$ considering possible response variations of the different calorimetric detectors measured with ^{60}Co-radiation (cf Sec. 6.4.1.1 and text on page 75).* [b] *Mean uncertainty of the thermistor specific k_l-values stated in Tab. 6.6.* [c] *The standard measurement uncertainty of the calibration factor contains the uncertainty of the pertubation and saturation effect of the ionization chamber at ^{60}Co radiation. Therefore, these contributions are not considered in the stated uncertainties of k_s and k_{pol}.*

the position of the thermistor probes inside the calorimetric detector is precisely known within an uncertainty of less than ± 0.1 mm, lateral positioning uncertainties of the water calorimeter due to the finite line width of the adjusting laser system can cause deviating measurement positions of the thermistor probes. In order to estimate this uncertainty contribution, the lateral measurement position of the thermistor probes is assumed to vary within ± 1 mm. Considering the mean lateral dose distribution measured with STARCHECK (Fig. 6.8), the standard measurement uncertainty of this effect can be estimated with 0.14 %.

Dosimeter reading The statistical uncertainty of an ionometric measurement is given by 0.05 %, which is a typical standard error of a mean radiation-induced charge value obtained during an ionometric experiment in the scanned carbon ion beam at HIT independent of the ionization chamber used. This uncertainty is caused by the signal-to-noise ratio of the read-out system as well as by variations of the dose deposition occurring from irradiation to irradiation. Further, an uncertainty contribution of 0.07 % is considered taking into account uncertainties due to the electrometer calibration, the leakage current, the measurement of the air pressure and the temperature in the chamber cavity, the humidity, as well as the incomplete stabilization of the ionization current. Thus, the overall uncertainty concerning the dosimeter reading amounts to 0.09 %.

Positioning of the ionization chamber Considering the very small depth dose gradient at the measurement position of the ionization chamber as well as almost negligible positioning variations of the ionization chamber in depth measured before and after a calibration, the positioning uncertainty in depth can be neglected. Analogue to the lateral positioning uncertainty of the thermistor probes, the measurement position of the ionization chamber is assumed to vary within ± 1 mm in both horizontal and vertical direction. Considering the mean lateral dose distribution measured with STARCHECK (Fig. 6.8) as well as the averaging effect of the ionization chamber due to its finite volume, the mean standard uncertainty of this effect can be estimated with 0.10 %.

Long-term reproducibility of the irradiation Usually, a calorimetric/ionometric beamtime for the determination of k_Q consisted of three consecutive night shifts with the calorimetric measurements performed during the first two nights and the corresponding ionometric measurements carried out during the third night. Thus, variations in the dose deposition due to the beam delivery system occurring between the calorimetric and ionometric measurements directly influence the resulting k_Q-factor. In order to investigate this effect, the long-term reproducibility of the irradiation has been monitored over a period of 7 months covering the course of all three ionometric/calorimetric beamtimes as shown in Fig. 6.15 revealing maximal variations in the order of 0.5 %. As these major variations did not occur between calorimetric and inometric measurements belonging to the same beamtime, it is more realistic to estimate the uncertainty of this effect by the relative standard deviation of all measurements given by 0.3 %.

The resulting k_Q-factors determined for each ionization chamber per calorimetric/ionometric beamtime are shown in Fig. 6.23 agreeing well within the given uncertainties. The final k_Q-factor per ionization chamber is taken to be the mean value of the three experimentally determined values with an overall standard measurement uncertainty of 0.8 %. As the displacement effect is accounted for differently in TRS-398 and DIN 6801-1 (*cf* Sec. 3.2), it is important to note that this experimentally determined k_Q-factor, which will be referred to as k_Q^{cal} in the following, is not directly comparable with the k_Q-factors stated in the dosimetry protocols. Thus, in order to compare the experimentally determined k_Q-factors with the corresponding literature values, k_Q^{cal} has to be transformed into k_Q^{DIN} (Eq. 3.12) and k_Q^{TRS} (Eq. 3.13), respectively, using the experimentally determined value of $\delta_{^{12}C} = -0.023\,\%/mm$ (*cf* Sec. 6.3.2.5) for the relative depth dose gradient at z_{ref} in the carbon ion field used for calibration. The resulting k_Q-values are summarized in Tab. 6.8 and will be discussed with

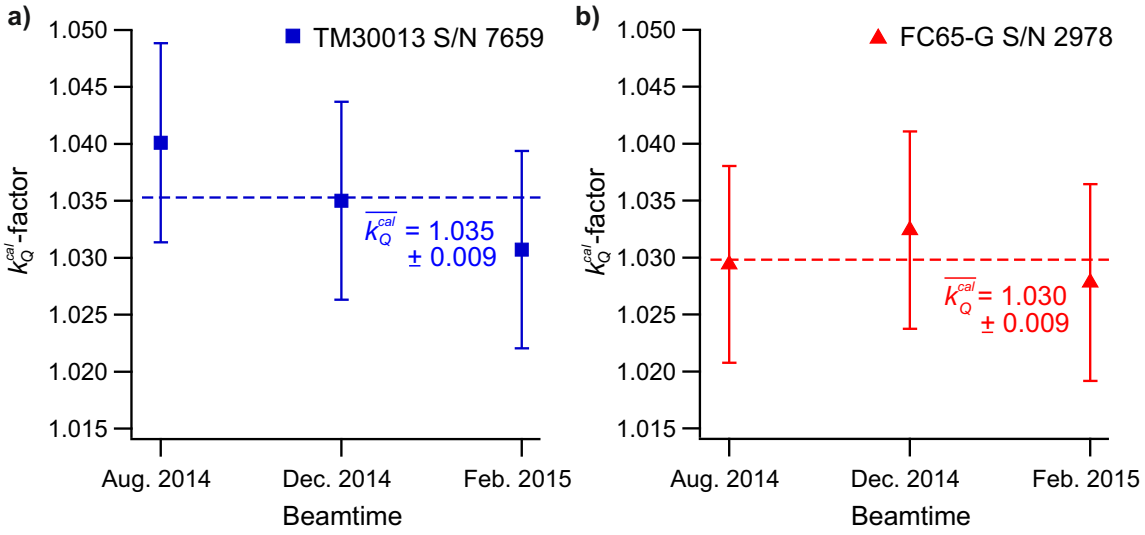

Fig. 6.23: *Experimentally determined k_Q^{cal}-factors for carbon ion beams. Please note that the mean k_Q^{cal}-values given in the figure need to be transformed into k_Q^{DIN} (Eq. 3.12) and k_Q^{TRS} (Eq. 3.13), respectively, in order to be used for the reference dosimetry of ion beams according to DIN 6801-1 and TRS-398.*

respect to the literature values in the following section.

6.7 Discussion

As a main result it was demonstrated for the first time that the experimental determination of the k_Q-factor for scanned clinical carbon ion beams by means of water calorimetry is achievable with a relative standard measurement uncertainty of 0.8 %. This corresponds to a threefold reduction of the uncertainty compared to calculated values and therefore enables to significantly decrease the overall uncertainty related to ionization-based dosimetry of clinical carbon ion beams. Besides precise calorimetric and ionometric measurements, this uncertainty could only be reached by a thorough choice of irradiation parameters as elaborated in Sec. 6.2. Moreover, a detailed characterization and monitoring of the irradiation field over the course of the successively performed three calorimetric/ionometric beamtimes (*cf* Sec. 6.3.2) has shown to be essential for the accurate determination of corresponding correction factors with low uncertainty (Sec. 6.4.1 and Sec. 6.5.1). In order to ensure that the field characterization measurements reflect the real experimental set-up used for the determination of k_Q at the best, a water-equivalent slab phantom has been developed mimicking the water calorimeter as discussed in Sec. 6.3.1. This ensures that the variety of measurements performed with all kind of detectors refer to the effective measurement position of the water calorimeter.

In excess of the precise knowledge of the lateral and depth dose distribution needed for the determination of k_l, k_V, k_d, and k_c, accurate determination of the spatial irradiation pattern, *i.e.* the position of each irradiated raster spot, the exact size and shape of the carbon ion pencil beam, and the temporal irradiation structure, were essential experimental parameters in order to accurately reproduce the real calorimetric measurement condition within the finite-element heat conduction calculations for the determination of k_c.

Thereby, one major challenge was to find a detector enabling precise measurements of the lateral dose distribution with high spatial resolution and reproducibility while at the same time offering a low measurement uncertainty. Comparing the different types of detectors available with respect to this specific ion-beam application, the ionization chamber array STARCHECK was found to offer the best trade-off between the desired properties. As the uncertainty of the array and with that of the measured lateral dose distribution have significant impact on the determination of corresponding correction factors and thus the overall measurement uncertainty of the resulting k_Q-factor, the detector array has been investigated in the well-defined ^{60}Co irradiation field at PTB prior to its application in the carbon ion beam at HIT. Via an extensive calibration procedure described in Sec. 6.3.2.4, a reduction of the calibration uncertainty from $\pm\,1\,\%$ as determined by the manufacturer to $\pm\,0.3\,\%$ could be achieved and a reproducibility of $\leq 0.1\,\%$ shown.

Although the irradiation parameters were carefully chosen to generate a preferably homogenous irradiation field, the frequently repeated STARCHECK measurements revealed reproducible maximal differences of 3 % between the central beam and the marginal regions ($\pm\,20\,$mm) of the measured relative dose profiles already within the central area of the irradiation field (*cf* Sec. 6.3.2.4). In this context it was intriguing to see that these large deviations could not be explained by the spatial irradiation pattern as derived from the measurements with the position-regulating MWPC1, nor by the number of particles delivered to each raster spot as determined by the particle-number regulating IC1, which are recorded for each irradiation within the machine beam records. Further measurements and theoretical investigations strongly indicate that the discrepancy between measured and calculated dose profiles is most likely due to slightly misplaced single wires within the MWPC1 resulting in defective raster spot positions. However, this hypothesis has not been verified experimentally as the clear separation of this effect from others is challenging. As the position of each irradiated raster spot is, besides others, an essential experimental information for the determination of k_c, the experimental verification of this hypothesis is highly desirable for future measurements.

The long-term reproducibility of the beam delivery system in the QA-room at HIT has been monitored over a time period of about 7 months covering the course of all calorimetric and ionometric measurements performed for the determination of k_Q. As a main result it could be shown that the beam delivery system in combination with the irradiation plan used allow for very reproducible measurement conditions with a relative standard deviation of only $\pm\,0.3\,\%$ (*cf* Sec. 6.3.2.6). As this result proves stable measurement conditions over time, k_Q could be determined with low measurement uncertainty although the corresponding calorimetric/ionometric measurements had to be carried out over the course of three beamtimes due to time constraints.

From the first part of this thesis dealing with the comparison of fluence- and ionization-based dosimetry it was found that, even in the entrance channel of a high-energy carbon ion beam, the primary particle beam is already significantly contaminated by fragments having a non-negligible contribution to the total deposited dose. Therefore, in order to determine the particle spectrum and the contribution of primary and secondary particles to the total deposited dose at the measurement position of the water calorimeter and thus characterize the particle spectrum corresponding to the experimentally determined k_Q-factor, extensive MC simulations have been performed. In order to reproduce the experimental set-up as

	TM30013 #7659			FC65-G #2978		
	Literature	Calorimetry	$\Delta/\%$	Literature	Calorimetry	$\Delta/\%$
DIN	$1.014 \pm 2.2\,\%$	$1.026 \pm 0.8\,\%$	-1.2	$1.012 \pm 2.2\,\%$	$1.021 \pm 0.8\,\%$	-0.9
TRS	$1.032 \pm 2.8\,\%$	$1.036 \pm 0.8\,\%$	-0.4	$1.042 \pm 2.8\,\%$	$1.030 \pm 0.8\,\%$	+1.1

Table 6.8: *Comparison of the calculated k_Q-values for ion beams as stated in TRS-398 and DIN 6801-1 (draft) with the experimental k_Q-factors determined by means of water calorimetry in the clinical carbon ion beam at HIT.*

accurate as possible, the inhomogeneous nature of styrofoam as well as appropriate phase-space files provided by HIT have been carefully considered in the simulations. As shown in Fig. 6.17 and discussed in the corresponding section, primary carbon ions with a median LET of 11.3 keV/µm (corresponding to a kinetic energy of about 368 MeV/u) deposit 85 % of the total dose, while their contribution to the total number of particles only amounts to 39 % being dominated by protons, deuterons, and tritons with a fraction of 48 %. However, due to their low-LET of about 0.4 keV/µm representing the lowest limit of the LET spectrum, their contribution to the total deposited dose is only 8 %. The remaining 7 % of the deposited dose is mainly from Helium ions, while the contribution of particles with Z = 3 to 5 is very small. Strictly seen, the experimentally determined k_Q-factor is only valid for this specific particle spectrum. However, as both TRS-398 and DIN 6801-1 assume a constant k_Q-factor for all ions with $2 \geq Z \leq 18$ (TRS-398) and $2 \geq Z \leq 10$ (DIN 6801-1) and use similar conditions within their calculations, it can be concluded that the experimentally determined k_Q-factor is comparable with the literature values stated in both protocols.

Table 6.8 compares the calculated k_Q-values for ion beams as stated in TRS-398 and DIN 6801-1 (draft) with the corresponding experimental k_Q-factors determined by means of water calorimetry in the clinical carbon ion beam at HIT for both ionization chambers used. With respect to k_Q^{DIN}, the experimentally determined values for both chambers having a similar design (*cf* Tab. 4.1) are about 1 % larger than the calculated ones. However, the same tendency is not observable with respect to k_Q^{TRS} - while the experimentally determined k_Q^{TRS}-value is about 1 % lower than the corresponding literature value stated in TRS-398 regarding the FC65-G chamber, a deviation of 0.4 % in the opposite direction is shown in case of the TM30013 chamber. At this point it should be noted that the k_Q-factor of the FC65-G chamber has been added retrospectively to version V.12 of TRS-398, which has been published in June, 2006. In this version it is stated that the FC65-G chamber fails to meet some of the minimum requirements given in Sec. 4.2.1 of TRS-398 and has only been added because of its clinical use. While the k_Q-values for both chambers given in DIN 6801-1 only differ by 0.2 %, the corresponding k_Q-factors stated in TRS-398 differ significantly by about 1 % due to the usage of different values for $(p_{wall})_{Co}$. However, as the k_Q-factor has only been determined for two ionization chambers within this thesis, a clear statement with respect to the literature values is not possible at this time.

Chapter 7

Conclusion and Outlook

Reference dosimetry with air-filled ionization chambers calibrated in terms of absorbed dose to water in a ^{60}Co gamma ray reference beam is the current gold standard for the dosimetry of clinical carbon ion beams. However, although treatment with carbon ion radiotherapy already started more than 20 years ago with more than 15000 patients treated in one of the 10 facilities being in clinical operation up to now ([PTCOG, 2016], [Jermann, 2015]), no primary standard for absorbed dose to water for carbon ion beams exists so far. Consequently, all values for the beam quality correction factor, k_Q, given in TRS-398 [IAEA, 2000] and DIN 6801-1 [DIN, 2016] for ion beams are derived by calculations being the main source of uncertainties in the dosimetry of carbon ion beams with ionization chambers calibrated in ^{60}Co radiation (*cf* Tab. 3.1).

Within this thesis, it could be shown for the first time that the experimental determination of the k_Q-factor for carbon ion beams by means of water calorimetry is achievable with a relative standard measurement uncertainty of 0.8 % via a thorough calibration procedure reducing the uncertainty of currently used calculated values by a factor of about three. Thus, this result shows the potential of experimentally determined k_Q-factors to significantly decrease the overall standard measurement uncertainty in the dosimetry of clinical carbon ion beams. In addition, the increased accuracy of the experimentally determined k_Q-factor might open the possibility to gain further insight and to potentially reduce the uncertainties of individual components of the calculated k_Q-factor for ion beams (*cf* Sec. 3.1), such as the $(W_{air})_Q$-value or the stopping-power-ratio $(s_{w,air})_Q$, which - up to now - dominate the overall uncertainty of the calculated k_Q-factor. Assuming recommended DIN 6801-1 values and corresponding uncertainties of the water-to-air stopping power ratios, the perturbation factors, as well as $W_{air,Co}$ (*cf* Tab. 3.1), a mean W_{air}/e-value of (34.90 ± 0.64) J/C (± 1.8 %) results for the carbon ion beam used within this study using the experimentally determined k_Q^{DIN}-factors for both ionization chambers (*cf* Tab. 6.8). This value is about 1.2 % larger than the corresponding value of (34.50 ± 0.52) J/C (± 1.5 %) stated in both DIN 6801-1 and TRS-398. In comparison, Sakama et al. [2009] found a mean value of (35.72 ± 0.54) J/C (± 1.5 %) for carbon ion beams having an initial energy between 135 MeV/u and 430 MeV/u by means of graphite calorimetry, which is about 3.5 % larger than the literature value. Preliminary results obtained by Rossomme et al. [2014] in an 80 MeV/u carbon ion beam also by means of graphite calorimetry indicate an W_{air}/e-value of (35.50 ± 0.90) J/C (± 2.5 %) and are thus in good agreement with the mean value found by Sakama et al. [2009]. As a future project it is contemplated to perform a direct comparison of water and graphite calorimetry in the

scanned carbon ion beam at HIT. As graphite calorimetry is commonly used as a primary standard for absorbed dose to water in many standard laboratories worldwide [Seuntjens and Duane, 2009], the direct comparison of two independent primary standards is of fundamental interest from a metrological point of view. Additionally, it would allow to gain further insight into the conversion of dose to graphite as primarily measured by the graphite calorimeter into dose to water as directly measured by the water calorimeter.

From the detailed investigation of uncertainties related to the experimentally determined k_Q-factor summarized in Tab. 6.7 it can be deduced that correction factors depending on the lateral dose distribution of the irradiation field (k_V, k_l, k_c) dominate the total measurement uncertainty. Although the irradiation field used for the determination of k_Q has been optimized with respect to homogeneity, measurements revealed maximal dose differences of 3 % already within the central area of the irradiation field. As a consequence from this finding one can conclude that accurate knowledge of the lateral dose distribution is essential in order to determine the corresponding calorimetric and ionometric correction factors with sufficient accuracy as the simple assumption of a homogeneous dose distribution as predicted by the irradiation plan would lead to severe mistakes. This result also allows to reason that the total standard measurement uncertainty of the experimentally determined k_Q-factor for carbon ion beams can potentially be further decreased by using a more advanced two-dimensional dosimetry device in order to determine the lateral dose distribution with higher accuracy and spatial resolution compared to STARCHECK. A second, more general conclusion from this finding is that the volume effect of ionization chambers with respect to ion beams, which is up to now not explicitly taken into account in TRS-398 and DIN 6801-1, should not be neglected since especially scanned ion beams tend to exhibit intrinsic inhomogeneities with partly significant dose gradients. This is for example shown for the ionometric measurements performed for the determination of k_Q, where the corresponding volume correction factor k_V, although determined by a simplified approach, already accounts for about 1.5 %. If k_V would have been assumed to be unity, the determined k_Q-factors would have been mistaken by about 1.5 %. At the same time, one can deduce that - although the experimentally determined k_Q-factor enables a significant reduction of the overall standard measurement uncertainty in the dosimetry of clinical carbon ion beams - one can still be mistaken by 1.5 % or even more, if the lateral dose distribution is not sufficiently known or just assumed to be flat. This could easily happen when applying the homogeneity criterion given in DIN 6801-1, which classifies an ion field as sufficiently homogenous if the relative variance of the dose, $s_{D,rel}$, determined over the area of the irradiation field is below 3 % [DIN, 2016]. To put this number in perspective, $s_{D,rel}$ amounts to less than 1 % for the irradiation field used within this study for the experimental determination of k_Q (*cf* Fig. 6.11), where k_V has been found to already account for 1.5 %. Thus, analogue to the recent developments in conventional radiation therapy, high-accuracy determination of absorbed dose to water - being a point-like quantity - in carbon ion beams requires to consider this effect by an appropriate volume effect correction factor, k_V. Therefore, the investigation of spatial dose response functions of ionization chambers with respect to carbon ion beams and with that a sound determination of k_V would be highly desirable in order to converge to the same level of dosimetric accuracy as of conventional high-energy photon beams.

However, the experimentally determined k_Q-factor for carbon ion beams does not explain the discrepancy of 4.5 % between fluence-based dosimetry using FNTDs and ionization-

based measurements of absorbed dose to water performed in the clinical carbon ion beam at HIT within the first part of this thesis. Although the k_Q-factor has not been determined for the specific ionization chamber (TM30013 S/N 1714) used within the comparison study, the same type of ionization chamber has been calibrated directly in the carbon ion beam by means of water calorimetry. From k_Q determinations in high-energy photon radiation at PTB it is known that differences of the k_Q-factor between ionization chambers of the same type are generally below 0.3 % [Kapsch and Pychlau, 2008]. If it is assumed that this value is also valid in the case of other types of radiation, the experimentally determined k_Q-factor of $1.036 \pm 0.8\,\%$ for the Farmer-type ionization chamber TM30013 S/N 7659 rather points to an even larger discrepancy of about 4.9 % than explaining the 4.5 % discrepancy seen in the measurements. However, conclusions drawn from the detailed irradiation field characterization measurements performed during the experimental determination of k_Q are retrospectively seen of major relevance for the measurements performed within the first part of this thesis and might explain parts of the discrepancy between fluence- and ionization-based dosimetry: (I) As discussed before, significant inhomogeneities of the lateral dose distribution of up to 3 % measured by means of STARCHECK over the course of all three beamtimes could not be explained by the calculated dose distribution derived by the machine beam records (MBRs), which in contrast indicate an almost homogenous irradiation field for all performed irradiations. This led to the conclusion that calculated dose distributions derived by means of the MBRs do not, as assumed before, accurately reflect the homogeneity of the irradiation field. As the assessment of the irradiation field homogeneity within the comparison study of fluence- and ionization-base dosimetry mainly based upon the information derived by the MBRs, the assumption of a homogenous irradiation field can not be regarded reliable anymore. Taking into account the significant difference of the FNTD and ionization chamber detection area, unrecognized inhomogeneities of the lateral dose distribution could have had a major impact on the measurement results. (II) Further it has been concluded that, especially in scanned ion beams, the volume effect of ionization chambers can have a significant contribution and should therefore be accounted for. As k_V has not been considered during the comparison study, this effect might also contribute to the observed overall discrepancy. However, retrospectively it is not possible anymore to clearly prove these assumptions. Thus, in order to thoroughly investigate the discrepancy determined between fluence- and ionization-based dosimetry, the performed measurement should be repeated and accomplished with a detailed characterization of the irradiation field in order to accurately consider the effects named above. In addition, as the FNTD fluorescent track amplitude depends on the particle species and energy ([Sykora et al., 2008b], [Niklas et al., 2013], [Greilich et al., 2013]), the effective stopping-power might be estimated directly from the intensity histogram of the particle tracks using improved read-out protocols thus being independent of possible uncertainties related to MC transport simulations of the particle spectrum.

As an outlook of this thesis, it would be highly desirable to extend the experimental determination of the k_Q-factor by means of water calorimetry to further ionization chambers, energies, and different particle species (*e.g.* p, He, O being available at HIT) taking advantage of the unique measurement opportunities at HIT. Even more conclusive results with respect to the comparison with calculated k_Q-values stated in literature as well as the possibility to investigate a potential energy/LET dependency of the k_Q-factor are expected from these additional measurements.

Bibliography

Abràmoff, M. D., Magalhães, P. J., & Ram, S. J. (2004). Image processing with ImageJ. *Biophotonics Int.*, 11(7):36–43.

Akselrod, M. S., Akselrod, A. E., Orlov, S. S., Sanyal, S., & Underwood, T. H. (2003). Fluorescent aluminum oxide crystals for volumetric optical data storage and imaging applications. *J. Fluoresc.*, 13(6):503–511.

Akselrod, M. S. & Sykora, G. J. (2011). Fluorescent nuclear track detector technology - A new way to do passive solid state dosimetry. *Radiat. Meas.*, 46:1671–1679.

Alfonso, R., Andreo, P., Capote, R., Saiful Huq, M., Kilby, W., Kjäll, P., Mackie, T. R., Palmans, H., Rosser, K., Seuntjens, J., Ullrich, W., & Vatnitsky, S. (2008). A new formalism for reference dosimetry of small and nonstandard fields. *Med. Phys.*, 35(11):5179–5186.

Andreo, P., Nahum, A., & Brahme, A. (1986). Chamber-dependent wall correction factors in dosimetry. *Phys. Med. Biol.*, 31(11):1189–99.

Barkas, W. H. & Evans, D. A. (1963). *Nuclear Research Emulsions: Techniques and theory*. Pure and applied physics. Academic Press.

Bethe, H. (1930). Zur Theorie des Durchgangs schneller Korpuskularstrahlen durch Materie. *Ann. Phys.*, 397(3):325–400.

BIPM (1985). *Effect of a change of stopping-power values on the W values recommended by ICRU for electrons in dry air (CCEMRI(I)/85-8)*. Comite consultatif des les etalons de mesure des rayonnements ionisants (section I), Bureau International des Poids et Measures.

Bloch, F. (1933). Zur Bremsung rasch bewegter Teilchen beim Durchgang durch Materie. *Ann. Phys.*, 16(5):285–320.

Böhlen, T. T., Cerutti, F., Chin, M. P. W., Fassò, A., Ferrari, A., Ortega, P. G., Mairani, A., Sala, P. R., Smirnov, G., & Vlachoudis, V. (2014). The FLUKA code: Developments and challenges for high energy and medical applications. *Nucl. Data Sheets*, 120:211–214.

Boutillon, M. & Perroche-Roux, A. M. (1987). Re-evaluation of the W value for electrons in dry air. *Phys. Med. Biol.*, 32(2):213–219.

Bragg, W. H. & Kleeman, R. (1905). On the alpha particles of radium and their loss of range in passing through various atoms and molecules. *Phil. Mag.*, 10:318–340.

Butler, D. J., Stevenson, A. W., Wright, T. E., Harty, P. D., Lehmann, J., Livingstone, J., & Crosbie, J. C. (2015). High spatial resolution dosimetric response maps for radiotherapy ionization chambers measured using kilovoltage synchrotron radiation. *Phys. Med. Biol.*, 60:8625–8641.

Cardinale, J. (2010). Histogram-based background subtractor for imagej. Technical report, MOSAIC Group, ETH Zurich, available at http://mosaic.mpi-cbg.de/Downloads/BGS_manual.pdf, accessed February 15, 2016.

Combs, S. E., Jäkel, O., Haberer, T., & Debus, J. (2010). Particle therapy at the Heidelberg Ion Therapy Center (HIT) - Integrated research-driven university-hospital-based radiation oncology service in Heidelberg, Germany. *Radiother. Oncol.*, 95(1):41–44.

Debus, J. (2009). Particle therapy - Physical, technical and clinical aspects. *Eur. J. Cancer*, 45:381–382.

Derikum, K. (2003). Correction for ion recombination effects in ionization chambers consistently in continuous and pulsed radiation (IAEA-CN-96/30). In: *Stand. Codes Pract. Med. Radiat. Dosim.*, volume 1, pages 353–359. International Atomic Energy Agency.

DIN (2014). *DIN 6809-8:2014-03: Klinische Dosimetrie - Teil 8: Dosimetrie kleiner Photonen-Bestrahlungsfelder (Entwurf)*. Deutsches Institut für Normung e.V. Berlin, Germany.

DIN (2016). *DIN 6801-1: Dosismessverfahren nach der Sondenmethode für Protonen- und Ionenstrahlung - Teil 1: Ionisationskammern (Entwurf vom Januar 2016)*. Deutsches Institut für Normung e.V. Berlin, Germany.

Durante, M. & Loeffler, J. S. (2010). Charged particles in radiation oncology. *Nat. Rev. Clin. Oncol.*, 7(1):37–43.

Fano, U. (1963). Penetration of protons, alpha particles, and mesons. *Annu. Rev. Nucl. Sci.*, 13:1–66.

Ferrari, A., Sala, P. R., Fasso, A., & Ranft, J. (2005). Fluka: A multi-particle transport code. *Cern. INFN/TC_05/11, SLAC-R-773,* available at http://www.slac.stanford.edu/cgi-wrap/getdoc/slac-r-773.pdf, accessed February 15, 2016.

Giesen, U. & Beck, J. (2014). New measurements of W-values for protons and alpha particles. *Radiat. Prot. Dosimetry*, 161(1-4):23–26.

Greilich, S., Grzanka, L., Bassler, N., Andersen, C. E., & Jäkel, O. (2010). Amorphous track models : A numerical comparison study. *Radiat. Meas.*, 45(10):1406–1409.

Greilich, S., Osinga, J.-M., Niklas, M., Lauer, F. M., Klimpki, G., Bestvater, F., Bartz, J. A., Akselrod, M. S., & Jäkel, O. (2013). Fluorescent nuclear track detectors as a tool for ion-beam therapy research. *Radiat. Meas.*, 56:267–272.

Gunzert-Marx, K., Iwase, H., Schardt, D., & Simon, R. S. (2008). Secondary beam fragments produced by 200 MeV u^{-1} ^{12}C ions in water and their dose contributions in carbon ion radiotherapy. *New J. Phys.*, 10.

Haberer, T., Becher, W., Schardt, D., & Kraft, G. (1993). Magnetic scanning system for heavy ion therapy. *Nucl. Instruments Methods Phys. Res. Sect. A Accel. Spectrometers, Detect. Assoc. Equip.*, 330:296–305.

Hartmann, G. H., Brede, H. J., Fukumara, A., Hecker, O., Hiraoka, T., Jakob, C., Jäkel, O., Krießbach, A., & Schardt, D. (1997). Results of a small scale dosimetry comparison with carbon-12 ions at GSI Darmstadt. In: *Proc. Int. Week Hadron. 2nd Int. Symp. Hadron.*, pages 346–350. Elsevier.

Hartmann, G. H., Jäkel, O., Heeg, P., Karger, C. P., & Krießbach, A. (1999). Determination of water absorbed dose in a carbon ion beam using thimble ionization chambers. *Phys. Med. Biol.*, 44(5):1193–1206.

Highland, V. L. (1975). Some practical remarks on multiple scattering. *Nucl. Instrum. Methods Phys. Res.*, 129:497–499 and Erratum (1979), *Nucl. Instrum. Methods Phys. Res.*, 161:171.

Hiraoka, T. & Bichsel, H. (1995). Stopping powers and ranges for heavy ions. *Japanese J. Med. Phys.*, 15:91–100.

Hünemohr, N. (2014). *Dual energy CT as an alternative for ion radiotherapy treatment planning*. Phd thesis, Ruperto-Carola University of Heidelberg.

IAEA (2000). *TRS-398: Dose determination in external beam radiotherapy: An international code of practice for dosimetry based on absorbed dose to water*. International Atomic Energy Agency.

IBA (2013). *IBA FC65-G User's Guide*. IBA Dosimetry GmbH, Schwarzenbruck, Germany.

ICRU (1984). *Report No. 37: Stopping powers for electrons and positrons*. International Commission on Radiation Units and Measurements.

ICRU (1993). *Report No. 49: Stopping powers and ranges for protons and alpha particles*. International Commission on Radiation Units and Measurements.

ICRU (1998). *Report No. 60: Fundamental quantities and units for ionizing radiation*. International Commision on Radiation Units and Measurements.

ICRU (2005). *Report No. 73: Stopping of ions heavier than helium*. International Commission on Radiation Units and Measurements.

Jäkel, O., Jacob, C., Schardt, D., Karger, C. P., & Hartmann, G. H. (2001). Relation between carbon ion ranges and x-ray CT numbers. *Med. Phys.*, 28(4):701–703.

Jermann, M. (2015). Particle therapy statistics in 2014. *Int. J. Part. Ther.*, 2(1):50–54.

Joint Committee for Guides in Metrology (JCGM/WG 1) (2008). Evaluation of measurement data: Guide to the expression of uncertainty in measurement.

Kapsch, R.-P. & Pychlau, C. (2008). Exemplarstreuung von k_Q-Werten. In: *Proc. 39. Jahrestagung der Deutschen Gesellschaft für Medizinische Physik (DGMP)*.

Karger, C. P. & Jäkel, O. (2007). Current status and new developments in ion therapy. *Strahlentherapie und Onkol.*, 183:295–300.

Karger, C. P., Jäkel, O., Palmans, H., & Kanai, T. (2010). Dosimetry for ion beam radiotherapy. *Phys. Med. Biol.*, 55:R193–R234.

Ketelhut, S. & Kapsch, R.-P. (2015). Measurement of spatial response functions of dosimetric detectors. *Phys. Med. Biol.*, 60:6177–6194.

Klassen, N. V. & Ross, C. K. (1997). Water Calorimetry : The Heat Defect. *J. Reseach Natl. Inst. Stand. Technol.*, 102(1):63–74.

Klassen, N. V. & Ross, C. K. (2002). Water calorimetry: A correction to the heat defect calculations. *J. Res. Natl. Inst. Stand. Technol.*, 107(2):171–178.

Kohlrausch, F. (1996). *Praktische Physik, Band 3*, (24 ed.). Teubner.

Kraft, G. & Weber, U. (2011). Tumor therapy with ion beams. In: *Handbook of particle detection, imaging*, C Grupen, I Buvat, ed., volume 1, chapter 47, page 1179. Springer, Berlin.

Krämer, M., Jäkel, O., Haberer, T., Kraft, G., Schardt, D., & Weber, U. (2000). Treatment planning for heavy-ion radiotherapy : Physical beam model and dose optimization. *Phys. Med. Biol.*, 45:3299–3317.

Krauss, A. (2002). Experimental verification of caluclated radiation-induced heat conduction effects in the water absorbed dose calorimeter. *Thermochim. Acta*, 382:99–107.

Krauss, A. (2006a). Heat conduction effects during the calorimetric determination of absorbed dose to water in radiotherapy beams. *Thermochim. Acta*, 445:126–132.

Krauss, A. (2006b). The PTB water calorimeter for the absolute determination of absorbed dose to water in ^{60}Co radiation. *Metrologia*, 43:259–272.

Krauss, A., Büermann, L., Kramer, H.-M., & Selbach, H.-J. (2012). Calorimetric determination of the absorbed dose to water for medium-energy x-rays with generating voltages from 70 to 280 kV. *Phys. Med. Biol.*, 57:6245–6268.

Krauss, A. & Kapsch, R.-P. (2007). Calorimetric determination of k_Q factors for NE 2561 and NE 2571 ionization chambers in 5 cm x 5 cm and 10 cm x 10 cm radiotherapy beams of 8 MV and 16 MV photons. *Phys. Med. Biol.*, 52:6243–6259 and Corrigendum (2008), *Phys. Med. Biol.*, 53:1151–1152.

Krauss, A. & Roos, M. (1999). Heat transport by material-dependent heating during absorption of radiation in the water absorbed dose calorimeter. *Thermochim. Acta*, 337:45–49.

Landau, L. (1944). On the energy loss of fast particles by ionization. *J. Phys.*, 8:201–205.

Lemmon, E. W., McLinden, M. O., & Friend, D. G. (2005). Thermophysical properties of fluid systems, NIST Chemistry Webbook, NIST Standard Reference Database 69, available at http://webbook.nist.gov/chemistry/fluid/, accessed December 12, 2015.

Leo, W. R. (1994). *Techniques for Nuclear and Particle Physics Experiments: A How-To Approach*. Springer.

Looe, H. K., Harder, D., & Poppe, B. (2014). The volume-dependent correction factor kV - its derivation from the convolution model, some numerical examples and its relationship with the IAEA nonstandard field formalism. In: *Abstractbook of the Jt. Conf. SSRMP, DGMP, ÖGMP*, S. Klöck, ed., pages 13–16.

Lühr, A., Hansen, D. C., Jäkel, O., Sobolevsky, N., & Bassler, N. (2011). Analytical expressions for water-to-air stopping-power ratios relevant for accurate dosimetry in particle therapy. *Phys. Med. Biol.*, 56:2515–2533.

Lühr, A., Hansen, D. C., Teiwes, R., Sobolevsky, N., Jäkel, O., & Bassler, N. (2012). The impact of modeling nuclear fragmentation on delivered dose and radiobiology in ion therapy. *Phys. Med. Biol.*, 57:5169–5185.

Medin, J. (2010). Implementation of water calorimetry in a 180 MeV scanned pulsed proton beam including an experimental determination of k_Q for a Farmer chamber. *Phys. Med. Biol.*, 55(12):3287–98.

Muir, B. R. & Rogers, D. W. O. (2010). Monte Carlo calculations of k_Q, the beam quality conversion factor. *Med. Phys.*, 37(11):5939–5950.

Niatel, M. T., Perroche-Roux, A. M., & Boutillon, M. (1985). Two determinations of W for electrons in dry air. *Phys. Med. Biol.*, 30(1):67–75.

Niklas, M., Melzig, C., Abdollahi, A., Bartz, J. A., Akselrod, M. S., Debus, J., Jäkel, O., & Greilich, S. (2013). Spatial correlation between traversal and cellular response in ion radiotherapy - Towards single track spectroscopy. *Radiat. Meas.*, 56:285–289.

Osinga, J.-M. (2012). *Fluorescent nuclear track detectors: High-accuracy fluence determination in ion beams*. Master's thesis, Martin Luther University of Halle-Wittenberg.

Osinga, J.-M., Akselrod, M. S., Herrmann, R., Hable, V., Dollinger, G., Jäkel, O., & Greilich, S. (2013). High-accuracy fluence determination in ion beams using fluorescent nuclear track detectors. *Radiat. Meas.*, 56:294–298.

Osinga, J.-M., Ambrožová, I., Pachnerová Brabcová, K., Akselrod, M. S., Jäkel, O., Davídková, M., & Greilich, S. (2014a). Single track coincidence measurements of fluorescent and plastic nuclear track detectors in therapeutic carbon beams. *J. Instrum.*, 9:P04013.

Osinga, J.-M., Brons, S., Bartz, J. A., Akselrod, M. S., Jäkel, O., & Greilich, S. (2014b). Absorbed dose in ion beams: Comparison of ionisation- and fluence-based measurements. *Radiat. Prot. Dosimetry*, 161:387–392.

Palmans, H., Seuntjens, J., & Verhaegen, F. (1996). Water calorimetry and ionization chamber dosimetry in an 85-MeV clinical proton beam. *Med. Phys.*, 23(5):643.

Parodi, K., Mairani, A., Brons, S., Hasch, B. G., Sommerer, F., Naumann, J., Jäkel, O., Haberer, T., & Debus, J. (2012). Monte Carlo simulations to support start-up and treatment planning of scanned proton and carbon ion therapy at a synchrotron-based facility. *Phys. Med. Biol.*, 57(12):3759–3784.

PTCOG (2016). Webpage of the Particle Therapy Co-Operative Group (PTCOG), available at http://www.ptcog.ch/, accessed February 8, 2016.

PTW (2013a). *Gebrauchsanweisung Farmer-Kammer Ionisationskammer Typ 30010, 30011, 30012, 30013 (D596.151.00/04 de)*. Physikalisch-Technische Werkstätten GmbH, Freiburg, Germany.

PTW (2013b). *STARCHECK technical manual (D827.151.01/02 de)*. Physikalisch-Technische Werkstätten GmbH, Freiburg, Germany.

PTW (2015). *PEAKFINDER water column technical specifications (D847.219.00/03)*. Physikalisch-Technische Werkstätten GmbH, Freiburg, Germany.

R Development Core Team (2015). R: A Language and Environment for Statistical Computing (version 3.2.2), available at http://www.r-project.org, accessed November 22, 2015.

Rasband, W. S. *ImageJ (version 1.46a)*. U.S. National Insitutes of Health, Bethesda, Maryland, U.S.A., available at http://rsb.info.nih.gov/ij/, accessed November 22, 2015.

Ringbæk, T. P., Brons, S., Naumann, J., Ackermann, B., Horn, J., Latzel, H., Scheloske, S., Galonska, M., Bassler, N., Zink, K., & Weber, U. (2015). Fluence inhomogeneities due to a ripple filter induced Moiré effect. *Phys. Med. Biol.*, 60:N59–N69.

Rossomme, S., Palmans, H., Thomas, R., Lee, N., Duane, S., Bailey, M., Shipley, D., Bertrand, D., Romano, F., Cirrone, P., Cuttone, G., & Vynckier, S. (2014). Reference dosimetry for light-ion beams based on graphite calorimetry. *Radiat. Prot. Dosimetry*, 161(1-4):92–95.

Sakama, M., Kanai, T., Fukumura, A., & Abe, K. (2009). Evaluation of *w* values for carbon beams in air, using a graphite calorimeter. *Phys. Med. Biol.*, 54:1111–1130.

Salamon, M. H. (1980). A range energy program for relativistic heavy ions in the region $1 < E < 3000$ MeV/amu. *Lawrence Berkeley Natl. Lab. Rep. LBL-10446*.

Sarfehnia, A., Clasie, B., Chung, E., Lu, H. M., Flanz, J., Cascio, E., Engelsman, M., Paganetti, H., & Seuntjens, J. (2010). Direct absorbed dose to water determination based on water calorimetry in scanning proton beam delivery. *Med. Phys.*, 37(7):3541–3550.

Sassowsky, M. & Pedroni, E. (2005). On the feasibility of water calorimetry with scanned proton radiation. *Phys. Med. Biol.*, 50(22):5381–5400.

Sbalzarini, I. F. & Koumoutsakos, P. (2005). Feature point tracking and trajectory analysis for video imaging in cell biology. *J. Struct. Biol.*, 151:182–195.

Schardt, D. (2007). Tumor therapy with high-energy carbon ion beams. *Nucl. Phys. A*, 787(1-4 SPEC. ISS.):633–641.

Schardt, D., Elsässer, T., & Schulz-Ertner, D. (2010). Heavy-ion tumor therapy: Physical and radiobiological benefits. *Rev. Mod. Phys.*, 82(1):383–425.

Serber, R. (1947). Nuclear reactions at high energies. *Phys. Rev.*, 72:1114–1115.

Seuntjens, J. & Duane, S. (2009). Photon absorbed dose standards. *Metrologia*, 46(2):S39–S58.

Sigmund, P. (2004). *Stopping of heavy ions: A theoretical approach.* Springer.

Sternheimer, R. M., Berger, M. J., & Seltzer, S. M. (1984). Density effect for the ionization loss of charged particles in various substances. *At. Data Nulcear Data Tables*, 30:261–271.

Sykora, G. J., Akselrod, M. S., Benton, E. R., & Yasuda, N. (2008a). Spectroscopic properties of novel fluorescent nuclear track detectors for high and low LET charged particles. *Radiat. Meas.*, 43:422–426.

Sykora, G. J., Salasky, M., & Akselrod, M. S. (2008b). Properties of novel fluorescent nuclear track detectors for use in passive neutron dosimetry. *Radiat. Meas.*, 43:1017–1023.

Tessonnier, T., Marcelos, T., Mairani, A., Brons, S., & Parodi, K. (2016). Phase space generation for proton and carbon ion beams for external users' applications at the Heidelberg Ion Therapy Center. *Front. Oncol.*, 5:297.

Vavilov, P. V. (1957). Ionization losses of high-energy heavy particles. *Sov. Phys. JETP*, 5:749–751.

VIDAR. DosimetryPRO Advantage (Red): X-ray film digitizer for EBT film dosimetry, QA and IMRT, available at http://www.vidar.com/film/images/stories/PDFs/products/dosimetrypro/pdf/18155-001 Rev E DosimetryPROAdv.pdf, accessed October 10, 2015.

Wagner, W. & Pruß, A. (2002). The IAPWS formulation 1995 for the thermodynamic properties of ordinary water substance for general and scientific use. *J. Phys. Chem. Ref. Data*, 31(2):387–535.

Zavgorodnyaya, E. V. (2015). *Heat transport corrections for water calorimetry in scanned proton beams*. Master's thesis, Radboud University Nijmegen.

Ziegler, J. F. (1999). The stopping of energetic light ions in elemental matter. *J.Appl.Phys/Rev.Appl.Phys.*, 85:1249–1272.

Danksagung

Ich möchte mich ganz herzlich bei Prof. Dr. Oliver Jäkel für die Möglichkeit bedanken in seiner Abteilung *Medizinische Physik in der Strahlentherapie* am DKFZ promovieren zu dürfen und dabei, insbesondere auch in Kooperation mit der PTB, an spannenden Fragestellungen rund um die Dosimetrie von Kohlenstoffstrahlung arbeiten zu dürfen. Die Arbeit innerhalb der Kooperation hat mir viel Spaß gemacht und ich möchte mich an dieser Stelle sowohl bei Prof. Dr. Oliver Jäkel als auch bei Frau Dr. Ulrike Ankerhold, Leiterin des Fachbereichs *Dosimetrie für Strahlentherapie und Röntgendiagnostik* an der PTB, für die große Unterstützung und das Vertrauen bedanken. Insbesondere auch die Ermöglichung an mehreren internationalen Konferenzen teilnehmen zu dürfen weiß ich sehr zu schätzen. Des Weiteren möchte ich mich bei Prof. Dr. Wolfgang Schlegel für die Übernahme des Gutachtens bedanken.

Während meiner Doktorandenzeit durfte ich Teil zweier Arbeitsgruppen sein - zum einen der Arbeitsgruppe *Schwerionentherapie* geleitet von Dr. Steffen Greilich am DKFZ sowie der Arbeitsgruppe *Einheit der Wasser-Energiedosis* unter der Leitung von Dr. Achim Krauss an der PTB - bei deren Mitgliedern und Ehemaligen ich mich ganz herzlich für die schöne Arbeitsatmosphäre und die viele Unterstützung bedanken möchte. Insbesondere danke ich Dr. Steffen Greilich für die Betreuung dieser Arbeit von Seiten des DKFZ besonders rund ums Thema FNTD, Dr. Eduardo Yukihara für seine Hilfe bei den Monte Carlo Simulationen, Christian Möhler für seine Diskussionsfreude, die mir so manches Mal auf die Sprünge geholfen hat, Dr. Nora Hünemohr für nette Gespräche auch über die Arbeit hinaus und Dr. Bernadette Breithaupt für ihre großartige Unterstützung in jeglicher Hinsicht. Vielen Dank auch Gernot Echner, Armin Runz sowie den Mitarbeitern der mechanischen Werkstatt am DKFZ fürs Konstruieren und Bauen des tollen Kalorimeter-Phantoms, welches für diese Arbeit von unschätzbarem Wert war. Im Besonderen möchte ich mich ganz herzlich bei Dr. Achim Krauss für die tolle Betreuung im Rahmen des Wasserkalorimetrie-Projekts bedanken, für die vielen, vielen Diskussionen und das rauf und runter lesen dieser Arbeit. Ein großes Dankeschön gilt Karl-Heinz Misselhorn und Andreas Schlesner, von denen ich sehr viel im praktischen Umgang mit dem Kalorimeter und der Messtechnik gelernt habe und die mich bei den nächtlichen Messkampagnen am HIT tatkräftig unterstützt haben.

Ohne Kohlenstoffstrahlung hätte diese Arbeit ganz schön mau ausgesehen! Ich möchte mich daher ganz herzlich beim HIT-Team für die viele Strahlzeit und tolle Unterstützung bedanken. Ein ganz besonderes Dankeschön gilt dabei Dr. Stephan Brons, der immer mit Rat und Tat zur Seite stand und selbst mitten in der Nacht per Telefon so manche Strahlzeit gerettet hat. Des Weiteren danke ich Julian Horn, Dr. Harald Latzel und Benjamin Ackermann für ihre Hilfe rund ums Thema Feldverteilungsmessungen, Dr. Andrea Mairani und

Thomas Tennossier für die Unterstützung bei den Monte Carlo Simulationen sowie Thomas fürs Bereitstellen der *PS files*, Udo Bauer für die Hilfe beim Installieren des Wasserkalorimeters sowie dem Beschleuniger-Team für die Hilfsbereitschaft und Flexibilität während der nächtlichen Messungen.

Mein allergrößter Dank gilt aber meiner Familie, die mich immer wieder daran erinnert, was wirklich wichtig ist im Leben. Insbesondere meinen Eltern, die immer an mich glauben und bedingungslos hinter mir stehen, meinem kleinen Bennett Jasper, der so geduldig in meinem Bauch gewartet hat, bis diese Arbeit fertig geschrieben war und mich seitdem überglücklich macht und natürlich dir Alex, einfach für alles!